Title
Pinned boundary piezoelectric micromachined ultrasonic transducers (PMUT)

Author
Liang, Yue

Publication Date
2020

Pinned boundary piezoelectric micromachined ultrasonic transducers (PMUT)

By

Yue Liang

A dissertation submitted in partial satisfaction of the

requirements for the degree of

Doctor of Philosophy

in

Engineering – Mechanical Engineering

in the

Graduate Division

of the

University of California, Berkeley

Committee in charge:

Professor Liwei Lin, Chair
Professor Lisa Pruitt
Professor Ming C. Wu

Spring 2020

Pinned boundary piezoelectric micromachined ultrasonic transducers (PMUT)

by

Yue Liang

Abstract
Pinned boundary piezoelectric micromachined ultrasonic transducers (PMUT)

by

Yue Liang

Doctor of Philosophy in Mechanical Engineering

University of California, Berkeley

Professor Liwei Lin, Chair

Ultrasound technologies can be applied to a variety of applications, such as medical imaging/therapeutics, materials assessment, flow rate measurement and others. Piezoelectric micromachined ultrasonic transducers (PMUTs) have advantages over the traditional bulk transducers in wide bandwidth, small size, and low cost. This work proposes to boost PMUT's acoustic performance further including vibrational amplitude, acoustic pressure and electromechanical coupling by using the pinning boundary structure and to explore various new applications.

The equivalent circuit model for pinned boundary PMUTs has been developed and validated with simulation results in terms of mode shape and displacement of the piezoelectric diaphragm under the alternative electrical voltage inputs. Prototype devices with pinned boundary are then fabricated without adding any fabrication complexity as compared to the conventional fabrication process of PMUTs by modifying the mask designs. Fabrication limitation of PMUTs with low resonant frequency is also investigated by fabricating prototype chips that operate at a resonant frequency of 338 kHz in air to experimentally detect objects at 22 cm away. Furthermore, testing results show a measured 2.5 times improvement in center displacement and 3.3 times improvement in the pressure output as compared with those PMUTs based on the traditional design with clamped boundary. The measured mode shape deformation results match well with the analytical and simulation results and a dual-electrode pinned PMUT structure is proposed to enable a single chip for both transmitting and receiving functionality without sacrificing the improved acoustic performance.

In the area of practical applications, a tilt angle sensing chip based on the PMUT device has been demonstrated based on the amplitude of signals from the receiver PMUT. It is found that the measured sensing results match well with

theoretical predictions with an average error of ±0.7 degree within the tilting range of plate between -8 to 8 degrees. A wireless power transfer system is then proposed based on a pinned ring PMUT transmitting array to provide a maximum efficiency of 57% at a focus point 2.7 mm away at a resonant frequency of 250 kHz.

To my Mother and Father

TABLE OF CONTENTS

LIST OF FIGURES

LIST OF TABLES

Chapter 1
Introduction

1.1 Introduction to Piezoelectric Micromachined Ultrasonic Transducer

Ultrasound transducers have a long history in the technological world. The first application using ultrasound was an attempt to detect submarines in 1917 [1-3]. In the modern world, people use ultrasound in Sonar to navigate, communicate and detect objects [4]. People also use Sonar to map the seafloor. In medical field, people use ultrasound for real time medical imaging such as b-scan. People also use high intensity focused ultrasound for therapeutics [5-13]. In materials and construction, people use ultrasound for non-destructive examination to evaluate internal cracks of material [14].
Many of these applications are based on the pulse-echo method. As illustrated in figure 1.1.1, when we excite the ultrasonic transducer electrically, it sends out an ultrasonic wave which will be reflected partially whenever there is a change in medium. As demonstrated in the figure, the induced ultrasound is being reflected by a defect and the back wall of the specimen. These reflected signals are called echoes and are collected by the ultrasonic transducer.

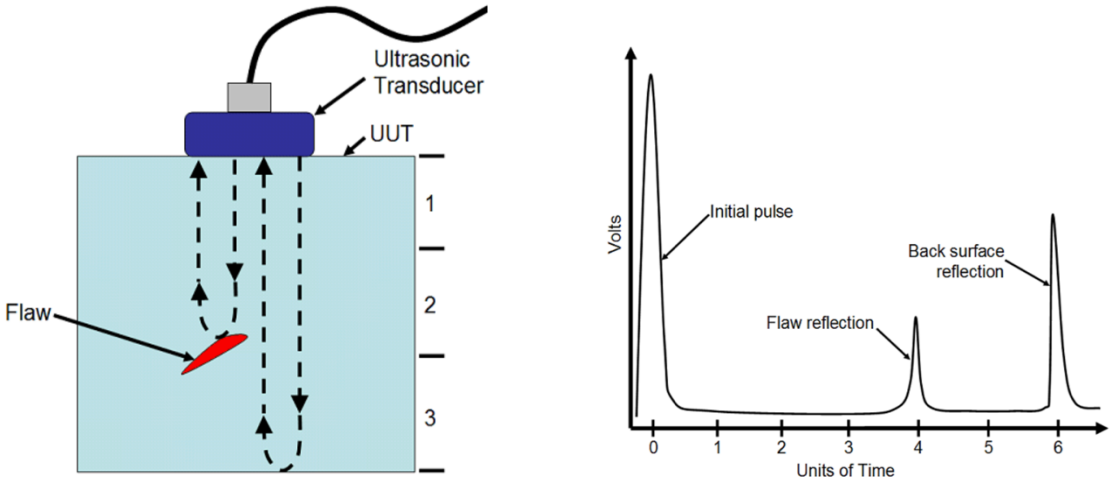

Source: National Instruments

Figure 1.1.1. Demonstration of pulse-echo experiment [15].

For a bulk ultrasonic transducer, it utilizes piezoelectric material to realize a transfer of energy from electrical energy to mechanical energy and vice versa. When we induce an electric field across a piezoelectric material, it causes an internal change in strain [1-3]. The material will then expand or shrink. And if we apply an AC signal at a certain frequency, the material will continuously vibrate. The vibration will then launch an ultrasonic wave into the medium. Typical piezoelectric materials that people use today are Lead zirconate titanate (PZT), Zinc oxide (ZnO), and Aluminum nitride (AlN).

In the early 1990s, with the advance of micromachining technology in the emerging Microelectromechanical system (MEMS) field, researchers started to explore possibilities of using Micromachined ultrasonic transducer (MUT) as an alternative to a traditional bulk ultrasonic transducer.

There are several advantages of MUT. Their miniature size costs much less power compared to bulk ultrasonic transducers [16-27]. Due to the batch fabrication, MUTs are lower in cost [16-27]. The fact that many MUTs are CMOS compatible makes them suitable for consumer electronics and portable devices [16-27]. MUTs are low in mass due to its small size and their compliant membrane structure makes them match much better to fluid loads compared to bulk ultrasonic transducer which results in a much wider bandwidth [16-27]. The wider bandwidth provides MUTs with higher resolution and more efficient energy conversion. In addition, MUTs can be tailored to various sizes and arranged into array elements. This provides MUTs with a wide operating frequency range and beam steering ability which opens up more application space. For example, people use MUTs for portable medical imaging [28-30]. Several companies have been using MUTs for fingerprint recognition [31-34]. In addition, people use MUTs for gesture recognition and range finding [35-40]. People also use MUTs as flow sensor for manufacturing process and environmental monitoring [41-43].

There are two types of MUTs: Capacitive MUT (CMUT) and Piezoelectric MUT (MUT). In a CMUT, the induced electrostatic force from the applied voltage causes a change in capacitance which leads to the vibration of the plate as shown in figure 1.1.2 (a).

In a PMUT, the induced electric field causes a change in strain, which in turn induces a bending moment that leads to the vibration of the plate. The vibrating plate then launches an ultrasonic wave into the surrounding medium [18-22].

One quantity people generally use to compare the performance across different transducer is the electromechanical coupling coefficient, which quantifies the amount of input electrical energy that's been converted to mechanical energy [1-3]. In CMUT, the coupling coefficient is dependent on design parameters like

gap space and DC bias [23-27]. Where in PMUT, the coupling coefficient is limited by material constant [18-22].

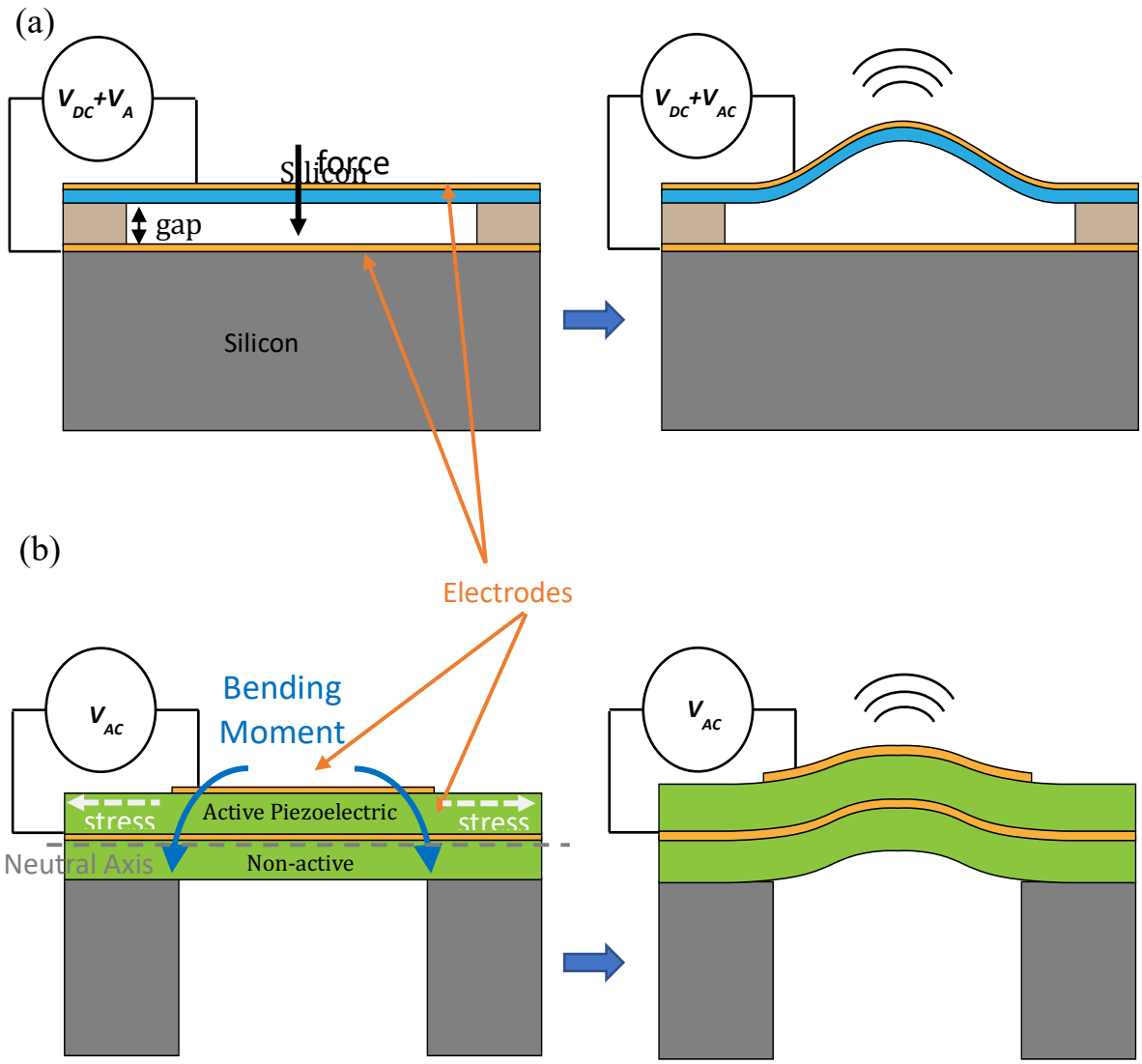

Figure 1.1.2. Schematics of working mechanism of MUTs (a) Working mechanism of CMUT. (b) Working mechanism of PMUT.

CMUT is a relatively matured technology. It has high coupling coefficient when superimposed with large DC bias and designed with small gap spacing [23-27]. However, the required bias voltage for good coupling is typically more than 100 volts which makes them less attractive for portable device [23-27]. In addition, its maximum displacement is limited by the gap spacing [23-27]. As a result,

CMUTs are less efficient as a transmitter which requires large displacements to transmit sufficient power.

PMUTs became an attractive alternative in recent years due to the advance of thin piezoelectric film deposition technology. On top of that, PMUT does not require a bias voltage. It also does not have the thin gap geometry restriction which makes PMUT a good candidate as a transmitting unit. However, current PMUT designs have relatively low electromechanical coupling compared to the maximum achievable value calculated from material constants [18-22].

Because of the aforementioned reasons, we investigated possibilities to improve PMUT's electromechanical coupling and make use of such PMUTs in different applications.

In chapter 2, we worked on designing a new PMUT structure which we call a pinned PMUT to improve its electromechanical coupling. In a traditional PMUT, the plate is clamped at the boundary. Due to clamping, the vibrating amplitude is limited. As a result, the transferred kinetic energy is also limited which leads to low electromechanical coupling.

Researchers have done theoretical work that shows improvement in displacement amplitude of PMUTs when boundary condition is changed from clamped to pinned [44-46]. However, putting such boundary condition into a real device have not been investigated yet. We designed the pinned PMUT structure which allows the plate with more vibrating amplitude to provide more transferred kinetic energy and more efficient coupling.

The pinned boundary condition also changes the PMUT's vibrating mode shape which leads to larger effective vibrating area. As a result, we can cover more area with electrodes and make use of more piezoelectric material.

The combination of improved vibrating amplitude increased effective vibrating area and increased electrode coverage further boosts electromechanical coupling of a pinned PMUT structure.

This pinned PMUT design is validated using simulation with boundary condition carefully designed to match real life scenario. We then fabricated such device in the Berkeley Marvell Nanofabrication Lab. We later on characterized such device using a digital holographic microscope. The experimental result shows matching mode shape and frequency response compared to simulation result. Figure 1.1.3 (a) shows the 3D schematics of a pinned PMUT structure [47].

In chapter 3, we improved on the existing design of the pinned PMUT to enable same chip transmitting (TX) and receiving (RX) functionality. There are different ways to achieve same chip TX and RX functionality. Standalone PMUTs can be arranged in the same array with two sets of wirings to selectively activate certain PMUTs within the array and use the rest of the PMUTs for

receiving purpose. However, this arrangement has drawbacks such as complicated wiring scheme for a single PMUT to be wired out without interfering the neighboring PMUTs. We seek a way to use a standalone PMUT for TX and RX as an alternative.

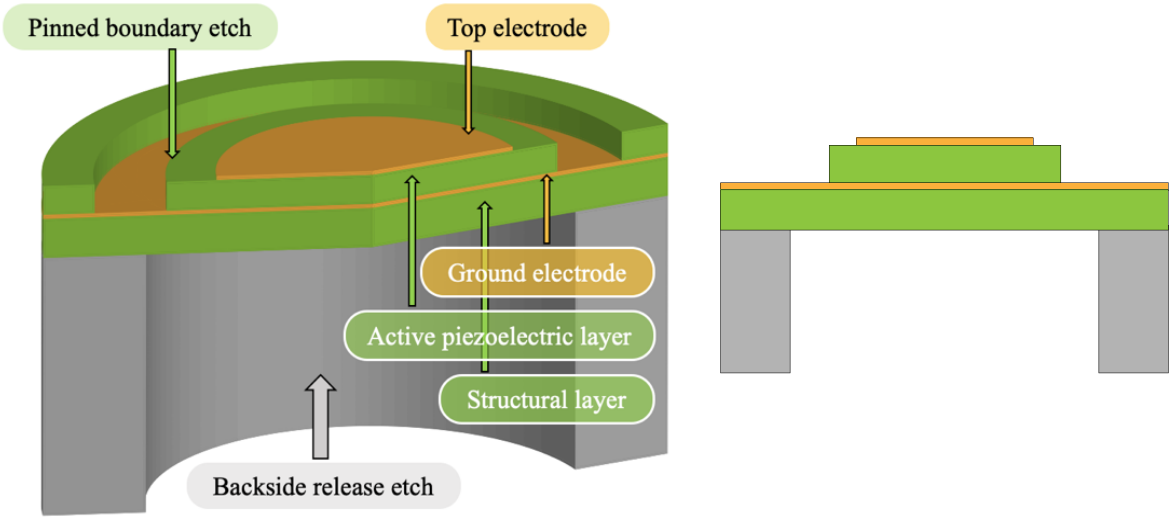

Figure 1.1.3. Schematics of pinned PMUT.

As a result, we designed the dual-electrode pinned PMUT to enable same chip TX and RX functionality. The difference between the original pinned PMUT and the dual-electrode pinned PMUT is essentially the location of etching that realizes the pinned boundary condition. In the original pinned PMUT design, the etching profile happens at 80% of diaphragm radius. For a dual-electrode pinned PMUT, the etching profile happens at around 60% of diaphragm radius where inner electrode occupies 57% of radius and outer electrode occupies 43% of radius. This is proven to be the best design to ensure good performance of the chip. Here, good performance means same acoustic response when inner and outer electrode are excited differentially compared to the original pinned PMUT design while providing the same acoustic response when inner and outer electrode are excited separately.

From simulation results, we compared mode shape of a traditional clamped PMUT, the original pinned PMUT and the dual-electrode PMUT and we found that the mode shape of the dual-electrode PMUT follows that of a traditional

clamped PMUT. The 3D schematics of a dual-electrode pinned PMUT is shown in figure 1.1.4.

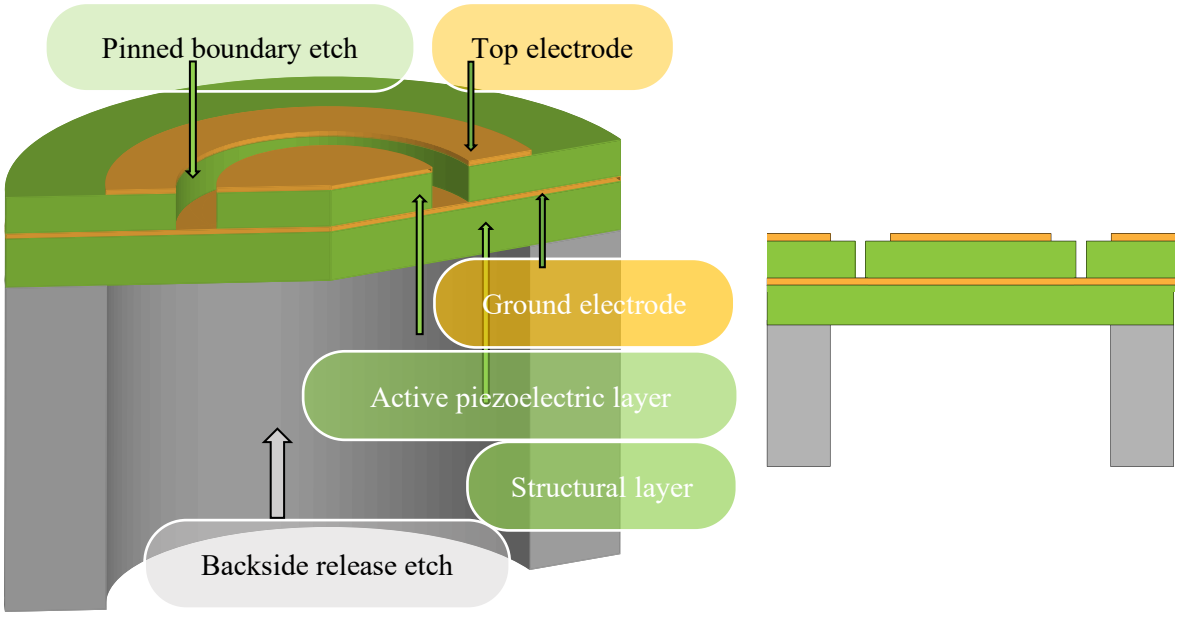

Figure 1.1.4. Schematics of dual-electrode pinned PMUT.

We then explored possibilities of using such PMUT chips in applications. Chapter 4 described a tilt sensor application using such pinned PMUT design. People has explored quite a lot using CMUT as an ultrasonic tilt sensor [48] which can be used in applications such as mobile device angle detections. However, previous work mostly focuses on determining tilt angle from time-of-flight in the pulse-echo mode which may suffer from inaccuracies due to difficulty in determining the onset of echo. We hereby propose a novel method of using the received signal strength in pulse-echo mode to determine the tilt angle. The setup of such tilt sensing system is shown in figure 1.1.5. We place our tilt sensing chip on one side and the reflector which changes tilt angle 4 cm to 5 cm away from the sensing chip. One array from the chip sends out an ultrasonic wave which will be reflected back when the wave hit the reflector. The reflected signal will change in strength based on the tilt angle. We can then determine the tilt angle based on this change in ultrasound strength/receiving PMUT voltage.

Chapter 5 explored possibilities of using PMUT for wireless power transfer with pinned PMUT structure. Wireless power transfer is a trending research field as it be used in either consumer electronics for wireless charging or medical area to charge medical implants [49-52]. Going wireless is the ultimate goal for most modern devices as it provides more convenience for users. For wireless charging, people mainly use near-field wireless power transfer.

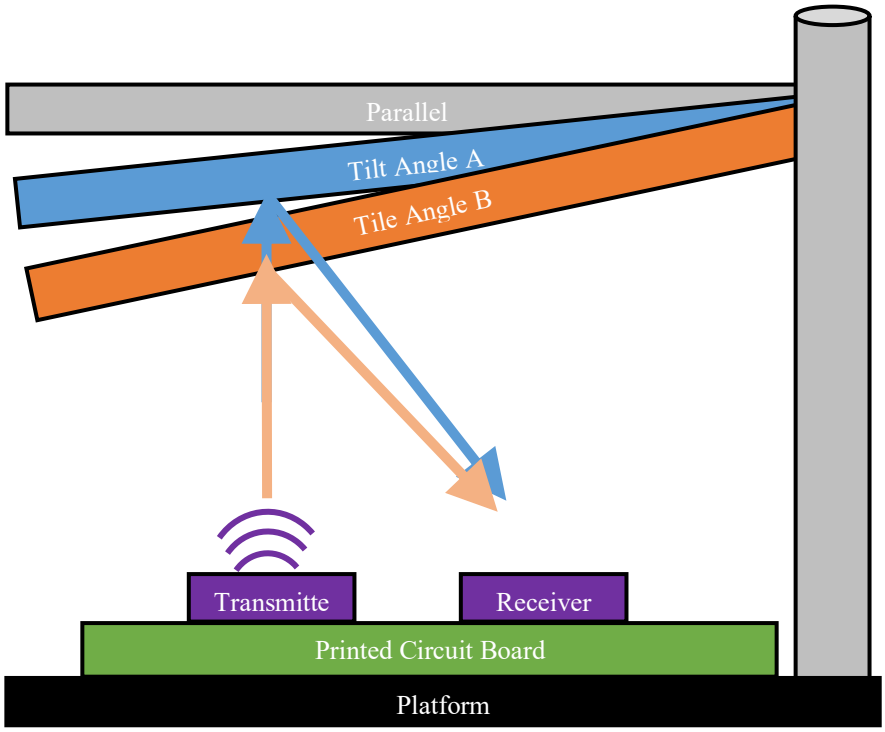

Figure 1.1.5. Schematics of tilt sensing setup.

The current dominating technology is inductive charging using magnetic fields. This method provides good efficiency [49]. However, it has limitations where inductive charging cannot charge parts that has metal as the existence of metal part will block the magnetic field pathway [49-52].
In general, previous studies either focus on using inductive charging, or using a bulk ultrasound transducer as the transmitting unit [49-52]. No one has yet explored the possibility of building a wireless power transfer system that consist solely MEMS-acoustics device.

Since MEMS device typically are small in size, we expect these devices to consume much less power. In addition, with the pinned PMUT design, we expect to see a major improvement in transmitting power. As a result, we explored the possibility of building a wireless power transfer system using the pinned PMUT structure.

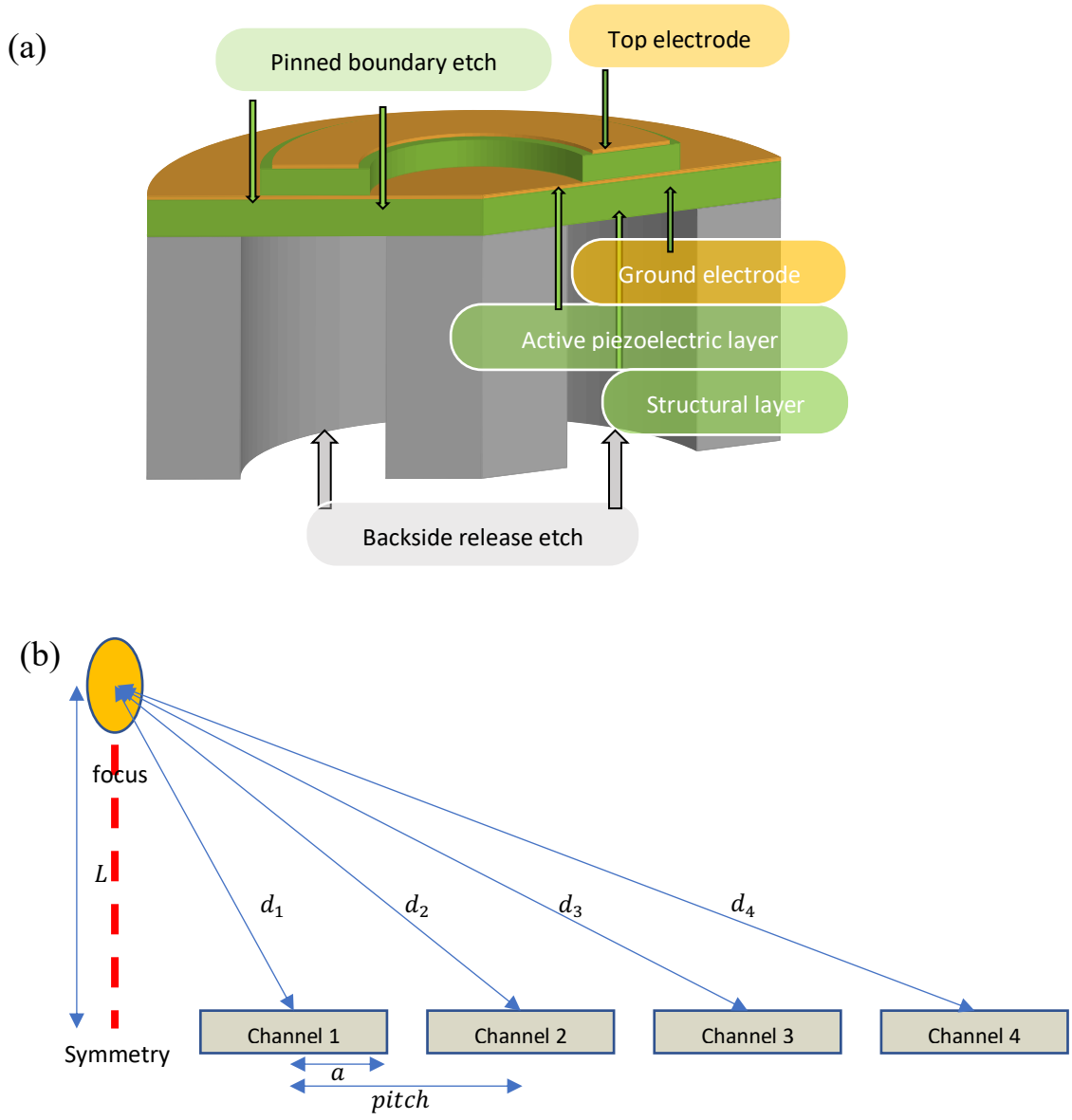

Figure 1.1.6 Schematics of pinned ring PMUT and wireless power transfer setup.

We first designed a pinned ring PMUT with improved vibrating amplitude. We then arranged such pinned ring PMUT into annular arrays to form the transmitting unit. These arrays were grouped into four channels which will be activated with a phase delay to further focus the emitted ultrasound. To allow more emitted power, we designed these PMUTs with large diaphragm size which lowers the resonant frequency of the device.

The schematics of a pinned ring PMUT is shown in figure 1.1.6 (a) and the schematics of the setup of the WPT system is shown in figure 1.1.6 (b).

As we explored the wireless power transfer system using PMUT, one essential design parameter is the diaphragm size which is limited by the fabrication process. With increasing diaphragm size, the standalone PMUTs tends to break due to stress distribution.

As a result, chapter 6 explores the fabrication limitation of fabricating PMUTs with large membrane size. We arranged these standalone PMUT into arrays where each array consists 4x20 standalone PMUT. We then explored long-distance object detection using these manufactured chips.

Traditionally, we have designed and fabricated PMUTs with as low a frequency as 630 kHz in air. However, this is still too high for most air-coupled applications since ultrasound attenuates logarithmically with increased frequency. We therefore designed and manufactured two PMUT chips with much larger diaphragm size and characterized them in pulse-echo mode.

The larger radius PMUT has a r = 355 um which gives 180 kHz resonant peak where the smaller radius PMUT has a r = 275 um which gives 338 kHz resonance peak. We then utilize the chip for long-distance object detection where we placed a paper cup upside down with a distance of 12 cm from rim of cup to PMUT chip and a distance of 22 cm from bottom of cup to PMUT chip. The experimental setup is shown in figure 1.1.7.

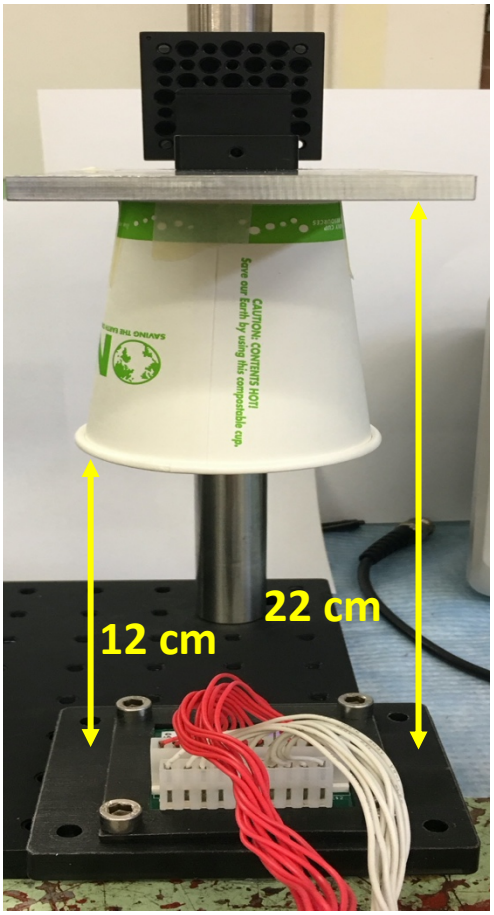

Figure 1.1.7 Experimental setup of long-distance object detection.

Chapter 2

Pinned PMUT

2.1 Introduction

As previously discussed, comparing to CMUTs, PMUTs require minimum to zero DC bias voltage, can be driven linearly, and have no displacement restrictions. However, the functionality of PMUTs are still significantly limited due to its limited electro-mechanical coupling and bandwidth [1-3, 18-22].
Electro-mechanical coupling coefficient k^2 is the ratio of converted mechanical energy to input electrical energy as described in the relationship below [1-3].

$$k^2 = \frac{converted\ mechanical\ energy}{input\ electrical\ energy} \tag{2.1.1}$$

The higher the coupling coefficient, the more mechanical energy is being converted. This means that the device will have a larger displacement which leads to a higher pressure output.
Bandwidth of a device in air is related to the Q factor. For a device to have larger bandwidth, we want to have lower Q factor which means we want a device that can lose or transfer a lot of energy to the medium [1-3]. Having a wider bandwidth can also provide better axial resolution and is beneficial for broadband applications such as harmonic imaging [53].
Researchers have done some previous works on improving PMUTs' functionality for either airborne or immersion applications [53-59]. For airborne applications, researchers have worked on improving PMUTs' pressure output through design modifications to allow more vibrational displacement which in turn improves PMUTs' electro-mechanical coupling and thus higher pressure output [60-62].
For immersion applications, researchers have worked on inducing a second resonance due to interactions between the medium and the device during vibration. By careful tuning, this induced resonance can be close to the resonant frequency of the device itself which then lead to a wider bandwidth [63].
Although researchers have worked on improving airborne PMUTs' pressure output, the results are not as promising. In particular, not much work has focused on changing the boundary condition of PMUT. In fact, by changing PMUT's boundary condition, we can have different vibration mode shapes. Sammoura et al. have presented through analytical modeling that a four times improvement

in center displacement at resonance can be achieved if the boundary condition of the device is changed from clamped to pinned [46].
In this chapter, we describe the design concept, analytical modeling, simulation results, fabrication process and experimental results of a pinned PMUT structure. The improvement of such a device is mainly through the change of its boundary conditions which leads to not only larger displacement amplitudes at resonance, but also increased effective vibrating area due to the change of mode shape. The effective vibrating area quantifies how much of the total surface area of a PMUT is sending out ultrasonic wave. This in turn leads to increased electrode coverage and thus further improves the device's pressure outputs [18-22].

2.2 Device Concept

Although theoretical work has been done to improve the displacement amplitude of PMUTs when boundary condition is being changed from clamped to pinned, no experimental work has been investigated [46,58,62].
Note that a PMUT typically requires a structural layer or in our case a non-active piezoelectric layer so that when the structure is under deflection, the neutral axis is not within the active piezoelectric layer. As we discussed before, in a PMUT, the induced electric field causes a change in strain based on the piezoelectric effect. This change in strain causes mechanical deformation which induces a bending moment. This bending moment in turn causes the PMUT to deflect which then launches an ultrasonic wave [1-3,18-22].
When the wave is being launched, the PMUT is in transmitting mode and we call it a transmitter. If on the other hand, an incoming ultrasonic wave hits the transducer, then the generated pressure will cause a change in the strain which induces a change in electric field and the PMUT is in receiving mode. In which case we call it a receiver [18-22]. Furthermore, if we arrange PMUTs into an array, then we can send a larger ultrasonic wave and it is indeed the PMUT arrays that enable many applications like the tilt sensor that we will cover in later chapters.
Now if we take a closer look at a single PMUT, we notice that a typical PMUT design clamps the plate at the boundary. As a result of clamping, the plate provides less amplitude. Since amplitude translates directly into kinetic energy, it follows that the clamp plate offers less efficient coupling [1-3].
We know that the piezoelectric effect is the relationship between electric field and strain and strain is the second derivative of curvature of the plate. In a clamped plate under deflection, the curvature in the center and the border are of opposite signs and the sign changes at 70% of the radius [18-22].

Thus, for efficient piezoelectric coupling, electrodes should only cover areas with the same sign of curvature or otherwise one part of the structure will be working against the other. As a result, we're wasting part of the piezoelectric material due to clamping which leads to limited coupling and electrode coverage.

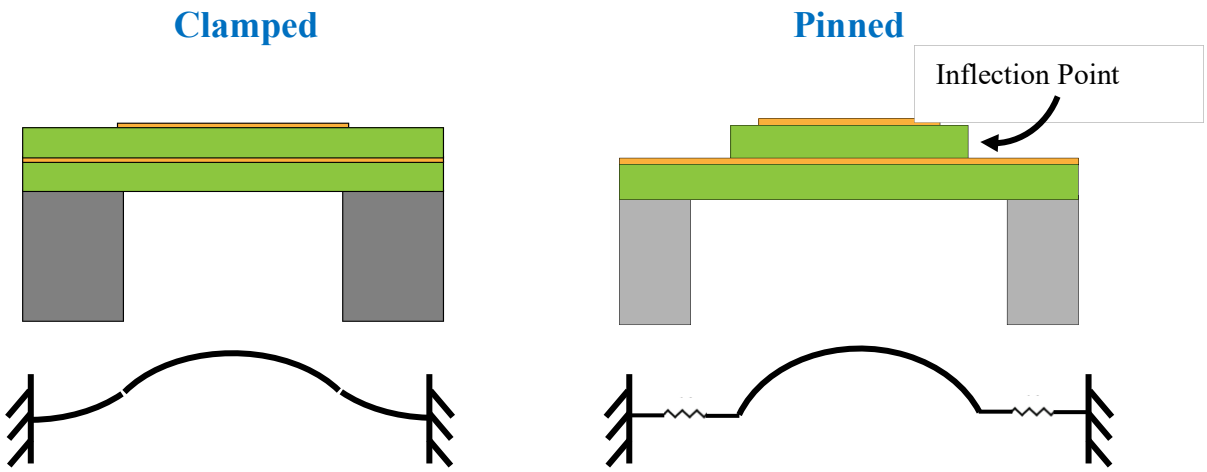

Figure 2.2.1. Demonstration of difference between a clamped plate and a pinned plate.

If we remove a small region of the piezoelectric layer at the edge, then we are effectively replacing that area with a softer spring as demonstrated in figure 2.2.1. In this way, we can tune the ratio of radius of the active and inactive layers until the entire top film is ideally pinned and the inflection point takes place at where the material is being removed.

Figure 2.2.2 explains the design concept in detail with both top view and cross-sectional view. The overall structure contains a piezoelectric layer on a structural layer, both colored in green. To realize the pinned boundary, we etch away the edge of the top active piezoelectric layer as shown in figure 2.2.2 labeled in green. The top and bottom electrodes are colored in orange. The backside DRIE that frees the membrane is colored in grey.

Although we would like to directly compare the electromechanical coupling coefficient k^2 of a clamped and pinned plate, we are comparing center displacement w_{peak} and pressure output p instead mainly because the measured

coupling coefficient typically contains parasitic effects and do not reflect the true coupling coefficient.
Comparing center displacement and pressure output is representative since center displacement translates directly to mechanical energy [1-3]. The pressure output of a PMUT is proportional to the volumetric displacement V_{V}, which is the product of the center displacement w_{peak} and the effective vibrating area $A_{effective}$ as described in the following equation where $\phi(r)$ is the mode shape of the device [1-3].

$$p \propto V_{\mathrm{V}} = \int w dA = w_{peak} \int \phi(r) dA \, 2\pi w_{peak} \int_0^a \phi(r) r dr = A_{effective} w_{peak} \tag{2.2.1}$$

The complete three-dimensional schematic view of the structure of a pinned boundary PMUT is shown in figure 2.2.3. As mentioned before, the pinned boundary is realized through etching away part of the top active piezoelectric layer. The ground electrode plane serves as a etch stop and the top electrode is covered to 80% of the radius of the device. This number is based on both analytical model and simulation results which will be covered in detail in later sections of this chapter. The 80% coverage ensures optimal performance of the device. The radius of the device is defined by the backside opening from DRIE. Both the top and bottom layers are made of piezoelectric material shown in green. However, only the top layer is active by applying a voltage difference through the electrodes shown in orange [47].
As we apply a voltage difference between the top and bottom electrodes, the device vibrates into a quasi-pinned mode shape where mode shape within the diaphragm of pinned boundary etch is that of a free plate and the mode shape outside of the pinned boundary etch is that of a clamped plate. The optimal electrode coverage is thus modified accordingly as the active piezoelectric area is increased from 70% of a clamped plate to 80% of the quasi-pinned plate. As a combined result, we can get a larger displacement amplitude at resonance along with a larger effective vibrating area which gives us the higher pressure output [47].

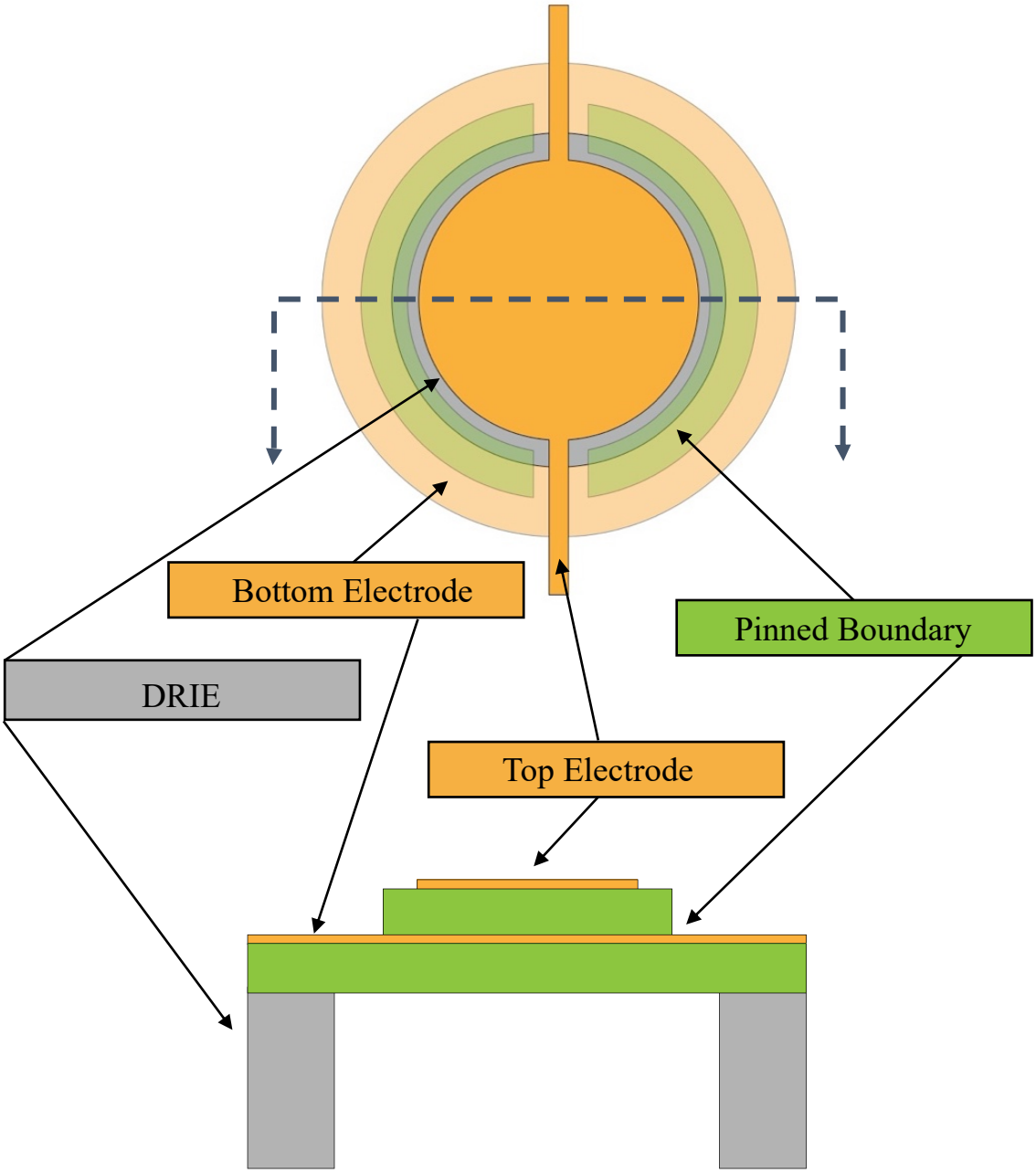

Figure 2.2.2. Device structure in detail with both top view (top part of the figure) and cross-sectional view (bottom part of the figure) labeled in color where piezoelectric layer in shown in green, electrodes are shown in orange and membrane is shown in grey.

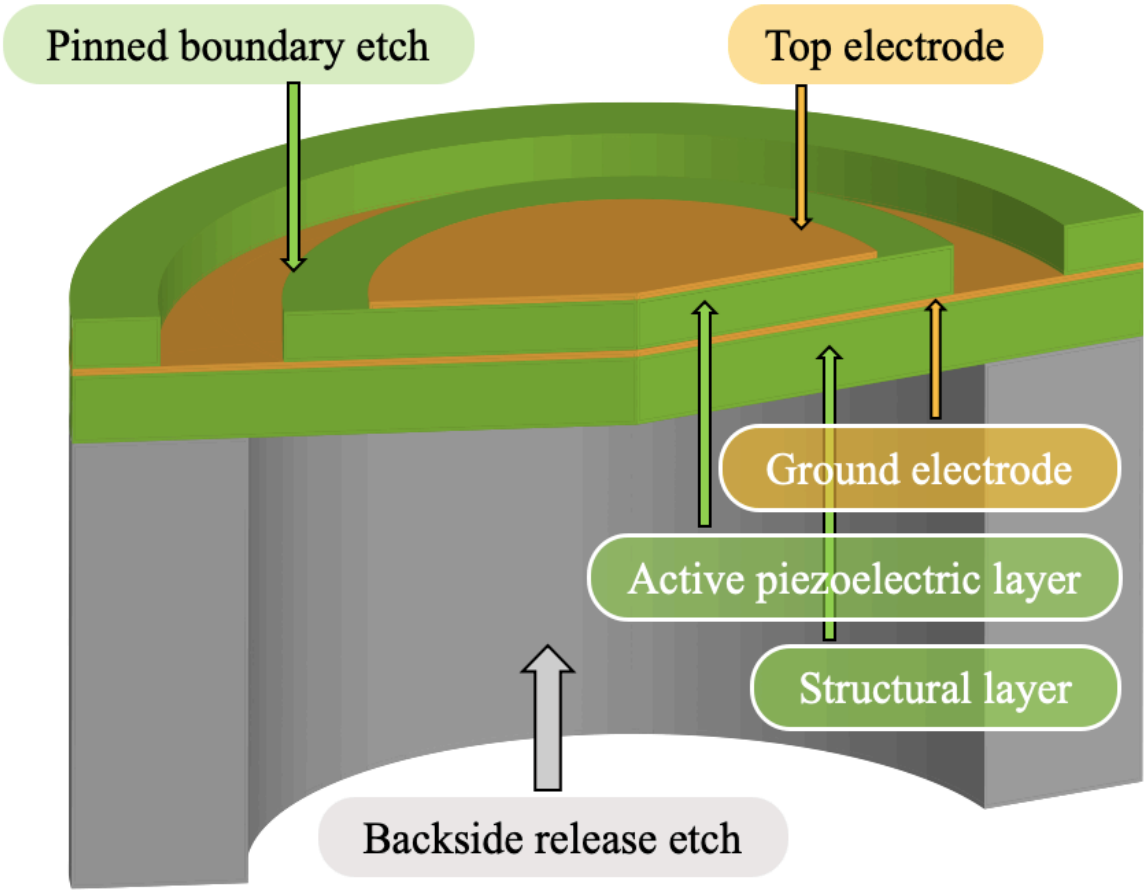

Figure 2.2.3. 3D schematic view of a pinned boundary PMUT with an active piezoelectric layer on a structural layer and the backside release etch to free the membrane. The top electrode covers 80% of radius for optimal performance where radius is defined by the backside release etch.

2.3 Equivalent Circuit Model

A moving mechanical structure can be represented by electrical elements as shown in the following schematics. In figure 2.3.1, R represents mechanical resistance, M represents mechanical mass which is related to inductance, and k represents mechanical stiffness which is related to capacitance [1-3].

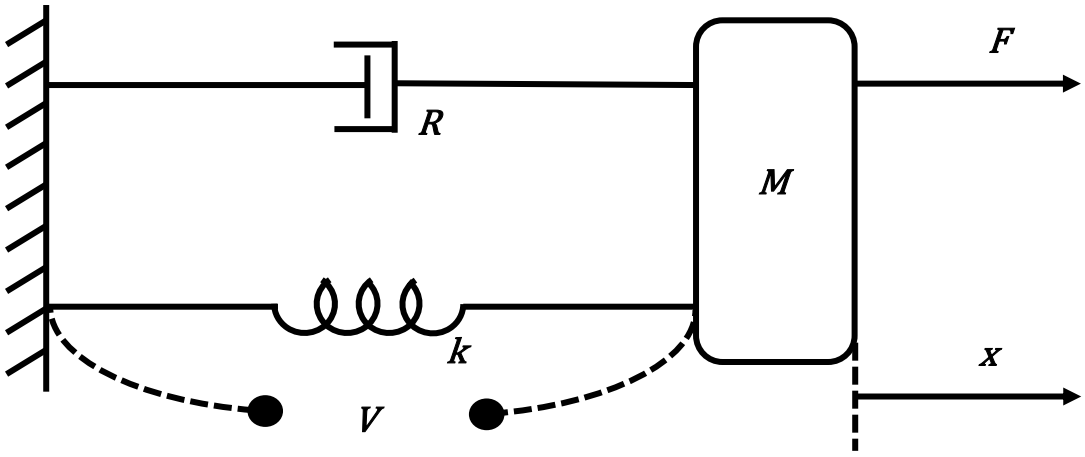

Figure 2.3.1. Electrical model of a moving mechanical component.

Building upon a moving mechanical component, a transducer is a two-port network that can be represented by the equivalent circuit model as shown in figure 2.3.2.

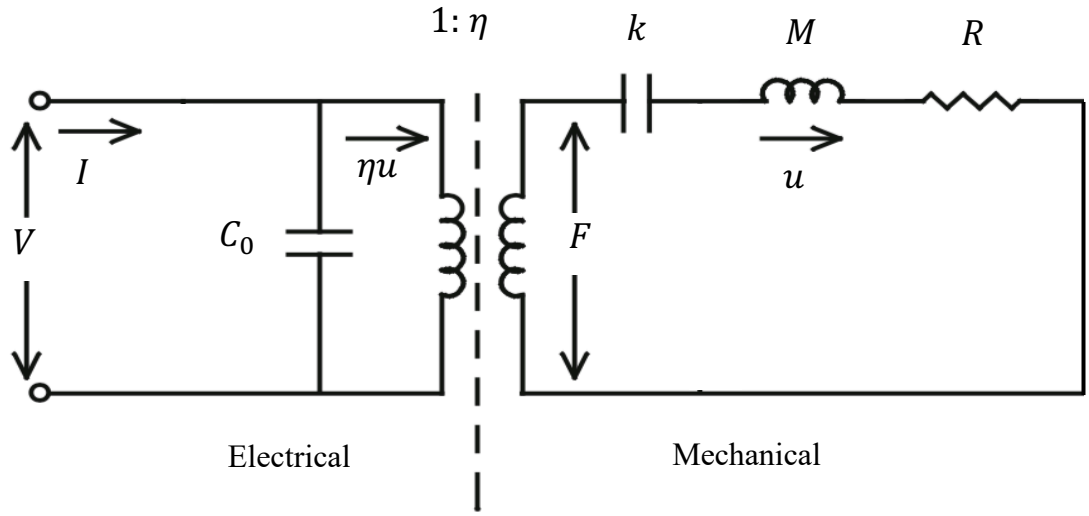

Figure 2.3.2. Equivalent circuit model setup containing both electrical and mechanical components.

In figure 2.3.2, the left portion of the circuit represents the electrical domain and the right portion represents the mechanical domain. The transformer represents the electromechanical transduction which in our case is caused by the piezoelectric effect. With equivalent circuit modeling, all design parameters can be represented by simple circuitry elements such that each term can be related to each other through equations as follows [1-3,64-73].

$$j\omega Mu + Ru + \frac{ku}{j\omega} = \eta V \tag{2.3.1}$$

$$I = j\omega C_0 V + \eta u \tag{2.3.2}$$

Where ω is frequency, u is velocity, η is transduction ratio, I is current and C_0 is capacitance.

With parameters being represented through electrical elements, we can then derive the system's frequency response. We first get the assumed mode shape by curve fitting in MATLAB R2019b (The MathWorks Inc., Natick, MA, USA) based on the simulated mode shape. The mode shape of the device takes the form as shown.

$$\varphi(r) = 1 - 1.76\left(\frac{r}{a}\right)^2 + 0.75(\frac{r}{a})^4 \tag{2.3.3}$$

A displaced PMUT is shown in figure 2.3.3 where w(r) is the displacement profile and is the product of center displacement and the system's mode shape as described in equation 2.3.4.

We can then derive stiffness k, mass m, and transduction ratio η from the assumed mode shape through energy terms. And by the end, we can get resonant frequency f [1-3,64-73].

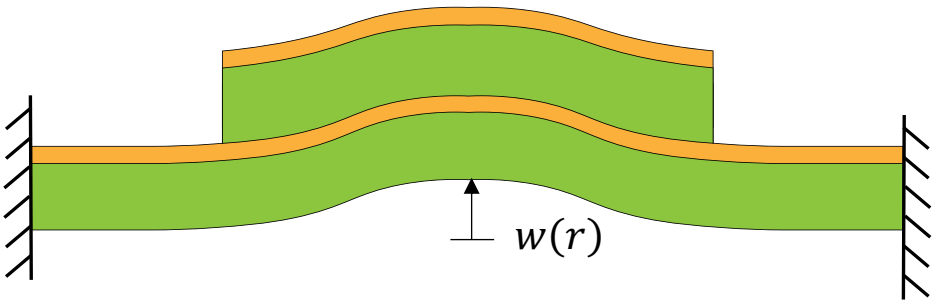

Figure 2.3.3. Schematics of a displaced PMUT.

and the dc displacement w_{dc} of the plate. Where displacement is described as below [1-3,64-73].

$$w(r) = w_0\varphi(r) \tag{2.3.4}$$

And velocity is described as below [1-3,64-73].

$$u(r) = u_0\varphi(r) \tag{2.3.5}$$

Resonant frequency is described as below [1-3].

$$f = \frac{1}{2\pi}\sqrt{\frac{k}{m}} \tag{2.3.6}$$

And dc displacement can then be derived based on transduction ratio η, input voltage V, and stiffness k as shown below [1-3].

$$w_{dc} = \frac{\eta V}{k} \tag{2.3.7}$$

The design parameters are shown in figure 2.3.4. We derive each circuitry element based on energy terms, where we get stiffness from elastic energy and mass from kinetic energy [1-3,64-73].
In figure 2.3.4, the neutral axis h_p is defined in equation 2.3.8 and distance to the neutral axis z_p is defined in equation 2.3.9

$$h_p = \frac{ah_0 + l(h_1 - h_0)}{2a} \tag{2.3.8}$$

$$z_p = h_0 + \frac{(h_1 - h_0)}{2} - h_p \tag{2.3.9}$$

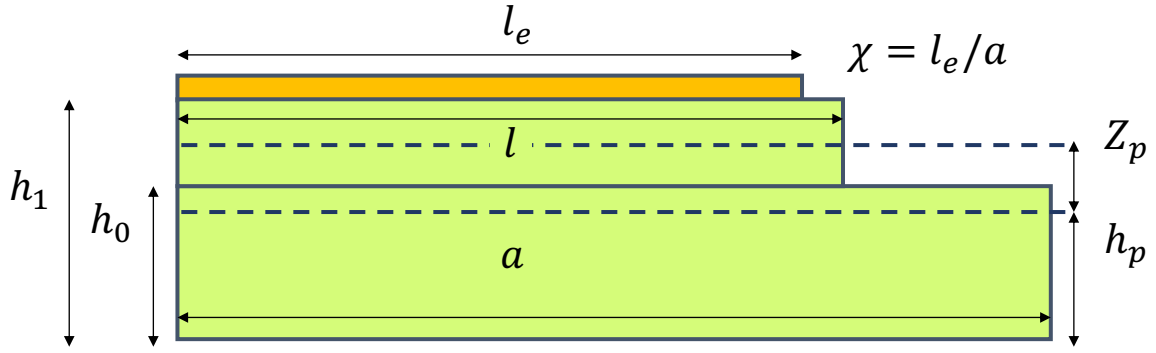

Figure 2.3.4. Schematics representation with parameters labeled.

We first use strain energy U_{Strain} to find stiffness. Strain energy is defined in equation 2.3.10 [1-3,64-73]. We can then find stiffness which is defined in equation 2.3.11 [1-3,64-73].

$$U_{Strain} = \frac{1}{2} k {w_0}^2$$

$$= 2\pi {w_0}^2 \int_{bot}^{top} {Y_0}'' z^2 dz \int_0^a \left[\left(\frac{\partial^2 \varphi}{\partial r^2}\right)^2 + \frac{2\upsilon}{r} \frac{\partial^2 \varphi}{\partial r^2} \frac{\partial \varphi}{\partial r} + \left(\frac{1}{r} \frac{\partial \varphi}{\partial r}\right)^2 \right] r dr \quad (2.3.10)$$

$$k = 4\pi \int_{bot}^{top} {Y_0}'' z^2 dz \int_0^a \left[\left(\frac{\partial^2 \varphi}{\partial r^2}\right)^2 + \frac{2\upsilon}{r} \frac{\partial^2 \varphi}{\partial r^2} \frac{\partial \varphi}{\partial r} + \left(\frac{1}{r} \frac{\partial \varphi}{\partial r}\right)^2 \right] r dr \quad (2.3.11)$$

Next, we use kinetic energy T to find equivalent mass. The equation for kinetic energy is defined in equation 2.3.12 and its equivalent mass is derived in equation 2.3.13 [1-3,64-73].

$$T = \frac{1}{2} m {u_0}^2 = \int_V \frac{1}{2} \rho \, u^2 = \frac{1}{2} \rho_s {u_0}^2 \int_{A_v} \varphi^2(r) dA_v \quad (2.3.12)$$

$$m = 2\pi \rho_s \int_0^a \varphi^2(r) r dr \quad (2.3.13)$$

Based on equations 2.3.6 – 2.3.13, the resonant frequency can be derived and is described in equation 2.3.14. Note that the frequency term contains all the design parameters including radius of the membrane, thickness of each layer and etch length shown in figure 2.3.4.

$$f = \frac{1}{2\pi} \sqrt{\frac{k}{m}} = 0.154 \sqrt{\frac{{Y_0}'' 38 \left((h_1 - h_p)^3 + (h_p)^3 \right) c(a,l,v,h_0,h_1,h_p)}{\rho}} \quad (2.3.14)$$

In equation 2.3.14, ${Y_0}''$ is the Young's Modulus of the material, ρ is the density of the material and υ is the Poisson's ratio of the material.

One last term that is to our interest is the transduction coefficient η. In order to find the transduction coefficient, we need to define coupling energy first. Coupling coefficient describes how well coupled the mechanical domain is to the electrical domain. The equation that describes coupling energy is shown below [1-3,64-73].

$$U_{coupl} = \eta V w_0 = \int_V e_{31,f}(\varepsilon_{rr} + \varepsilon_{\theta\theta}) E_3 dV = 2\pi e_{31,f} Z_p I_{Piezo} V w_0 \quad (2.3.15)$$

$$e_{31,f} = \frac{d_{31} Y_0}{1-\upsilon} \quad (2.3.16)$$

$$\varepsilon_{rr} = -z \frac{\partial^2 w(r)}{\partial r^2} \quad (2.3.17)$$

$$\varepsilon_{\theta\theta} = -\frac{z}{r} \frac{\partial w(r)}{\partial r} \quad (2.3.18)$$

From equations 2.3.15 – 2.3.18, we can define transduction coefficient as follows.

$$\eta = 2\pi e_{31,f} Z_p I_{Piezo} = e_{31,f} Z_p \chi^2 (-22 + 18\chi^2) \quad (2.3.19)$$

One term of interest in equation 2.3.19 is I_{Piezo} which is the integral of strains within the electrode area. It represents how well-coupled a certain electrode configuration is to a specific mode shape [1-3,64-73]. The equation of I_{Piezo} is shown below

$$I_{Piezo} = \int (\frac{\partial^2 \varphi}{\partial r^2} + \frac{1}{r} \frac{\partial \varphi}{\partial r}) r dr = (-3.482\chi^2 + 2.9184\chi^4) \quad (2.3.20)$$

From plotting equation 2.3.20 with varying electrode coverage χ, we found that the best coupling happens at 77% electrode coverage. The plot is shown in figure 2.3.5.

The results from equivalent circuit model of pinned PMUT and clamped PMUT are listed in table 2.3.1. We have listed important parameters such as mode shape, effective vibrating area, resonant frequency, transduction coefficient and dc displacement for comparison.

From the table, we observed that by modifying the mode shape, we have increased the effective vibrating area of a pinned PMUT from 33% of the total surface area to 42%. In addition, at the same resonant frequency, a pinned PMUT occupies 1.2 times smaller radius compared to a clamped PMUT which implies that more PMUTs can be arranged in an array with the same array area.

Pinned PMUT also shows 1.2 times improvement in transduction coefficient and 2 times increase in dc displacement at resonance compared to a clamped PMUT of the same radius.

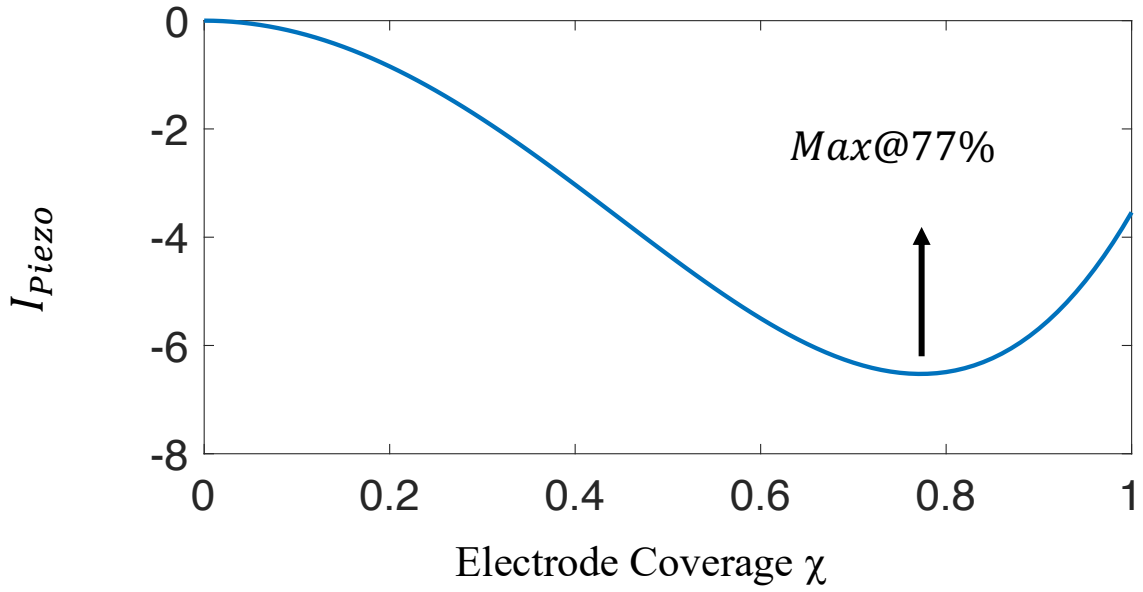

Figure 2.3.5. I_{Piezo} versus electrode coverage.

Table 2.3.1. Comparison of important design parameters between a clamped and pinned PMUT

	Clamped	Pinned	Conclusion
$\phi(r)$	$(1-(\frac{r}{a})^2)^2$	$1-1.741\left(\frac{r}{a}\right)^2+0.7296\,(\frac{r}{a})^4$	Modified mode shape
$A_{effective}$	$0.33A_{Total}$	$0.42A_{Total}$	1.2 times increase
f_0	$0.475\sqrt{\frac{Y_0^{"}{h_p}^2}{a^4\rho}}$	$0.154\sqrt{\frac{Y_0^{"}38\left(\left(h_1-h_p\right)^3+\left(h_p\right)^3\right)c}{\rho}}$	Radius reduced by 1.2 times at same resonant frequency
η	$8\pi e_{31,f}Z_p\chi^2(-1+\chi^2)$	$e_{31,f}Z_p\chi^2(-22+18\chi^2)$	1.2 times increase
w_{dc}	$\frac{9a^2e_{31,f}Z_p}{8Y_0^{"}h_p^3}$	$\frac{9a^2e_{31,f}Z_p}{4Y_0^{"}h_p^3}$	2 times increase

2.4 Simulation Results

This section explains the COMSOL Multiphysics v4.3 simulation model along with simulation results. Simulation results provide us with valuable information of the design, for example, the mode shape and frequency response of the design. Figure 2.4.1 shows the simulation setup using axisymmetric acoustic-structure-piezoelectric module. The geometry of PMUT is realized in the solid domain, where the left axis is the symmetry axis. The device is fixed along the right boundary as shown in the zoomed diagram. The entire structure is realized by revolving around the symmetry axis as shown in the zoomed diagram.
Voltage is applied between the bottom and top surface of the active piezoelectric layer in the electrical domain. The acoustics domain contains a standard acoustic domain and a perfectly matched layer to model infinite space. Perfectly matched layer (PML) absorbs outgoing waves and do not reflect the waves at the interface and the wave entering PML exponentially decay and thus the solution in the standard acoustic domain is not affected [74].

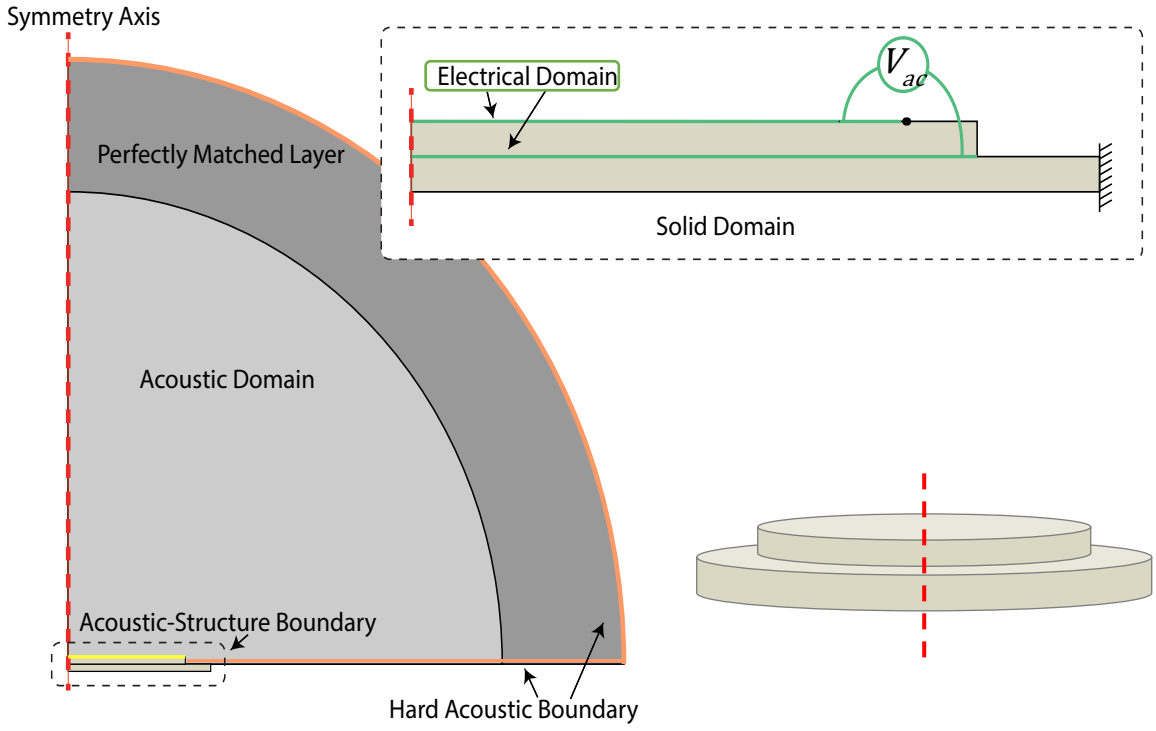

Figure 2.4.1. COMSOL Multiphysics v4.3 Simulation Setup of pinned PMUT.

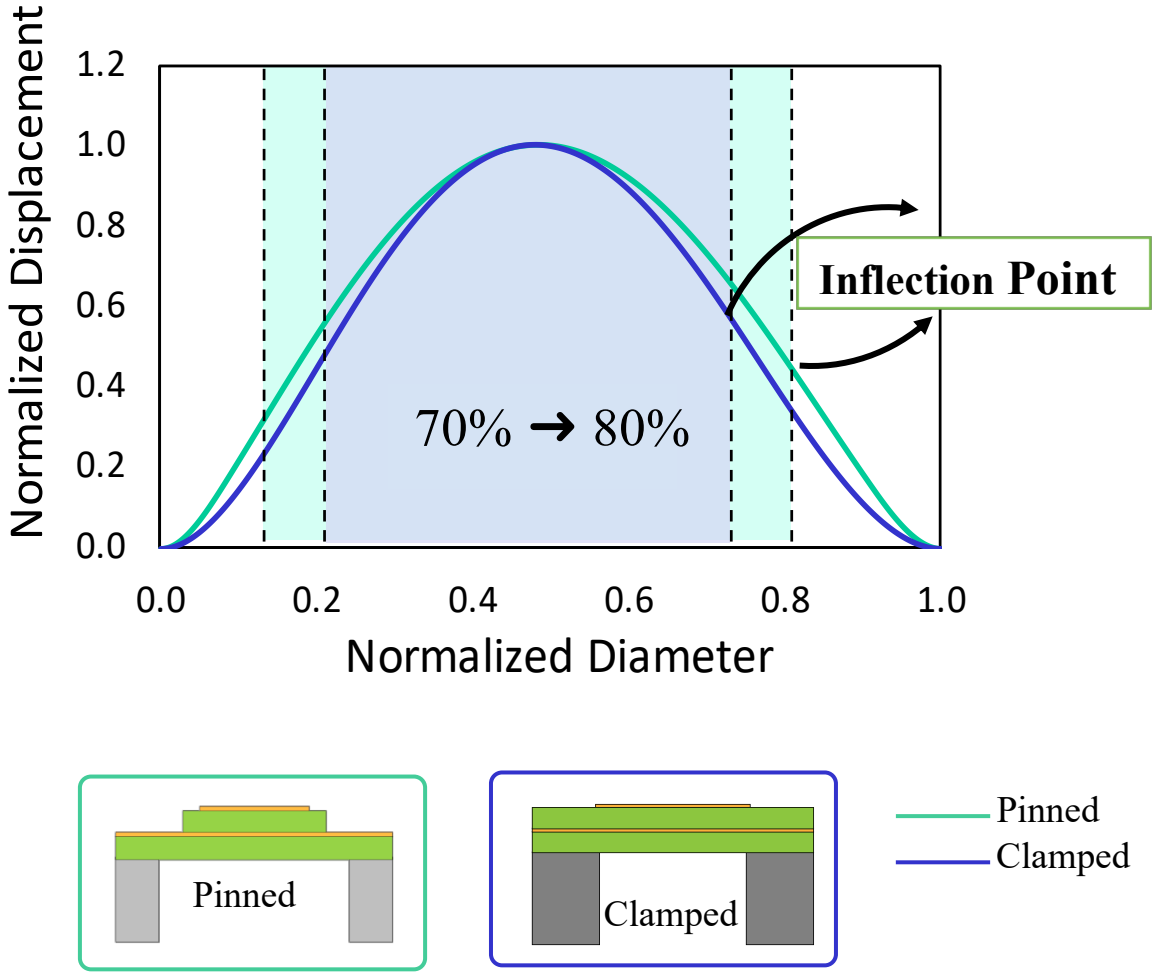

Figure 2.4.2. Comparison of simulated mode shape between a pinned PMUT design and a clamped PMUT design.

Figure 2.4.2 shows the simulated mode shape comparison between the pinned and the clamped design. The blue curve shows mode shape of the clamped design and the green curve shows the pinned design. In addition, both radius and displacement are normalized. The clamped design is simulated and later fabricated for ease of comparison.

For a clamped design, the curvature changes sign at 70% of radius. Thus, the electrode should only cover 70% of the plate radius for best coupling [47]. For

the pinned design, we see that the inflection point has moved out from 70% of radius to 80% of the radius and the inflection happens at where we etch away the material. Thus, from simulation results, we can claim that we have successfully modified the mode shape from clamped to pinned and we have also successfully increased the electrode coverage area.

Figure 2.4.3 shows the simulated frequency response result of the pinned boundary PMUT. A traditionally clamped PMUT with the same film stack with either the same radius or same resonance frequency is also simulated for comparison and the results are shown in the same figure. In figure 2.4.3, we simulated the result of the center displacement per volt of a pinned PMUT with 91 um radius in diaphragm and we see that the pinned PMUT shows a 983 nm/V peak displacement at resonance. On the other hand, the clamped PMUT shows a 368 nm/V peak displacement at the same resonance frequency with a diaphragm radius of 107 um. In addition, the clamped design with same diaphragm radius as the pinned design shows a 307 nm/V displacement at slightly higher resonance frequency. Both numbers are smaller than the pinned design and we see a 167% to 220% improvements in the displacement per volt output at resonance [47].

Note that the 167% improvement in center displacement per volt output at resonance matches with equivalent circuit model results which gives us 2 times increase.

One other thing that's worth noting is that, under the same radius with the same film stack, the pinned PMUT shows lower resonance frequency which we think is due to the reduced diaphragm stiffness from the change of mode shape and the etched away material at the boundary of the top layer of the film stack.

Figure 2.4.4 shows the simulated results of the pressure output per volt at a distance of 2 mm away from the transducer surface comparing the pinned and clamped PMUT design. From the figure, we see that the pinned PMUT gives a 38 Pa/V peak pressure output at resonance where the clamped one gives only 11 Pa/V peak pressure output at the same resonance frequency. This translates to a 227% improvement in pressure output per volt or 10 dB enhancement [47].

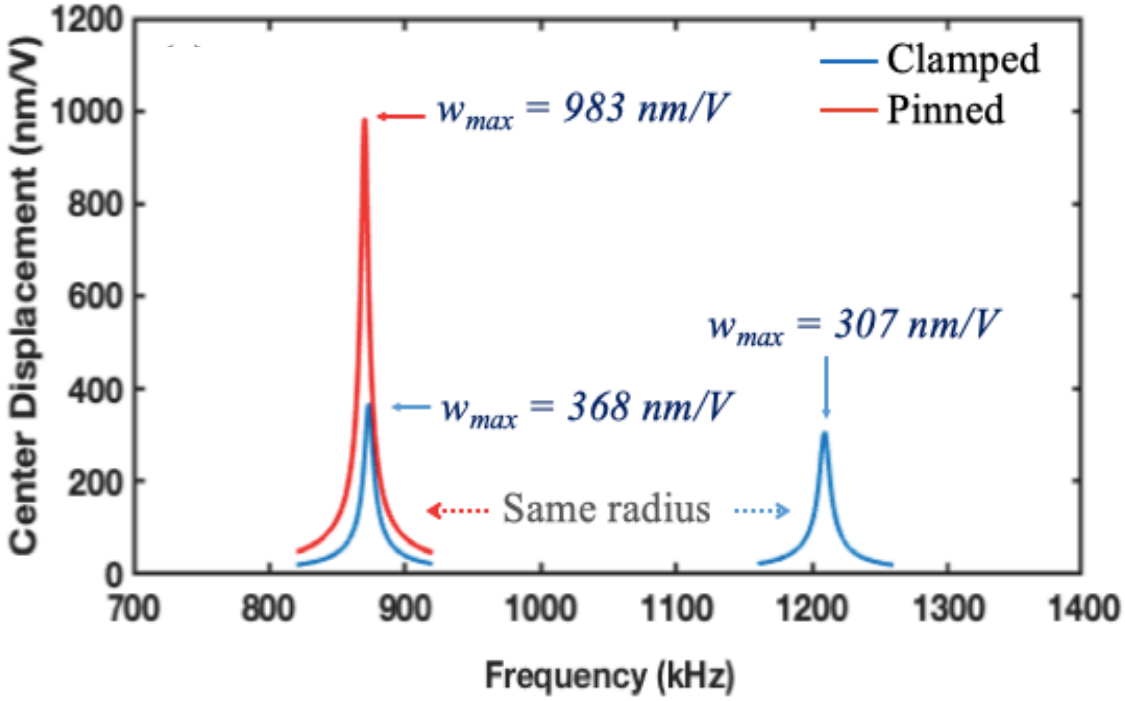

Figure 2.4.3. Simulated center displacement per volt for pinned and clamped PMUT.

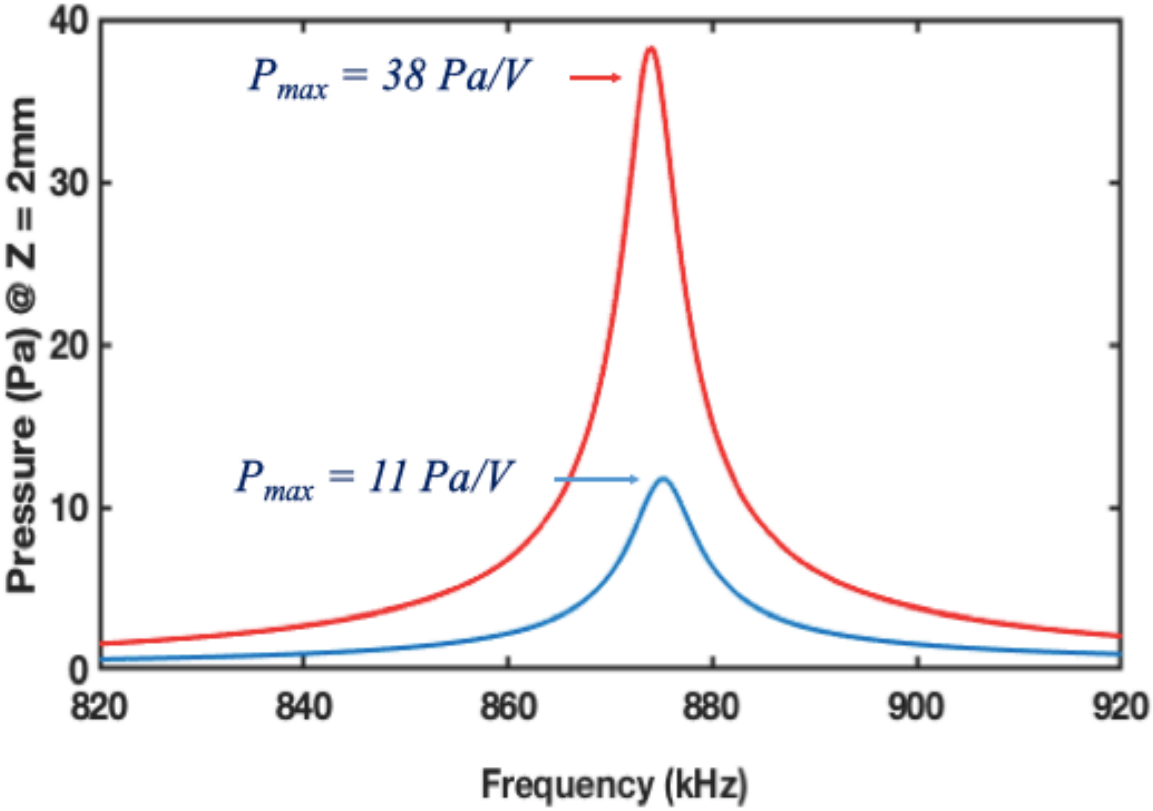

Figure 2.4.4. Simulated pressure output per volt for pinned and clamped PMUT.

Figure 2.4.5. shows results of simulated electromechanical coupling coefficient k^2 of a pinned and clamped PMUT at the same resonant frequency. From the figures, we see that the pinned PMUT gives a 2.39% coupling coefficient where the clamped PMUT gives a coupling coefficient of 1.48%. This translates to a 61% improvement in the electromechanical coupling which also supports out claim that the pinned PMUT will transfer more mechanical energy from electrical energy and thus more center displacement at resonance which lead to enhancement in pressure output of the overall device [47].

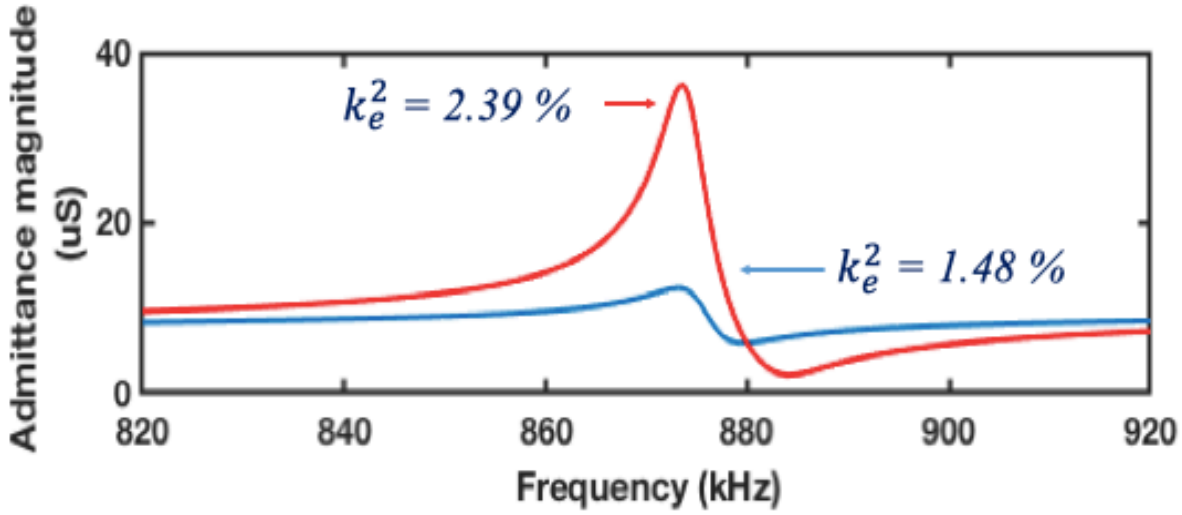

Figure 2.4.5. Simulated coupling coefficient for pinned and clamped PMUT.

2.5 Fabrication Process

This section explains the fabrication process of the pinned PMUT.

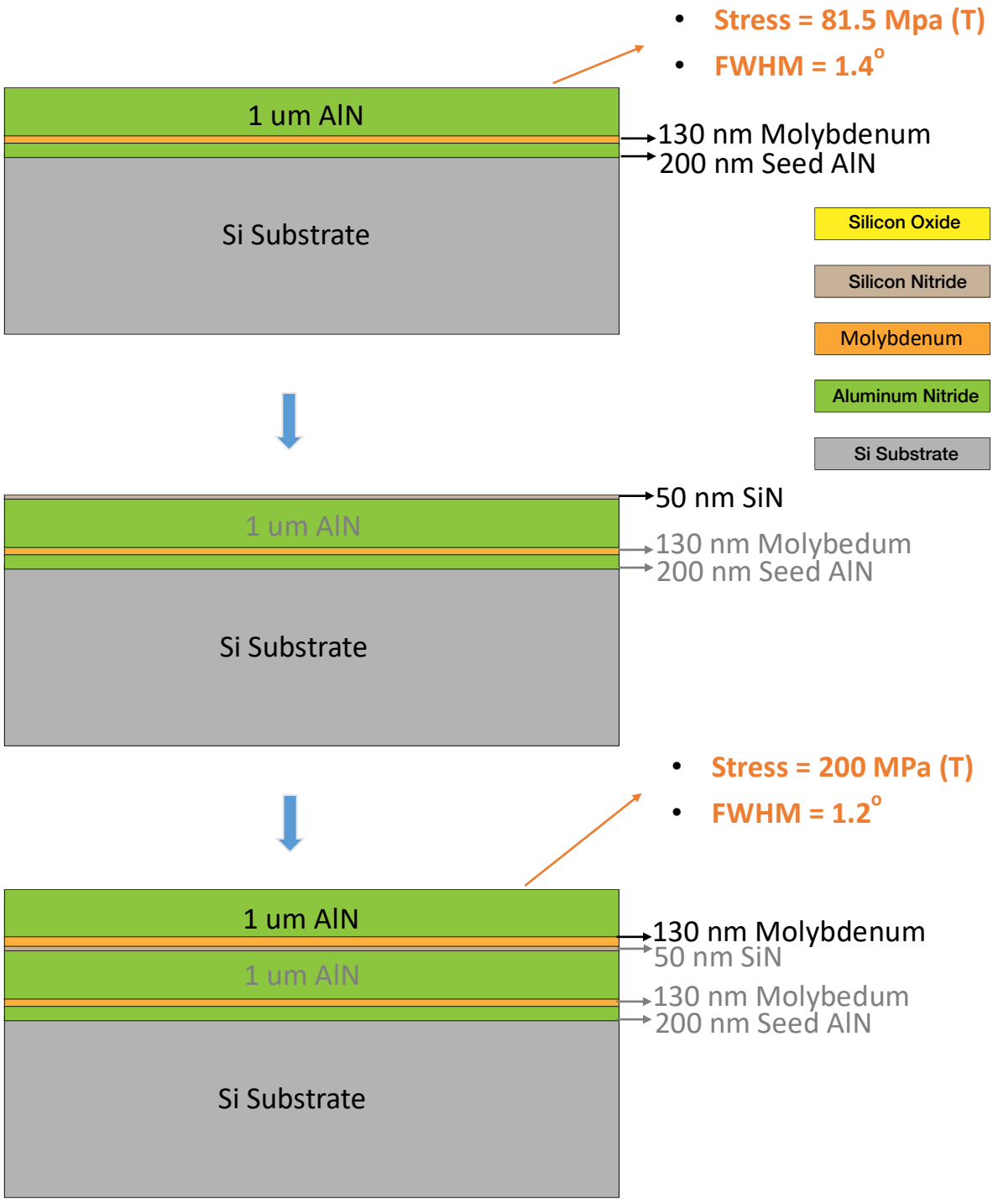

Figure 2.5.1. Fabrication process flow of thin-film deposition of each layer.

The fabrication process is adapted from the same process flow for DEB PMUT that is previously developed in our group [59]. We start by sputter deposition of a 200 nm-thick layer of seed AlN layer on silicon substrate and followed by a 130 nm-thick layer of Molybdenum as the ground electrode. After that, we sputter deposit a 1 um thick AlN layer as the non-active piezoelectric layer. The purpose of the seed layer is to ensure the quality of sputtered AlN. The above process is shown in figure 2.5.1.
The measured film stress of AlN is 81.5 MPa of stress in tension and the bow is negative 25.4 um. We also measured the full width half max (FWHM) of AlN film using x-ray diffractometer to monitor its quality and we found it to be 1.4-degree as shown in figure 2.5.2. From literature, any number below 1.7 degree will give us reasonable PMUT performance [75-76].
We then deposit 50 nm thick layer of Nitride to prevent conduction through AlN layer. And we sputter another 130 nm thick layer of Mo as the bottom electrode.

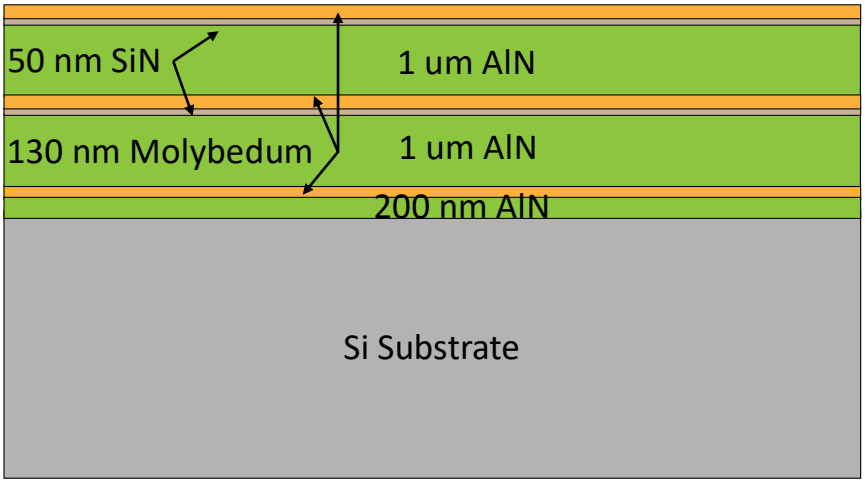

Figure 2.5.2. Complete film stack of sputtered layers.

The last step is to sputter deposit a 1 um-thick layer of AlN as the active piezo layer. We get a film stress of 200 MPa in tension and a FWHM of 1.2 degree. We finish the film stack by deposit 50 nm-thick Nitride layer, and 130 nm -thick top Moly electrode layer.

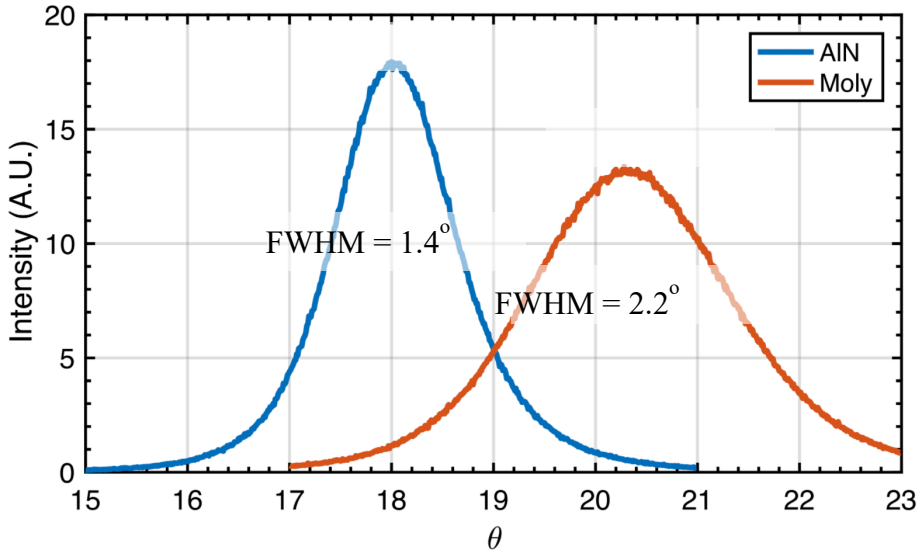

Figure 2.5.3. XRD of bottom device layers showing FWHM of AlN and Moly

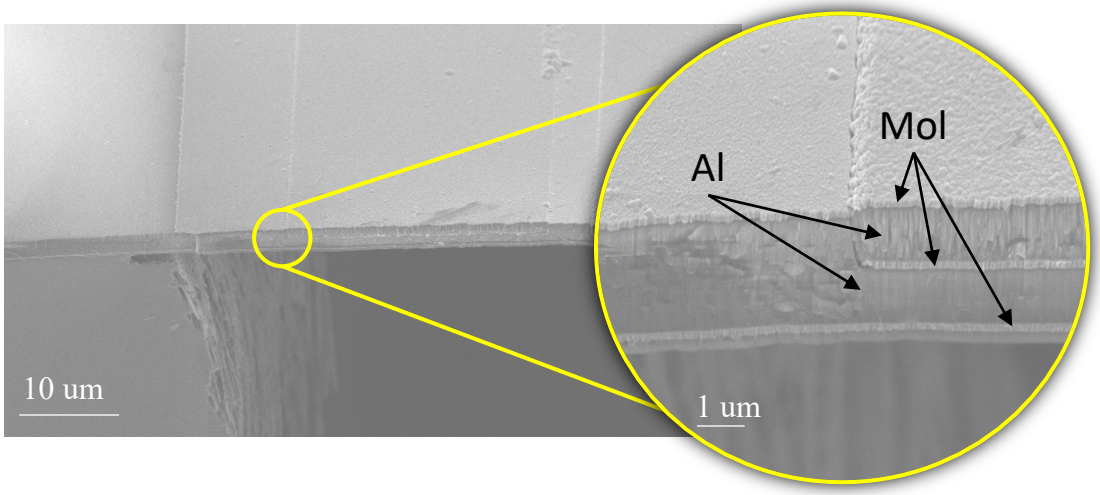

Figure 2.5.4. SEM of cross-sectional view of the film stack.

The SEM shows a cross-sectional view of the film stack. We can see that AlN crystals are aligned vertically which again ensures the piezoelectric quality. The next step is to pattern and etch the electrode and Nitride with fluorine-based plasma etching. We then pattern and etch AlN to achieve the pinned boundary and to access the bottom electrode using chlorine-based plasma etching.

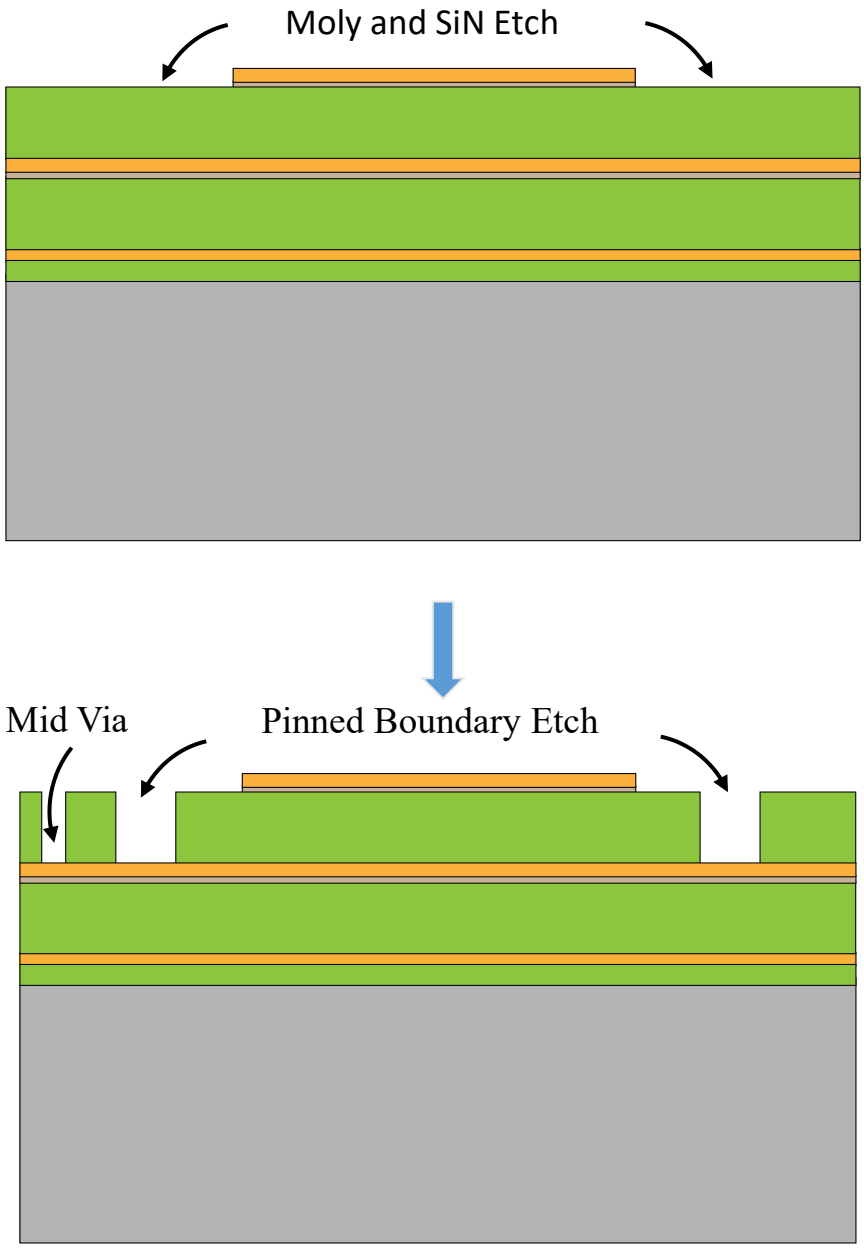

Figure 2.5.5. Etch of top AlN layer to access electrodes and to achieve the pinned design.

The last step of fabrication is to free the membrane by etching away the silicon layer form below using deep ion reactive etching (DRIE).

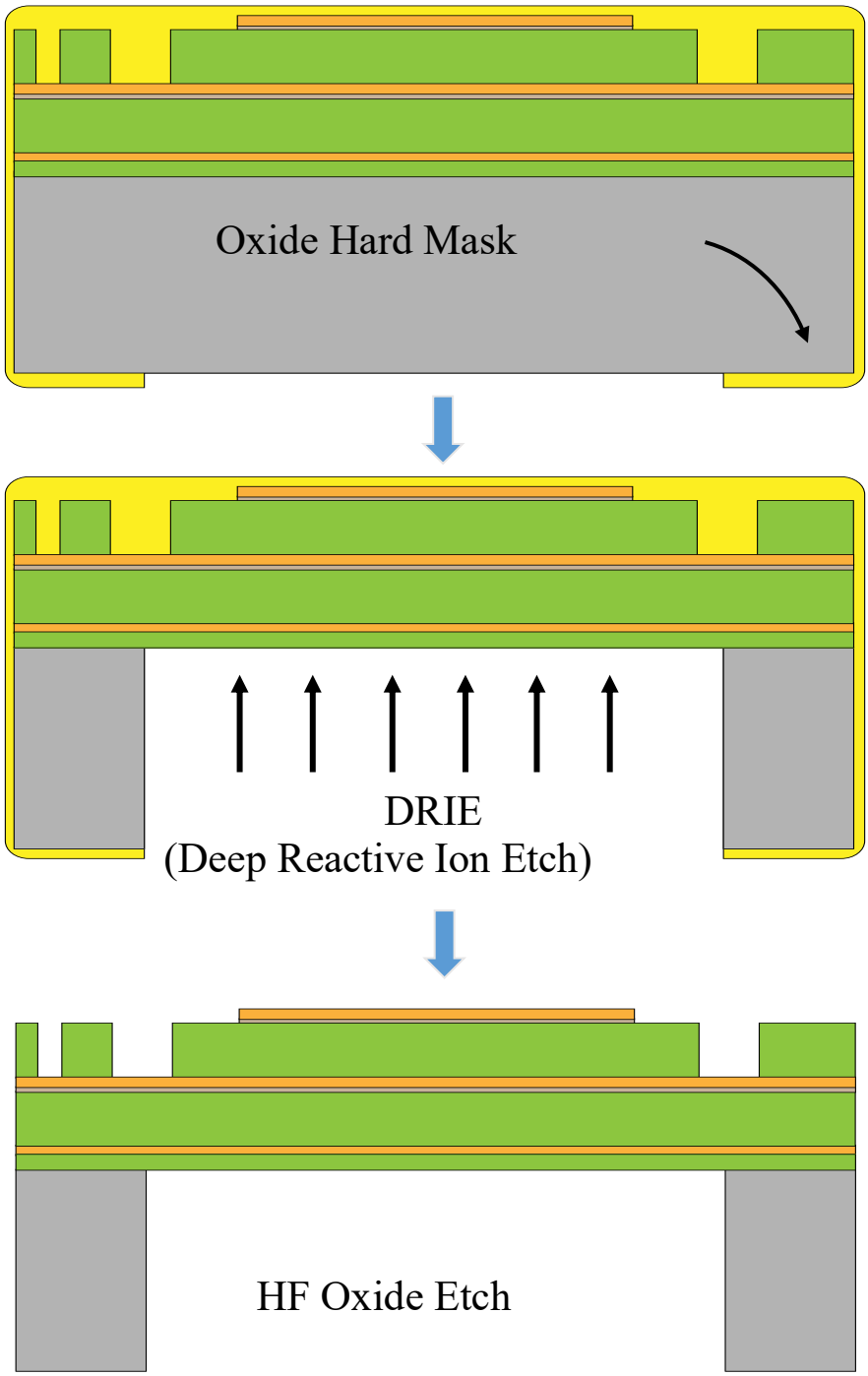

Figure 2.5.6. Backside DRIE and membrane release.

We start by depositing oxide to protect the front device layer and to act as a hard mask for DRIE silicon etch. We then etch the silicon wafer and monitor the etch profile with a confocal microscope as shown in figure 2.5.7. We can see from SEM in figure 2.5.4 that the resulted DRIE is fairly straight.
After we are done with etching, we send the wafer to a company to dice the wafer into smaller chips for characterization which will be described in the next section. Lastly, after we get the chips back from the company, we dip each chip in HF for 90 seconds to remove any excess Oxide. We then finish up by performing a standard wafer cleaning before wire bonding.

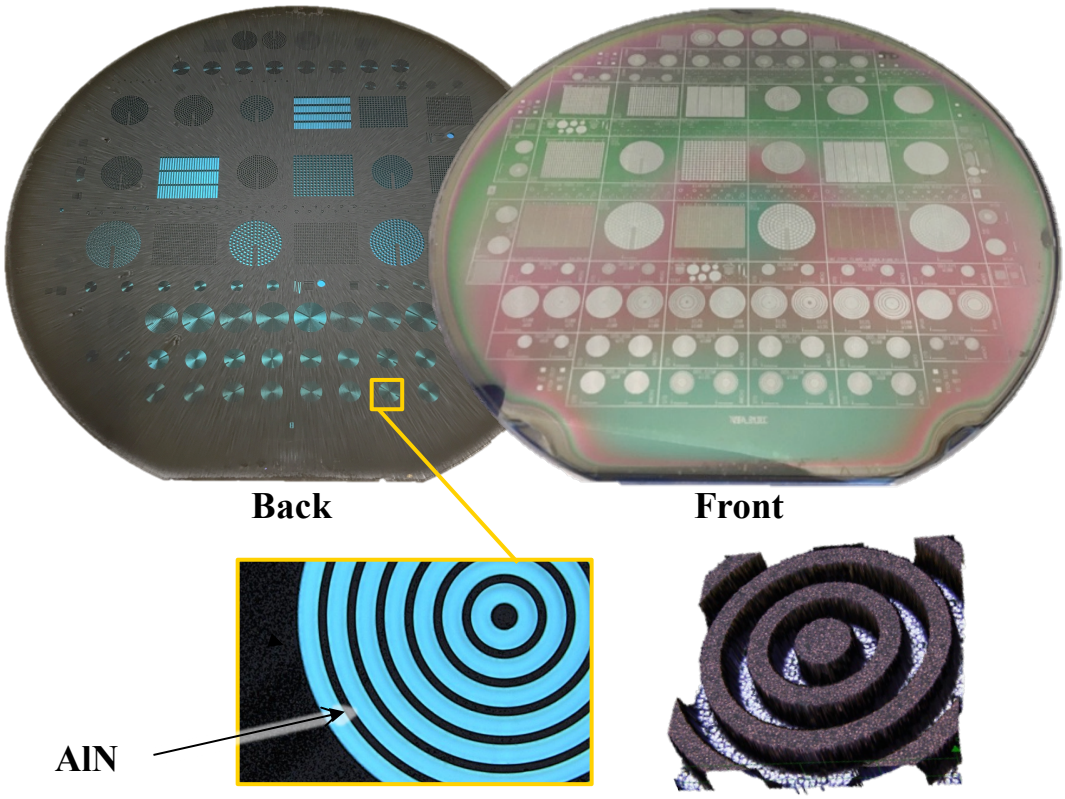

Figure 2.5.7. Confocal microscopy of the entire wafer for DRIE monitor.

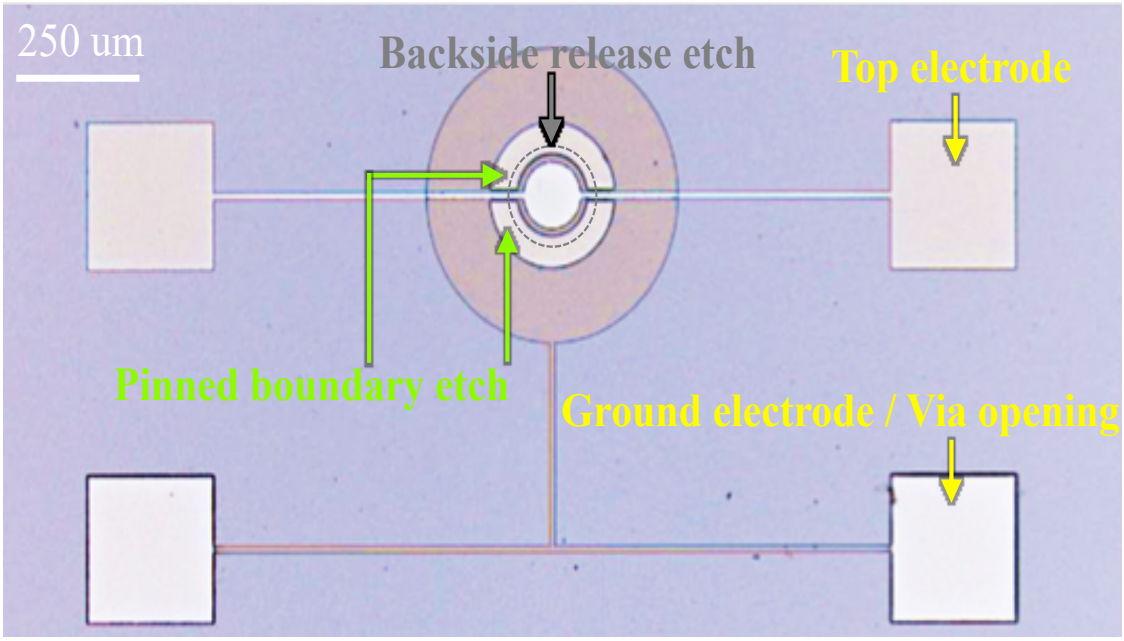

Figure 2.5.8. An optical image of a fabricated device showing the top electrode, the via opening to access bottom electrode, the pinned boundary etch, and sketched backside release etch.

Figure 2.5.8 shows the optical image of a fabricated device taken using the same confocal microscopy. The top electrode, ground electrode and via opening are indicated in yellow and the pinned boundary etch is indicated in green. The top electrodes are connected to two bond pads for the ease of wire bonding. The backside release etch is sketched in grey dashed line for clarity.

2.6 Experimental Results

This section shows the experimental results of the pinned PMUT with center displacement and pressure output being evaluated and compared to simulation results.

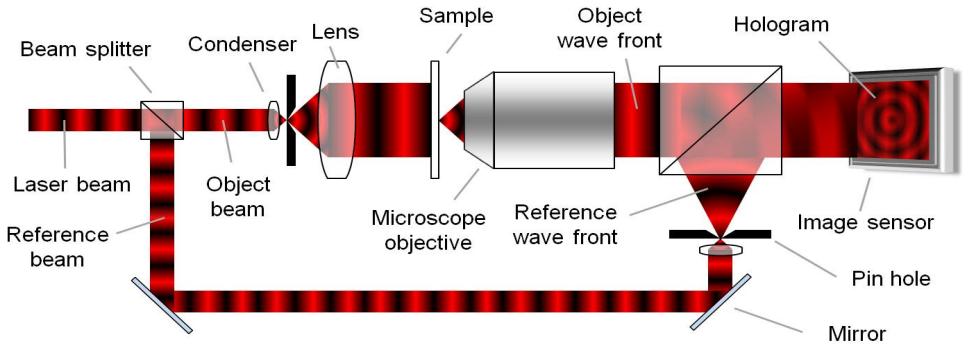

Source: Wikipedia

Figure 2.6.1. Illustration of working principle of a digital holographic microscope (DHM).

We accessed the digital holographic microscope (DHM) thanks to Prof. Ming Wu's group's help. A DHM splits a laser beam into an objective beam and a reference beam. The objective beam is focused onto the sample and the light reflected is collected to form an interference pattern with the reference beam. And we call this pattern the hologram. Difference in height along the sample surface results in a difference in phase. And thus, we can use DHM to find the displacement amplitude of a sample. Figure 2.6.1 shows the working principle of a DHM.

Figure 2.6.2 (a) shows the desktop image of the SUT. Figure 2.6.2 (b) shows the wiring of the SUT where the fabricated device is glued onto a PCB with header pins mounted for electrical connection to the PMUT. A function generator is connected to the header pins with the laser setup directed on top of the SUT.

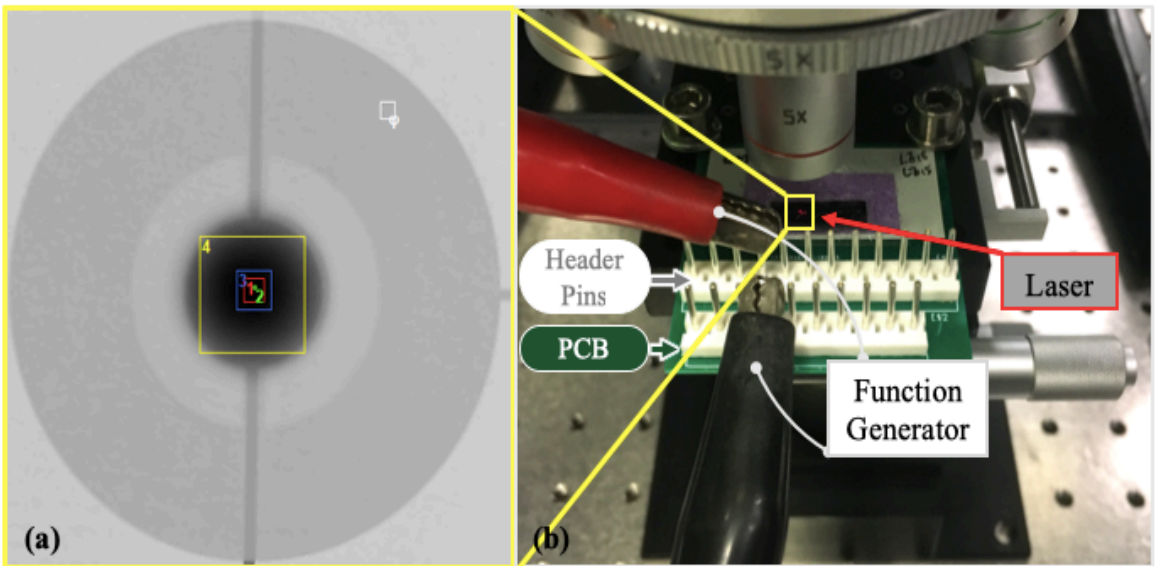

Figure 2.6.2. Optical image of the sample under test using DHM. (a) Desktop image of the sample under test. (b) Digital image of a sample under test with header pins wired to a function generator and laser pointed at the PMUT sample under test shown in figure 2.6.2 (a).

The mode shape of each sample is collected at locations on the sample as shown in figure 2.6.3 (a). Figure 2.6.3 (b) shows the comparison between experiment and simulation results of both pinned and clamped design with both radius and displacement normalized. As shown in the figure, experimental results show strong agreement with simulation results.

The mode shape of an ideal free-free plate is drawn in black dashed lines for comparison as well. We can see that it matches closely to that of the pinned PMUT mode shape from both experimental result and simulation result up to 80% of the radius.

With the successfully modified mode shape, we have increased the electrode coverage of the pinned PMUT to an optimal number of 80% of its radius. This is 10% extra compared to that of a clamped PMUT which is 70% of the radius. This indicates that we have increased the amount of active piezoelectric area. In addition, we have increased the effective vibrating area of the PMUT from modifying its mode shape from clamped to pinned.

By sweeping the frequency we can get the frequency response of each sample. We compared experimental results of both pinned and clamped PMUTs as shown in figure 2.6.4. The PMUTs are fabricated at different radius and we are comparing center displacement per volt of both cases at two resonant frequencies.

Figure 2.6.4 (a) shows the frequency response of the PMUTs. Figure 2.6.4 (b) shows the gain of the PMUTs and figure 2.6.4 (c) shows the phase information of the PMUTs.

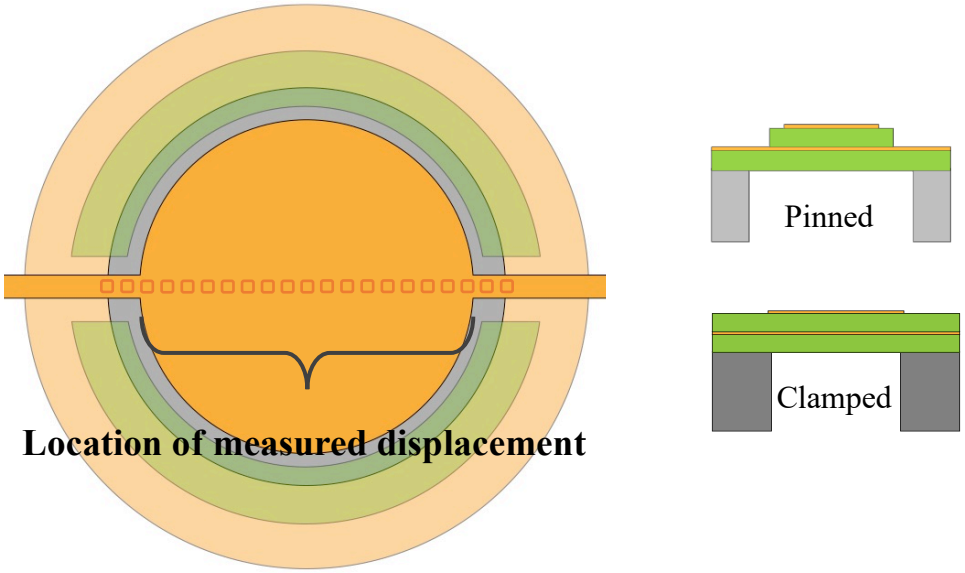

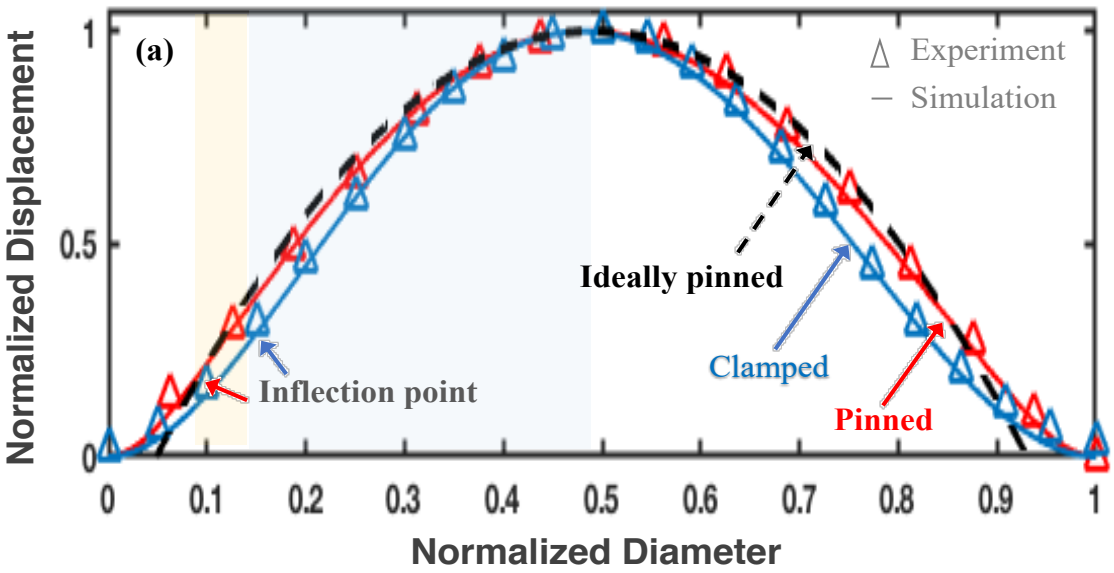

Figure 2.6.3. Results of mode shape measured using DHM. (a) Location of recorded frequency response on the SUT. (b) Measured mode shape of both clamped and pinned PMUT with mode shape of an ideally pinned PMUT for reference.

As shown in figure 2.6.4, the purple and yellow curves are frequency response of the clamped PMUT, and the red and blue curves are the frequency response of the pinned PMUT. At the lower resonant frequency, the pinned PMUT shows a 218.2 nm/V peak center displacement at resonance while the clamped one shows a 87.4 nm/V peak center displacement at resonance. At the higher resonant frequency, the pinned PMUT shows a 231.9 nm/V peak center displacement at resonance while the clamped one shows a 95.4 nm/V peak center displacement at resonance. These numbers translate to a minimum of 150% improvement in peak displacement per volt at resonance which also matches pretty well with simulation results which gives us 167% improvement.

With the combined enhancement of both center displacement at resonance and the modified mode shape, we have successfully improved the volumetric velocity of the PMUT. The combined 150% improvement in displacement and 1.2 times increase in effective vibrating area translates to an estimated 3.3 times improvement in the pressure output comparing to a traditionally clamped PMUT.

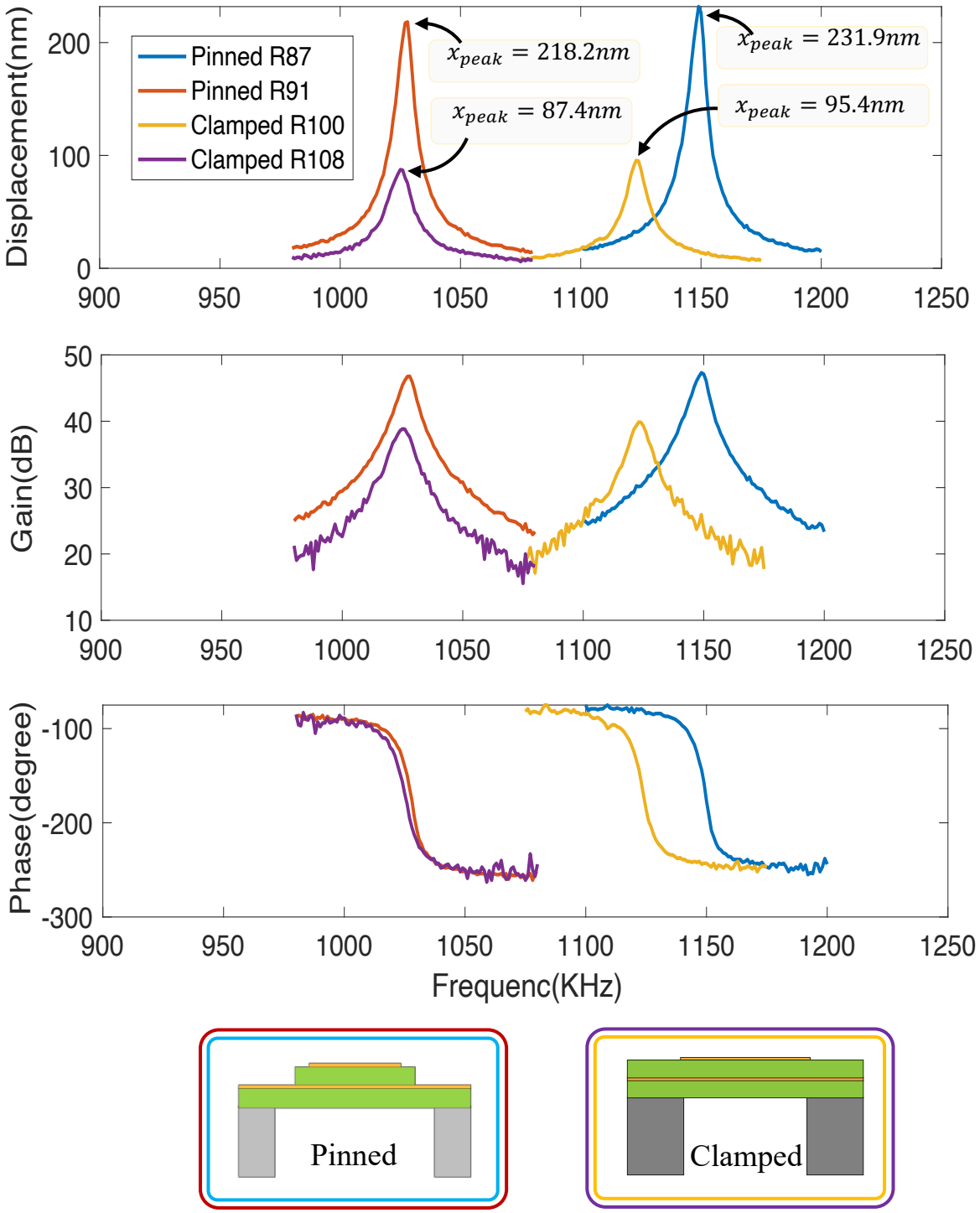

Figure 2.6.4. Experimental results of frequency response of pinned and clamped PMUT. (a) Experimental results of center displacement versus frequency. (b) Experimental results of gain versus frequency. (c) Experimental results of phase versus frequency.

2.7 Conclusion

In this chapter, we demonstrated the working principle of a pinned PMUT. We started by showing the design concepts of the pinned boundary PMUT using schematics. We then proved the concept simulation model. After that, we utilized analytical modeling to validate our simulation model results.

The device is then drawn on masks using L-Edit in preparation of fabrication. After that, we fabricated the device in the Berkeley Marvell Nanofabrication Lab using tools from sputter deposition to wet etching, SEM, and XRD. In the end, we characterized the fabricated chips using DHM and we see matching results between simulation model and experimental results.

The fabricated device is shown to have 3.3 times boost in acoustic pressure output at resonance compared to a traditional clamped PMUT without any added fabrication complexity. These PMUT are expected to expand the application space mainly for air-coupled operations.

Chapter 3

Dual – Electrode Pinned PMUT

3.1 Introduction

The performance boost form pinned PMUT brings us a lot of possibilities of using PMUTs in various applications as both a transmitter and receiver. However, such PMUTs can only operate as either a transmitter (TX) or a receiver (RX). Certain applications require same chip TX and RX functionalities and the current pinned PMUT design is having limitations. As a result, we started to look at possibilities of altering the PMUT design based on the existing pinned PMUT to enable same chip TX and RX functionality.

One way of achieving this goal is to put pinned PMUTs into array and arrange the single PMUT elements in a way such that half of the array element are wired together and serve as a transmitter and the other half of the array element are wired together and serve as a receiver. We can arrange the PMUTs to be mixed with each other to allow this functionality as demonstrated in figure 3.1.1. In the schematics, all the PMUT elements are of the same design except that all the green ones are wired together, and the blue ones are wired together but separate from the green ones. We can use either ones as TX or RX as we desire.

The drawback of this arrangement is that it requires complicated wiring to wire all the single PMUTs without interfering with the neighboring elements. In addition, the areal distribution of PMUT elements are spread out which can also impede the PMUT performance.

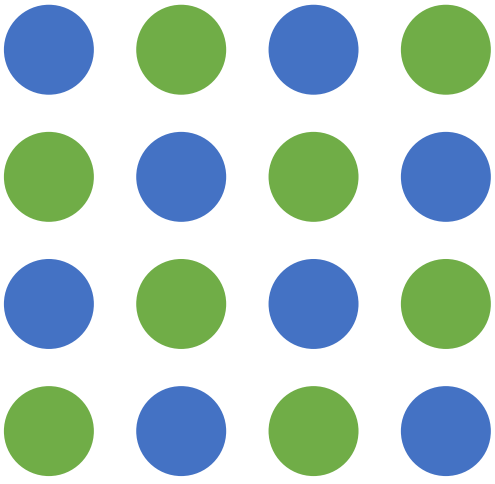

Figure 3.1.1. Schematics of mixed PMUT arrangement for same chip TX and RX functionality.

As a result, we are looking at other alternatives such that a standalone PMUT can have TX and RX functionality at the same time. The dual-electrode pinned PMUT can provide the same amplitude improvement as the original pinned PMUT and yet serves the purpose of same chip TX and RX functionality.
The detailed design concept is covered in section 3.2. Simulation setup of such design is provided in section 3.3 and the simulation results are listed in section 3.4

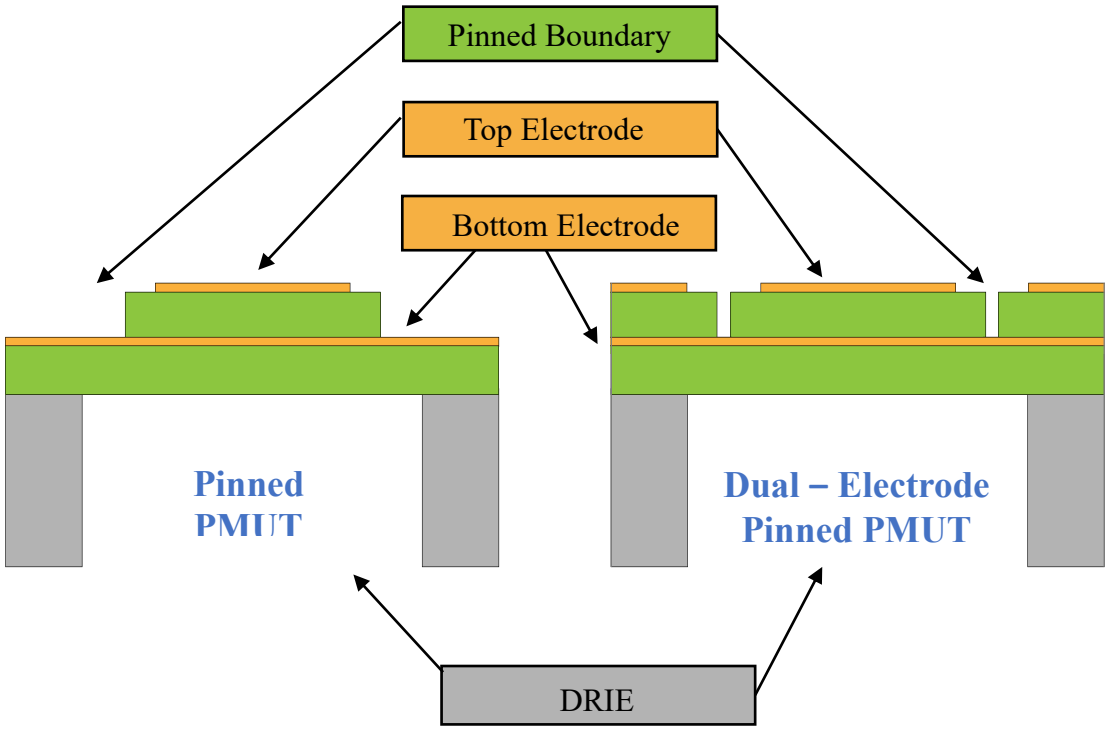

Figure 3.2.1. Cross-sectional schematics comparison of original pinned PMUT and dual-electrode pinned PMUT.

3.2 Design Concept

The cross-sectional view of the dual-electrode pinned PMUT is shown in figure 3.2.1. and the cross-sectional view of the original pinned PMUT is also shown for comparison.

As shown in the figure, in the original pinned PMUT, the pinned boundary etch happens at 80% of diaphragm radius and the entire outer edge is etched away. In comparison, for the dual-electrode pinned PMUT, the pinned boundary etch happens at 65% of radius which is close to the original 70% inflection point of a clamped PMUT.

The ratio of inner and outer electrode is decided based on simulation results and will be covered in detail in later sections. Similar to the pinned PMUT design, the dual-electrode pinned PMUT design provides similar acoustic performance boost when the inner and outer electrodes are excited altogether.

In addition, the dual-electrode design only etches away of free a small region of the membrane while keeping the outer electrode to enable the same chip TX and RX functionality.

The complete 3D schematics of the film stack is shown in figure 3.2.2. From the figure, the pinned boundary etch is shown and the top and bottom electrodes are shown in orange. The active layer and the structural layer are shown in green. And the backside release etch is shown in grey.

Similar to the original pinned PMUT design, we use Aluminum Nitride as the piezoelectric material and Molybdenum as the electrodes.

As we apply a potential difference between the top and bottom electrodes, the device vibrates into a clamped plate mode shape similar to a traditional clamped PMUT but with increased vibrational amplitude. Alternatively, we can use either the inner or outer electrode portion as the TX element and the other electrode as the RX element to achieve the same chip TX and RX functionality. The detailed results on mode shape and frequency response will be covered in the later sections.

With the dual-electrode pinned PMUT design, we are able to achieve same chip TX and RX functionality with improved acoustic performance without any added fabrication complexity.

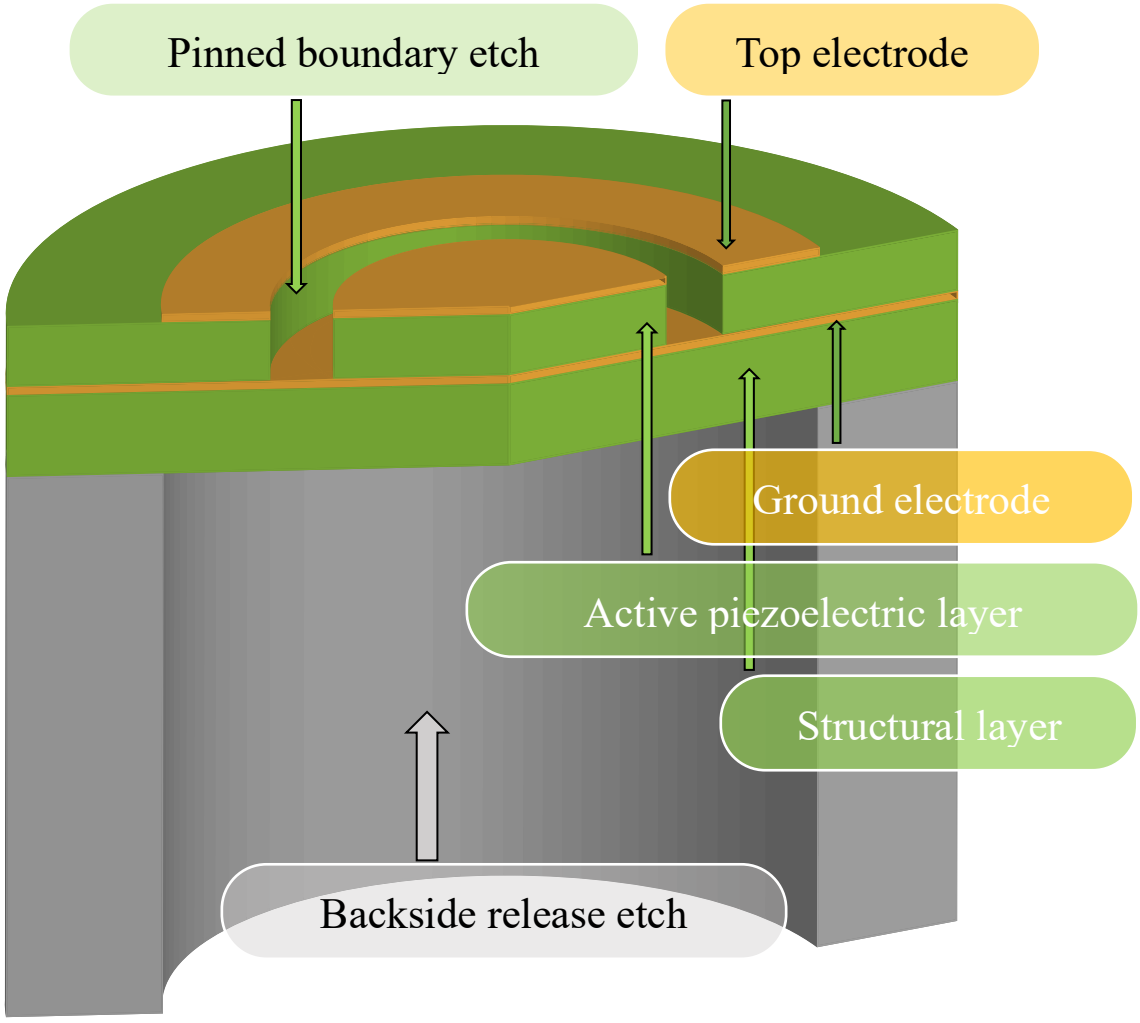

Figure 3.2.2. 3D schematics of the dual-electrode pinned PMUT with complete film stack.

3.3 Simulation Setup

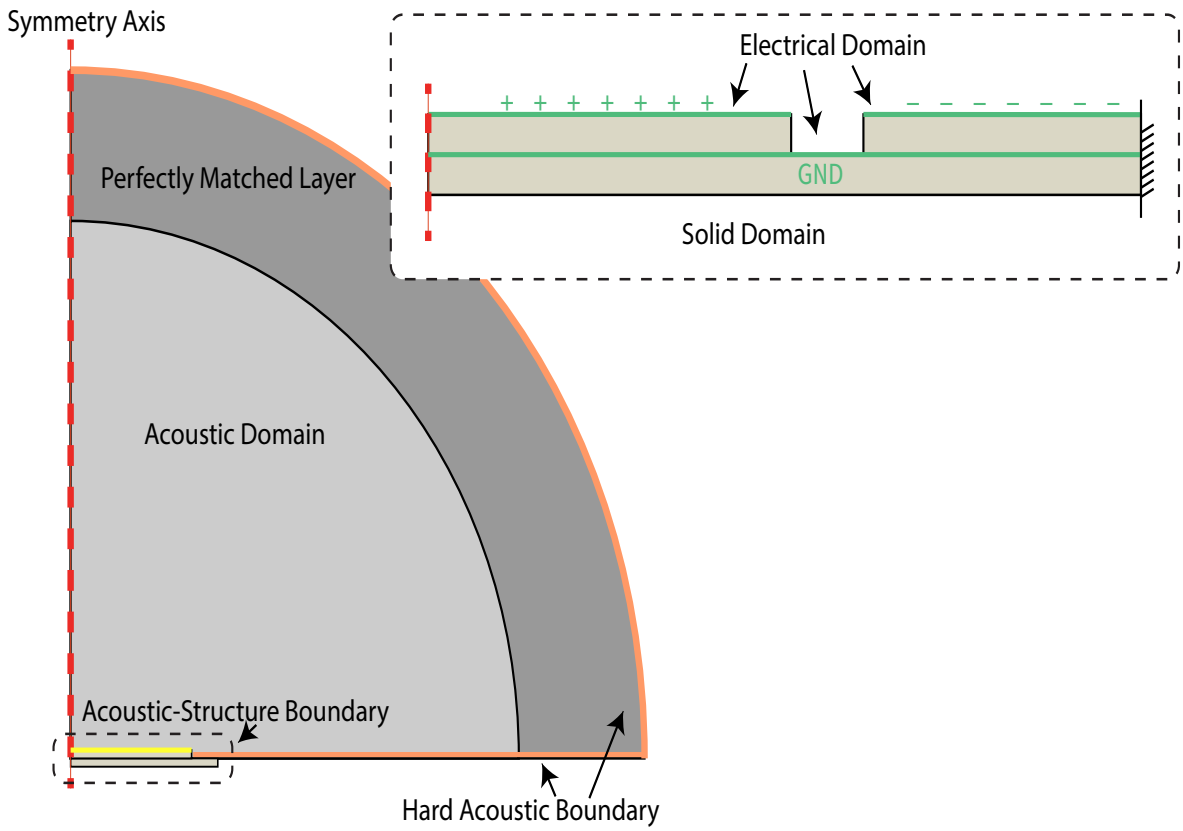

Figure 3.3.1. Simulation setup of dual-electrode pinned PMUT.

The simulation setup of the dual-electrode pinned PMUT is shown in figure 3.3.1. The cross-sectional view of the dual-electrode pinned PMUT is shown in figure 3.2.1.

Similar to the simulation setup of the original pinned PMUT, the simulation is realized using COMSOL Multiphysics v4.3 with axisymmetric acoustic-structure-piezoelectric module.

The left axis labeled with red dashed line is the symmetry axis. The device is fixed along the right boundary and revolves around the symmetry axis. In the solid domain, we have the device structure designed with etch happens at the inflection point.

In the electrical domain, the inner and outer electrodes are either excited only one-sided for single chip TX and RX functionality or differentially to achieve similar performance compared to the original pinned PMUT. The acoustics domain contained a regular acoustic domain and a perfectly matched layer to simulate the effect of infinite space.
We designed the PMUTs to have a resonant frequency of around 850 kHz to compare the frequency response between the original pinned PMUT and the dual-electrode pinned PMUT, and to compare the mode shape among the original pinned PMUT, the dual-electrode pinned PMUT, and a traditional clamped PMUT. The detailed parameter selection along with simulation results will be explained in the next section.

3.4 Results and Discussions

This section covers the simulation results including parameter selection and results comparison with the original pinned PMUT.
The mode shape comparison of the dual-electrode pinned PMUT, the original pinned PMUT, and the traditional clamped PMUT is shown in figure 3.4.1.
In figure 3.4.1, the yellow curve shows the mode shape of the original pinned PMUT, the blue curve shows the mode shape of the dual-electrode pinned PMUT and the green dashed curve shows the mode shape of the traditional clamped PMUT. We can see that the mode shape of the dual-electrode pinned PMUT is very similar to that of the traditional PMUT where the inflection point happens at approximately 70% of the radius of the diaphragm.
The mode shape shown here for the dual-electrode pinned PMUT is resulted from the mode shape of the dual-electrode pinned PMUT which gives the best performance after a parametric study varying the ratio of inner electrode radius to outer electrode radius and the corresponding etch width. For our purpose of maintaining the same output pressure comparing to the original pinned PMUT while enabling the same chip TX and RX functionality, best performance refers to the result that gives us similar center displacement per volt at resonance when both inner electrode and outer electrode are excited differentially compared to the original pinned PMUT while outputting similar center displacement per volt comparing results when either inner electrode or outer electrode is excited.

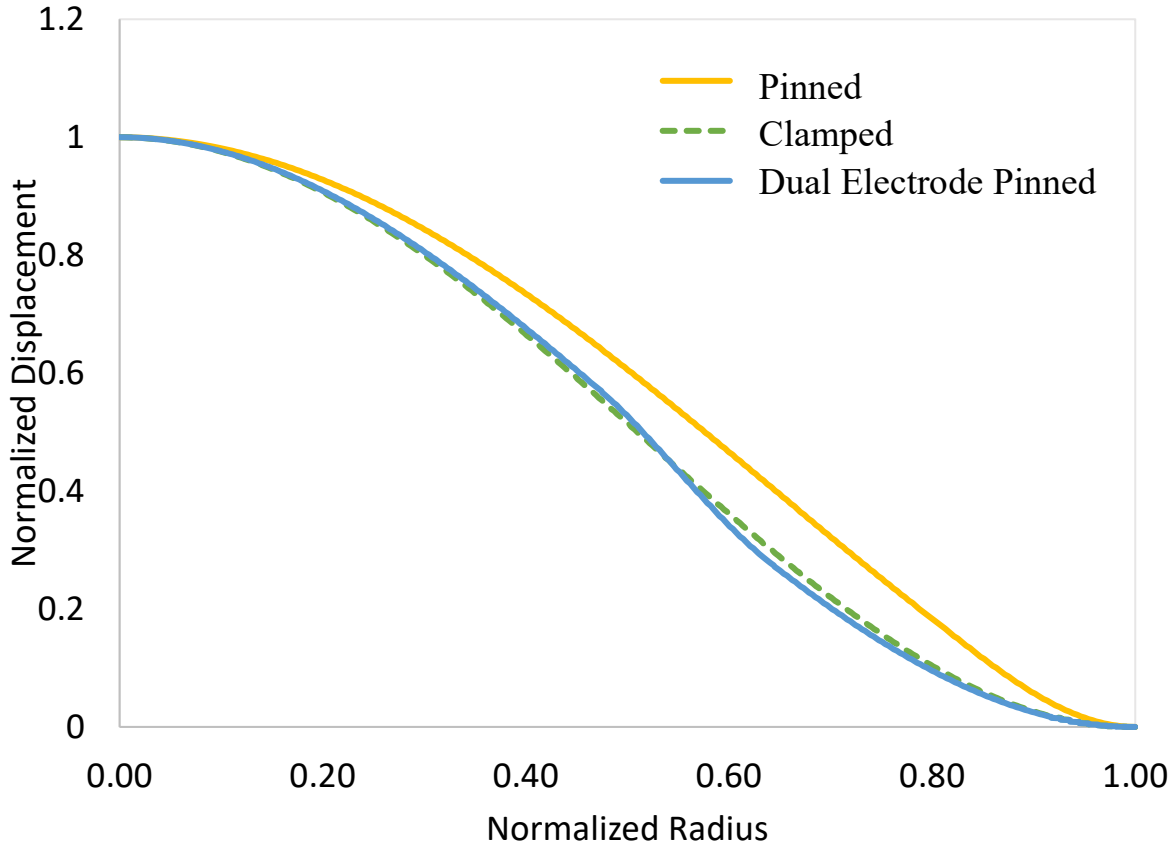

Figure 3.4.1: Simulated mode shape comparison of the dual-electrode pinned PMUT, the original pinned PMUT and a traditional clamped PMUT.

From simulation result, we get the best performance when we set the etch length l_e to be 20% of the diaphragm radius r, inner electrode length r_{in} to be 57% of diaphragm radius minus etch length and outer electrode length r_{out} to be 43% of diaphragm radius minus etch length as described in the following equations.

$$l_e = 0.2r \tag{3.4.1}$$

$$r_{in} = 0.57(r - l_e) \tag{3.4.2}$$

$$r_{out} = 0.43(r - l_e) \tag{3.4.3}$$

Figure 3.4.2 shows the frequency response of the dual-electrode pinned PMUT and the original pinned PMUT. In figure 3.4.2, the orange dashed line represents the frequency response of the dual-electrode PMUT when only inner electrode is being excited, the blue dashed line represents the frequency response of the dual-electrode PMUT when only outer electrode is being excited. The solid blue line represents the frequency response of the dual-electrode PMUT when inner and outer electrodes are being excited differentially and the solid yellow line represents the frequency response of the original pinned PMUT with a diaphragm radius of 92 um at the same resonance frequency compared to the dual-electrode pinned PMUT with a diaphragm radius of 109 um.

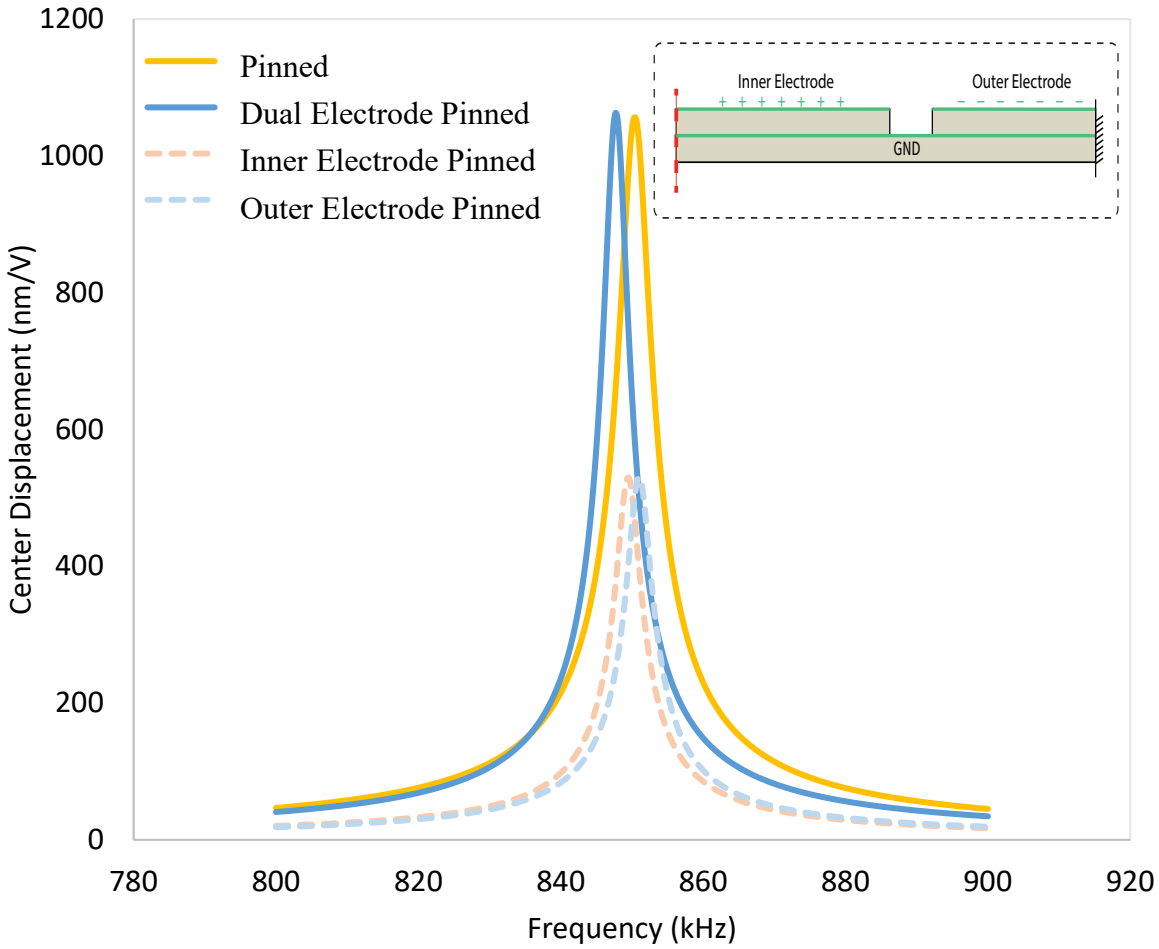

Figure 3.4.2. Simulated frequency response comparison of the dual-electrode pinned PMUT and the original pinned PMUT.

From figure 3.4.2, we can see that when only inner electrode is being excited, the device outputs 510 nm/V center displacement at resonance. When only outer electrode is being excited, the device outputs 510 nm/V center displacement at resonance, which is the same as when only inner electrode is being excited. When inner and outer electrode are both driven differentially, the device outputs 1059 nm/V center displacement at resonance, which is approximately two times larger compared to those when only inner or outer electrode is being excited. The original pinned PMUT also outputs 1059 nm/V at the same resonance frequency compared to that of the dual-electrode pinned PMUT.
With simulation results of both mode shape and frequency response, we confirm the feasibility of realizing same chip TX and RX functionality using the dual-electrode pinned PMUT.

3.5 Conclusion

In this chapter, we started by explaining the reason and need of the dual-electrode pinned PMUT, followed by the design concept of such device. We then covered the details of simulation setup in COMSOL Multiphysics v4.3, and parameter selection of the device. We finished by showing simulation results of both mode shape and frequency response of the dual-electrode pinned PMUT.
The mode shape of the dual-electrode pinned PMUT follows that of a traditional clamped PMUT where the inflection point happens at approximately 70% of the diaphragm radius. When only inner or outer electrode is being excited, the dual-electrode pinned PMUT has the center displacement per volt under resonance at half of the value of that when both electrode are excited differentially. The original pinned PMUT outputs similar center displacement per volt at resonance compared to that of the dual-electrode pinned PMUT when driven differentially. As a result, we conclude that we've successfully designed a dual-electrode pinned PMUT that provides the same performance as the original pinned PMUT while enabling single chip TX and RX functionality.

Chapter 4

Pinned PMUT for Tilt Sensing

4.1 Introduction

With the success of designing the pinned PMUT that provides improved center displacement per volt at resonance and pressure output, we explore the possibilities of using such PMUT for various applications. One of such applications is tilt sensing.

Tilt sensing has broad applications such as angle determination for automotive operations and the control of solar panels [77-78]. Researchers have investigated the possibilities of using CMUTs as ultrasonic tilt sensor before [48]. However, their work uses the time-of-flight method to determine the tilt angle which suffers from difficulties in determining the onset of echoes. In addition, no one has explored the possibility of using PMUTs for ultrasonic tilt sensing.

This work investigated the feasibility of utilizing the pinned PMUT structure to determine the tilt angle based on the receiving PMUT's pressure amplitude. The advantages of using PMUTs over CMUTs is that it requires no high DC bias voltage and has no thin gap restriction [23-27]. In addition, using the pressure amplitude instead of time-of-flight method based on the pulse-echo mode, there is no issue with determining the onset of echoes. The improved electromechanical coupling coefficient also guarantees the improvement in sensitivity of using the pinned PMUTs as a receiver.

4.2 Concept and Device Fabrication

The schematics of the experimental setup is shown in figure 4.2.1.

In figure 4.2.1, the transmitting (TX) and receiving (RX) PMUT elements are glued onto a printed circuit board (PCB). The PCB provides electrical connection to power source, function generator, oscilloscope, etc. The PCB along with the PMUT elements is then mounted onto the platform.

A reflector fixed onto the platform changes its tilt angle both clockwise and counterclockwise. The TX element is electrically excited which then launches an ultrasonic wave to the air. This launched ultrasonic wave is then reflected to the RX element. The schematics demonstrated two scenarios when the reflector is at two different counterclockwise tilt angles. With the difference in tilt angle, the reflected pressure/voltage received at the RX element will be different. We

can thus determine the tilt angle based on the sensor output pressure/voltage measured at the RX element.

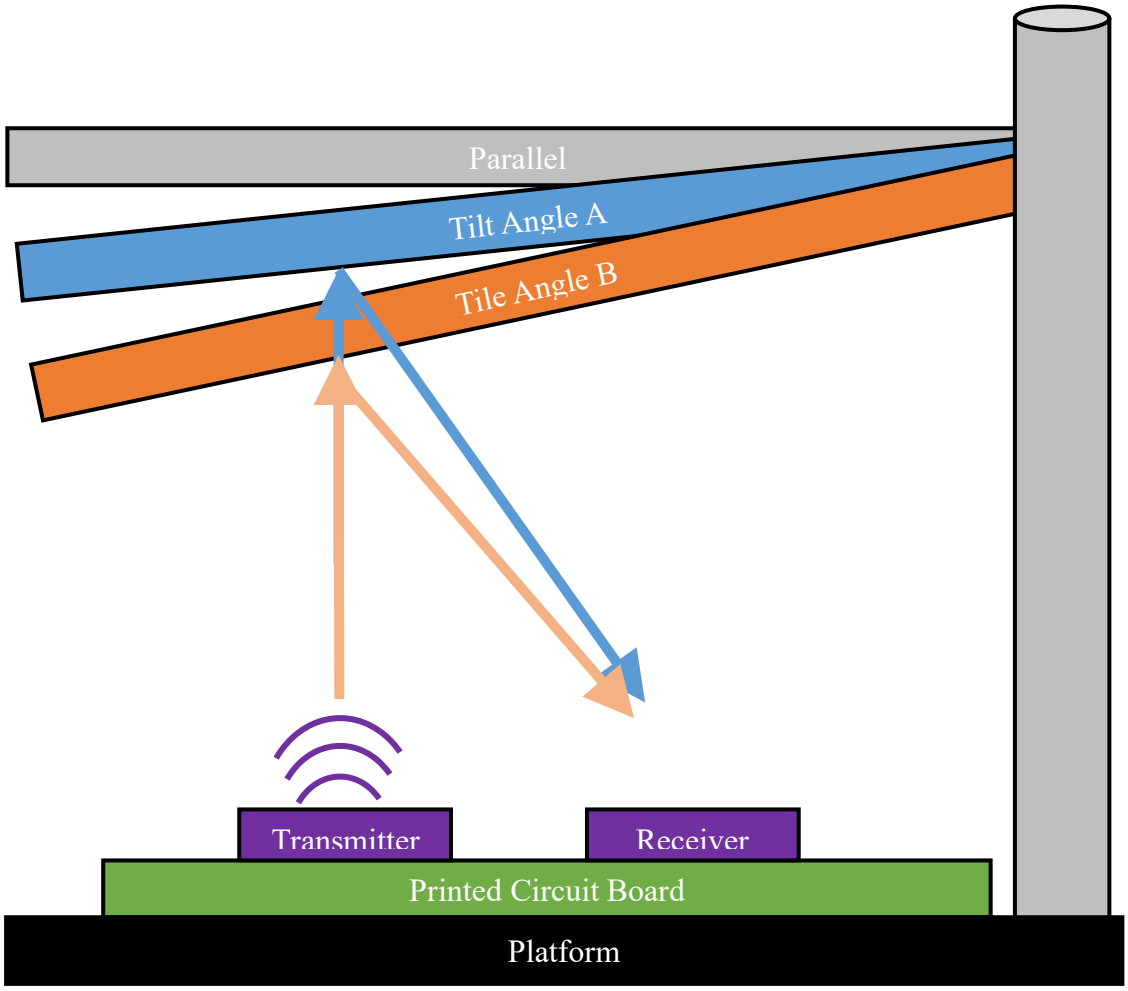

Figure 4.2.1. Schematic view and operational principal of the ultrasonic tilt sensor demonstrating counterclockwise tilt.

Figure 4.2.2 shows the arrangement of standalone pinned PMUTs as an array element. Both the transmitting and receiving PMUT elements are arranged in the same way.

As shown in figure 4.2.2, an array element is consisted of 6x15 standalone PMUTs. Each PMUT has a radius of $a = 275\ \mu m$ and the pitch between each standalone PMUT is $p = 750\ \mu m$. Each array element is 11 mm in length and 3.5 mm in width.

Figure 4.2.3 shows the fabrication process of such PMUT array which is similar to that described in section 2.5.

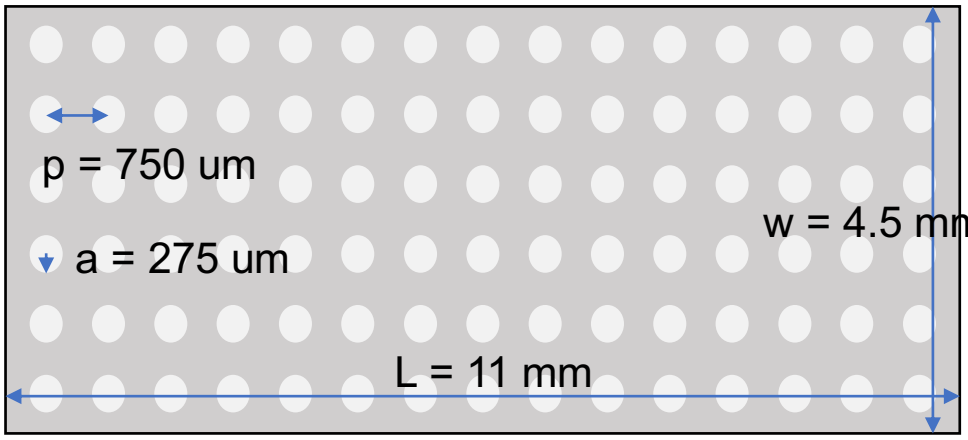

Figure 4.2.2. Schematic view of the pinned PMUT array element arrangement.

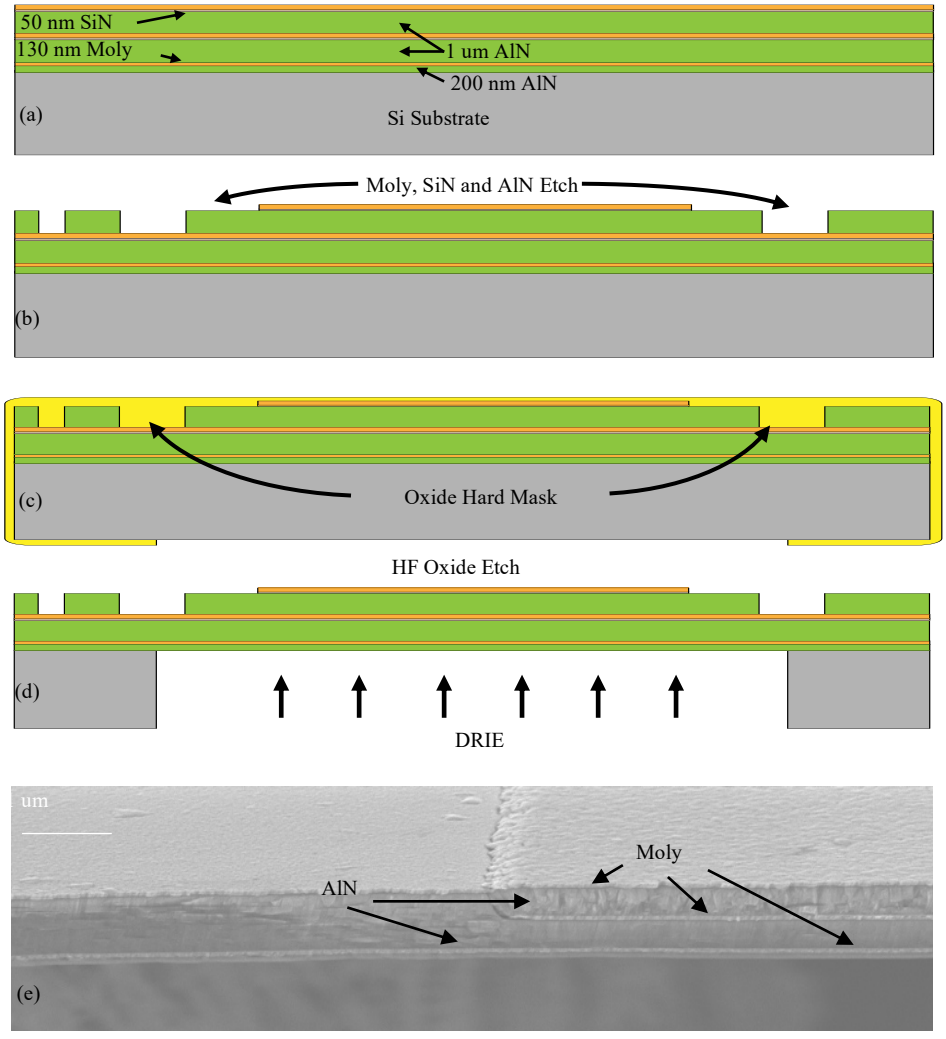

Figure 4.2.3. Fabrication process flow of the pinned PMUT array (a) Deposition of AlN and Mo. (b) Patterning of top Mo electrode, SiN barrier layer and AlN. (c) Deposition of oxide hard mask. (d) Backside DRIE to free the membrane and HF oxide etch to remove the oxide hard mask. (e) SEM of cross-sectional area of the fabricated PMUT.

4.3 Theoretical Modeling

We established a theoretical model with analytical equations to help predict the behavior of our ultrasonic tilt sensor based on the layout of our array elements. First, we need to determine the directivity pattern of the PMUT array. The directivity $D(\theta)$ of the array is governed by the following equation [1-3,18-22].

$$D(\theta) = \frac{\sin(kwsin(\theta)/2)}{Nsin(kpsin(\theta)/2)} \frac{48J_3(kasin(\theta))}{kasin(\theta)} \tag{4.3.1}$$

$$k = \frac{2\pi}{\lambda} \tag{4.3.2}$$

In equation 4.3.1, the first term is the directivity pattern of a rectangular array of size $w \times L$ and the second term is the directivity pattern of a circular PMUT with diaphragm radius a, k is the wave number of the medium and is dependent on wavelength, N is the number of PMUTs in the direction of flow or in our case the vertical direction in as shown in figure 4.2.2, and p is the pitch between each PMUT element. Equation 4.3.1 is a proven equation according to the multiply theorem [1-3] where the directivity pattern is a multiplier of the directivity of each pattern. The second term is also well studied according to Yipeng et al [27]. The derived directivity pattern is shown in figure 4.3.1 with a beam angle of $-60°$ to $+60°$ with array dimension as labeled in figure 4.2.2. Based on the directivity pattern/the far-field acoustic pressure, we can predict the receiving amplitude of pressure/voltage at the receiving element once we know the distance between the TX and RX element and the operational frequency.

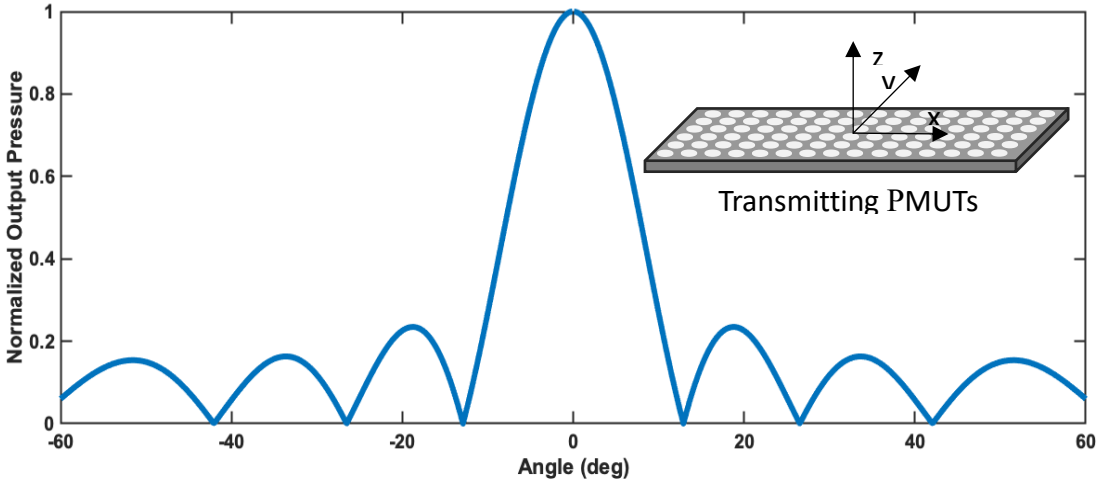

Figure 4.3.1. Theoretical far-field acoustic pressure from a TX element with dimensions as drawn in figure 4.2.2.

The relative change of the receiving PMUT element is resulted from the change of tilting angle which leads to a change receiving angle from the directivity angle along with a change in the length of acoustic path. The relative change in tilt angle is defined in the following equation [55].

$$\emptyset = tan^{-1}(\frac{y}{2h}) \tag{4.3.3}$$

Where h is the height between the PMUT array and the reflector plate as shown in figure 4.3.2.

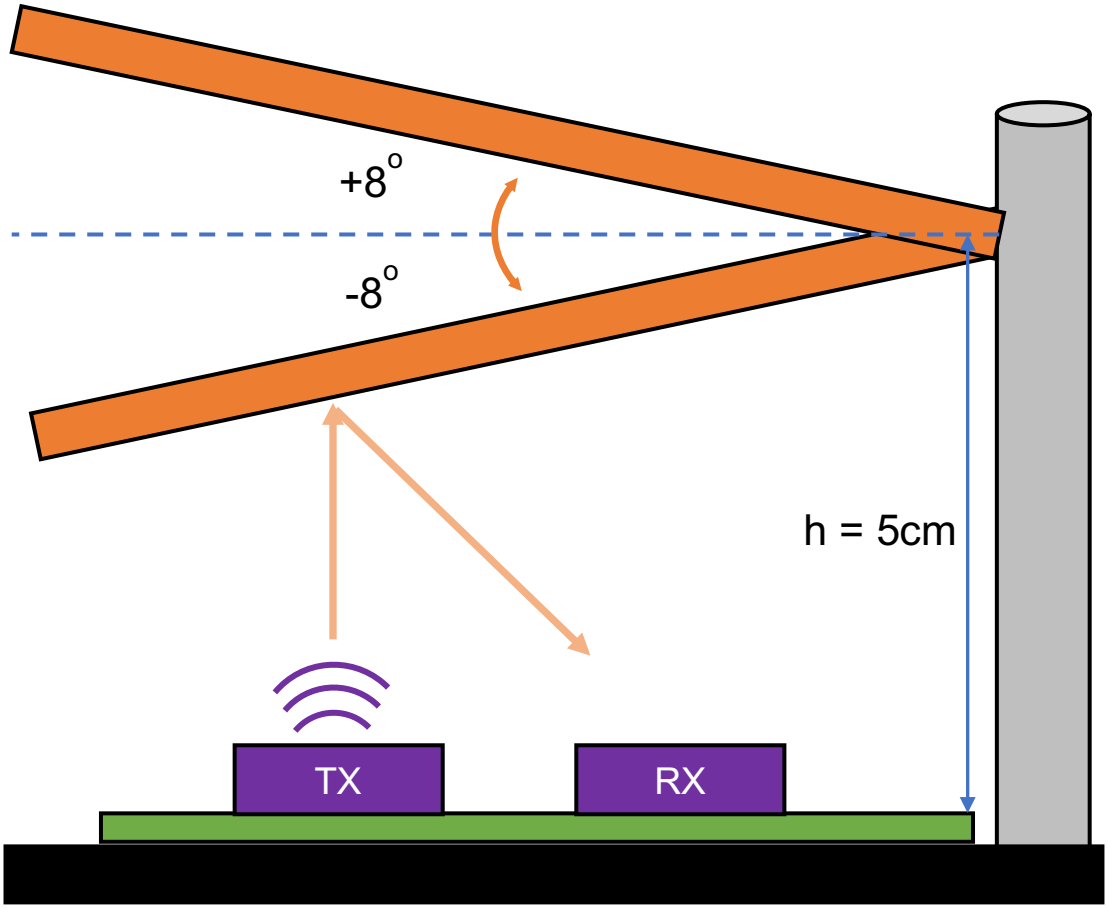

Figure 4.3.2. Schematics of experimental setup with parameters labeled.

The pressure seen at the receiving PMUT array can then be expressed with tilt angle, the directivity pattern and the reflector height as shown below [55].

$$p(w_0) = \int_{w_0-w}^{w_0+w} D(\theta - \emptyset)dy \tag{4.3.4}$$

Where w_0 is the distance between the transmitting and receiving PMUT array and in our case $w_0 = 6.75\ mm$. Table 4.3.1 listed the parameter values being used in the theoretical model.

Table 4.3.1. List of parameters used in the theoretical model

Parameter	**Value**
Reflector Height h	$5\ cm$
TX and RX Separation Distance w_0	$6.75\ mm$
PMUT Radius a	$275\ \mu m$
Pitch p	$750\ \mu m$
Array Width w	$4.5\ mm$
Array Length L	$11\ mm$

Figure 4.3.3 shows the results of theoretical simulation based on equation 4.3.4 and parameters listed in table 4.3.1. In figure 4.3.3, we varied tilt angle from -8 degrees to +8 degrees with pressure normalized. Using this approach, we are assuming that any near-field effect is negligible.

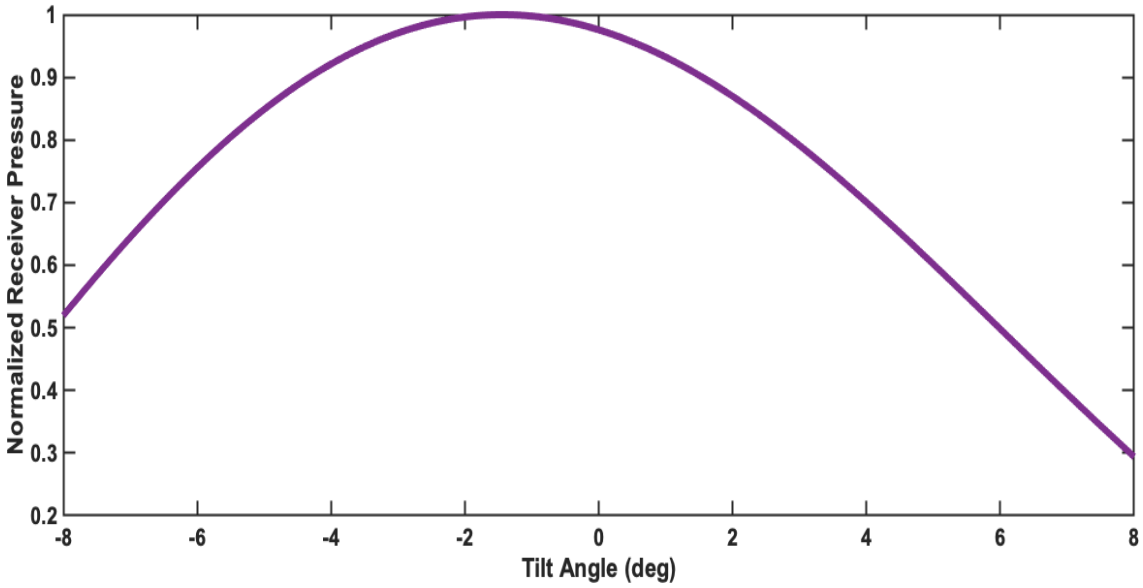

Figure 4.3.3. Theoretical result of tilt angle versus RX PMUT pressure.

As shown in figure 4.3.3, the receiving PMUT pressure reaches its maximum value at around -2 degrees tilting angle which is as expected if we consider the change of reflector height which would affect the ultrasound path length and the arrangement of TX and RX element. A different arrangement of TX and RX arrays will result in a different trend and we can adjust the arrangements accordingly based on our need of tilt angle detection for different applications.

4.4 Experimental Results

Figure 4.4.1 shows the experimental setup for tilt sensing application.
In figure 4.4.1, the figure shows the optical image of the chip under test with a reflector 5 cm away from the transducer plane and an inclinometer on top of the reflector recording the tilt angle. The bottom figure is the zoomed in image of PMUT under test with the TX and RX elements labeled. Using the pinned PMUT arrays, we are increasing the active piezoelectric material being utilized for both TX and RX elements and thereby we see an improvement in both the TX and RX responses and thus a higher SNR compared to those from a traditional PMUT layout.

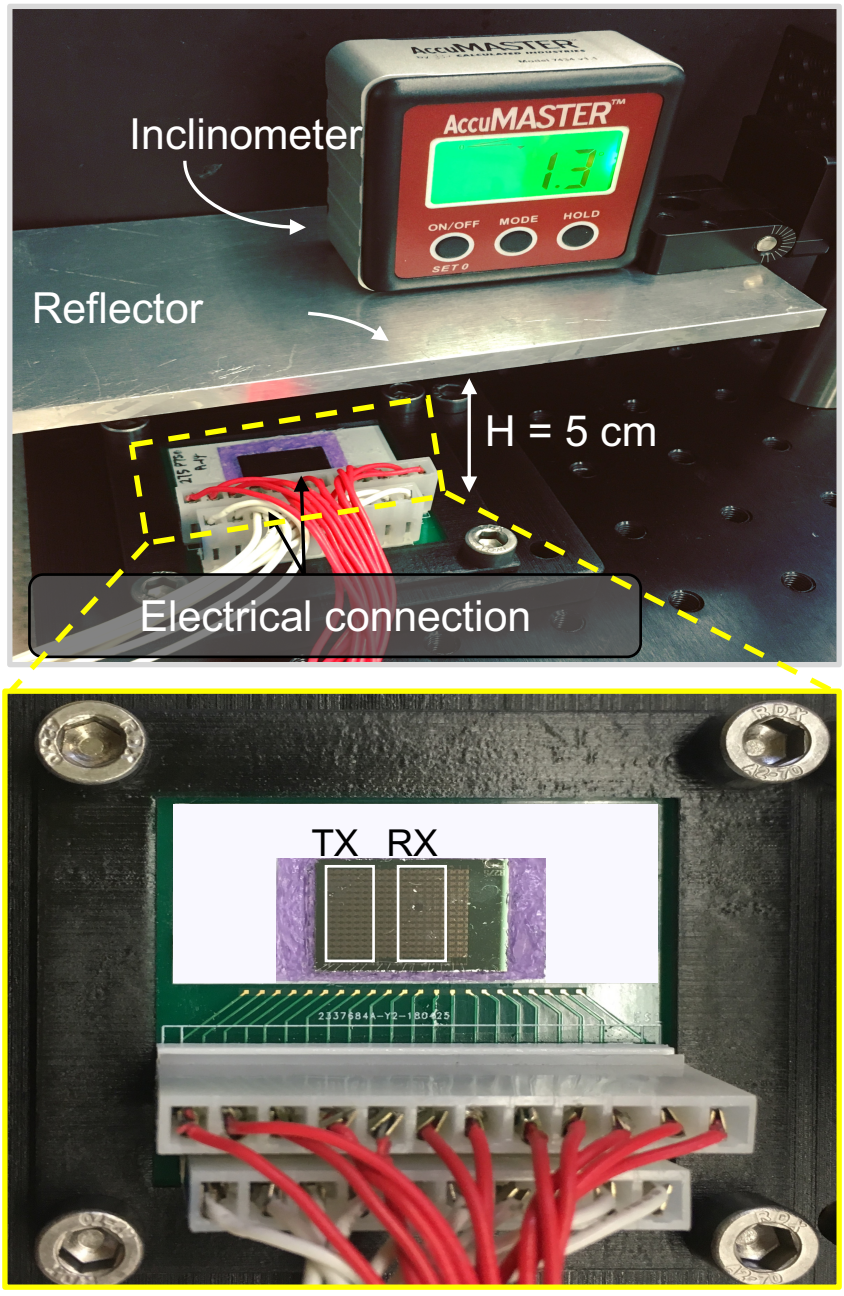

Figure 4.4.1. Experimental setup of the PMUT tilt sensor.

We trigger the TX elements using a function generator at its resonant frequency of 340 kHz with 12 Vpp amplitude and 50 cycles. We then amplify the signal with an off-the-shelf op-amp that requires only $\pm 5V$ power supply rails and we

collect the amplified signal using a function generator along with the trigger signal. We record the real-time tilt angle using the inclinometer from Calculated Industries 7434 AccuMASTER. The chip arrangements are the same as listed in table 4.3.1.

Figure 4.4.2 shows the collected signal from the oscilloscope along with data processing steps. All the signals are post processed with a Butterworth bandpass filter in MATLAB R2019b (The MathWorks Inc., Natick, MA, USA). Figure 4.4.2 (a) shows the captured receiving echo with a strong main echo and a second echo after post processing. Figure 4.4.2 (b) shows the captured unwanted signal when no reflector is present. We subtract the captured echoes with this unwanted signal to get our calibrated signal as shown in figure 4.4.2 (c).

The maximum receiving voltage or in other words, the peak of the main receiving echo as shown in figure 4.4.2(c) is recorded at each tilt angle. The corresponding results are shown in figure 4.4.3.

The pulse-echo experiment is performed repeatedly at each tilt angle varying from -8 degrees to +8 degrees with 1 degree increment each time. The same data processing procedure is followed as described previously and shown in figure 4.4.2.

In figure 4.4.3, the yellow triangular points are experimental results at sixteen tilt angles after post processing, the blue curve is the theoretical result using the same chip arrangement with parameters listed in table 4.3.1.

As seen in figure 4.4.2 (b), the early on unwanted signals due to electrical and mechanical cross talk die out after 150 us. With a speed of sound at 343 m/s, this corresponds to a path length of 5 cm round trip. As a result, we placed our reflector at 5cm away from the chip surface which is far enough to avoid these near-field effects. In order to mitigate these effects for future work, a customized ASIC chip can be utilized. We can also work on isolating the ground electrode plane for each array which in the current layout is being shared among all arrays to further reduce electrical crosstalk.

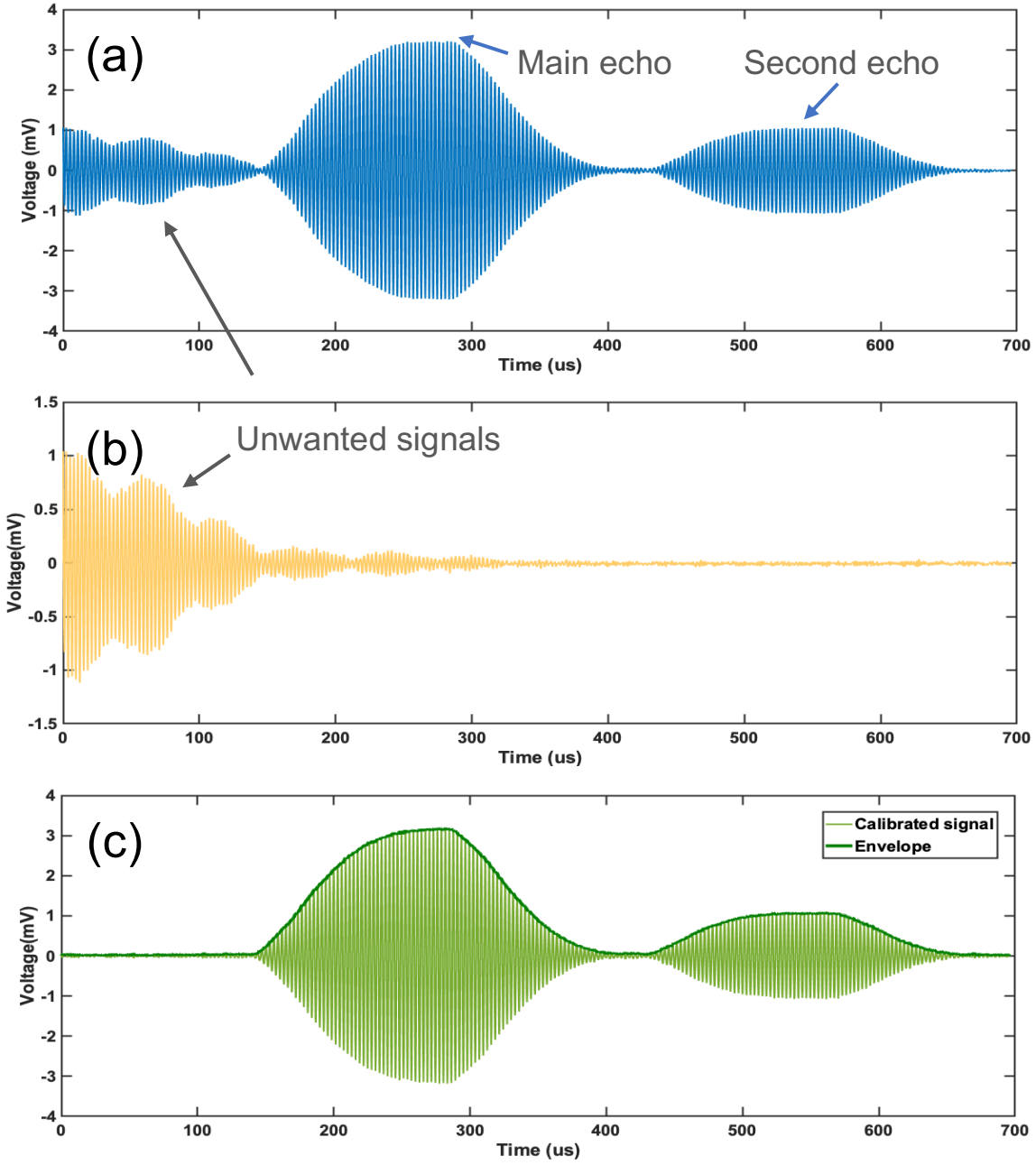

Figure 4.4.2. Sample pulse-echo experiment sensor readout and calibration. (a) Captured receiving echo showing the main echo and the second echo. (b) Captured sensor response with no reflector showing unwanted signals. (c) Calibrated receiving echo where the initial receiving echo is subtracted by the no reflector response. The envelope of the echo is then taken, and the maximum receiving voltage is recorded at each tilt angle.

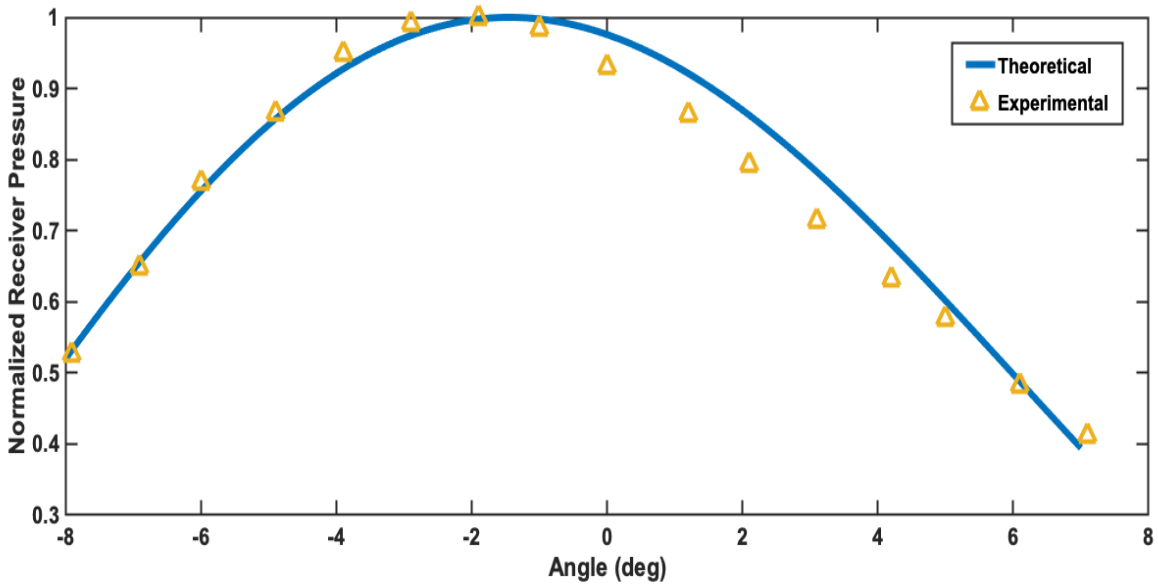

Figure 4.4.3. Recorded sensor output at 16 different tilt angles showing high agreement with the theoretical values with an accuracy of ± 0.7. The maximum sensor output response happens at -2 degree as expected due to the change of reflector height and the placement of the RX element.

Overall, experimental results and theoretical results show high agreement with an accuracy of $\pm 0.7°$. The maximum sensor output response happens at $-2°$ as expected due to the change of reflector height and the placement of the RX element. Most inaccuracies lie between $-2°$ to $+4°$ which could possibly be caused by the minimal change in acoustic path length

This high agreement between experiment and theory along with the new method of determining the tilt angle could open up new application space of MUT-based tilt sensor.

4.5 Conclusion

In this chapter, we report the first ultrasonic tilt sensor that utilizes a single chip pinned PMUT structure. We first performed theoretical work to predict the behavior of a PMUT based tilt sensor. We then fabricated these PMUT arrays accordingly. After that, we carried out experiments with post data processing with results showing high agreement with our theoretical model.

Three distinctive advancements have been achieved: (1) first demonstration of tilt angle sensing by PMUTs; (2) the usage of pulse-echo sensing for the tilt angle measurement by using the receiving (RX) PMUT element's pressure amplitude; and (3) measured results showing matching sensor outputs compared to the predicted value from theory with ± 0.7 accuracy to measure tilt angle up to ± 8 degrees. As such, this work opens new application areas for MUT-based sensors.

Chapter 5

Wireless Power Transfer using PMUT

5.1 Introduction

With the advancement of consumer electronics and the need in medical applications, wireless power transfer (WPT) has become a trending research topic in recent years [77-84]. In consumer electronics, people utilize WPT to charge electronic devices to eliminate the need of wires while maintaining fast charging speed to provide users with convenience and efficiency [77-84]. In medical applications, people mainly make use of WPT to charge implanted devices inside human body to elongate the lifetime of such devices and to reduce their sizes [85-88].

There are two categories within wireless power transfer, near-field wireless power transfer and far-field wireless power transfer. In this chapter, we focus on the near-field power transfer. There are several methods to realize wireless power transfer. The majority of current technologies uses inductive charging with magnetic fields to realize WPT especially in consumer electronics. Others use capacitive coupling for WPT.

Although inductive charging provides sufficient efficiency and good coverage, it cannot be used simultaneously with the presence of other metal parts since the existence of certain metals will block the magnetic field pathway and prevents wireless power transfer. In addition, inductive charging emits EMF radiation which is harmful to human body.

As for medical applications, researchers have shown promising results of using ultrasonic transmission to power brain-implants which provides sufficient power transfer while emitting ultrasound intensity within the safety limit [89]. In these studies, researchers use bulk piezo materials as transmitting device and a PMUT device as the receiving PMUT or a receiving node in liquid-coupled mode.

Among all previous studies, no one has yet studied the possibility of using a MEMS-based ultrasonic transducer as a complete wireless power transfer system for air-coupled applications, meaning using such devices as a transmitter and a receiver all at once. MEMS-based WPT system has advantages of consuming low power and small in size. The drawback of using a MEMS-based transmitter is its limited emission power. A complete MEMS-based WPT system may also suffer from low power transfer efficiency due to the relatively lower electromechanical coupling between PMUT device.

However, with the design of our pinned PMUT device that is shown to provide improved acoustic performance, i.e., increased output pressure at resonance and improved electromechanical coupling, it is possible to make use of such structures as a wireless power transmitter and receiver using with careful design. As a result, we explore the possibilities of using such structures to enable wireless power transfer for air-coupled applications meaning in low frequency spectrum.

5.2 Concept

To realize wireless power transfer using PMUTs, we need a transmitter that can transmit as much power as possible yet a receiving PMUT that is able to receive most of the transmitted power at a given distance. In order to transmit enough acoustic power, we need to utilize a PMUT array while lowering transmitter frequency since output power increases with decreased frequency in air [1-3]. As a result, we designed a circular array instead of rectangular arrays to focus the transmitted acoustic beam at a given location, and we designed a circular standalone PMUT as the receiving element.

However, using circular PMUTs in a circular array arrangement will lead to a waste of space due to limitations of DRIE which lead to the minimum spacing requirement between each standalone PMUT. In addition, such arrangement by nature occupies less space compared to a ring arrangement as shown in figure 5.2.1. As a result, we would like to design our array using ring PMUT instead of circular PMUT.

Figure 5.2.1 shows the schematics of the conceptual transmitter and receiver arrangement where figure 5.2.1 (a) shows the transmitter arrangement using circle PMUTs and figure 5.2.1 (b) shows the transmitter arrangement using ring PMUTs. We can see from the comparison that circular PMUTs will lead to more white space [36]. Figure 5.2.1 (c) shows the arrangement of the complete WPT system. Each colored array is electrically excited together and each array will be phase shifted to concentrate all the acoustic power to the receiving PMUT node.

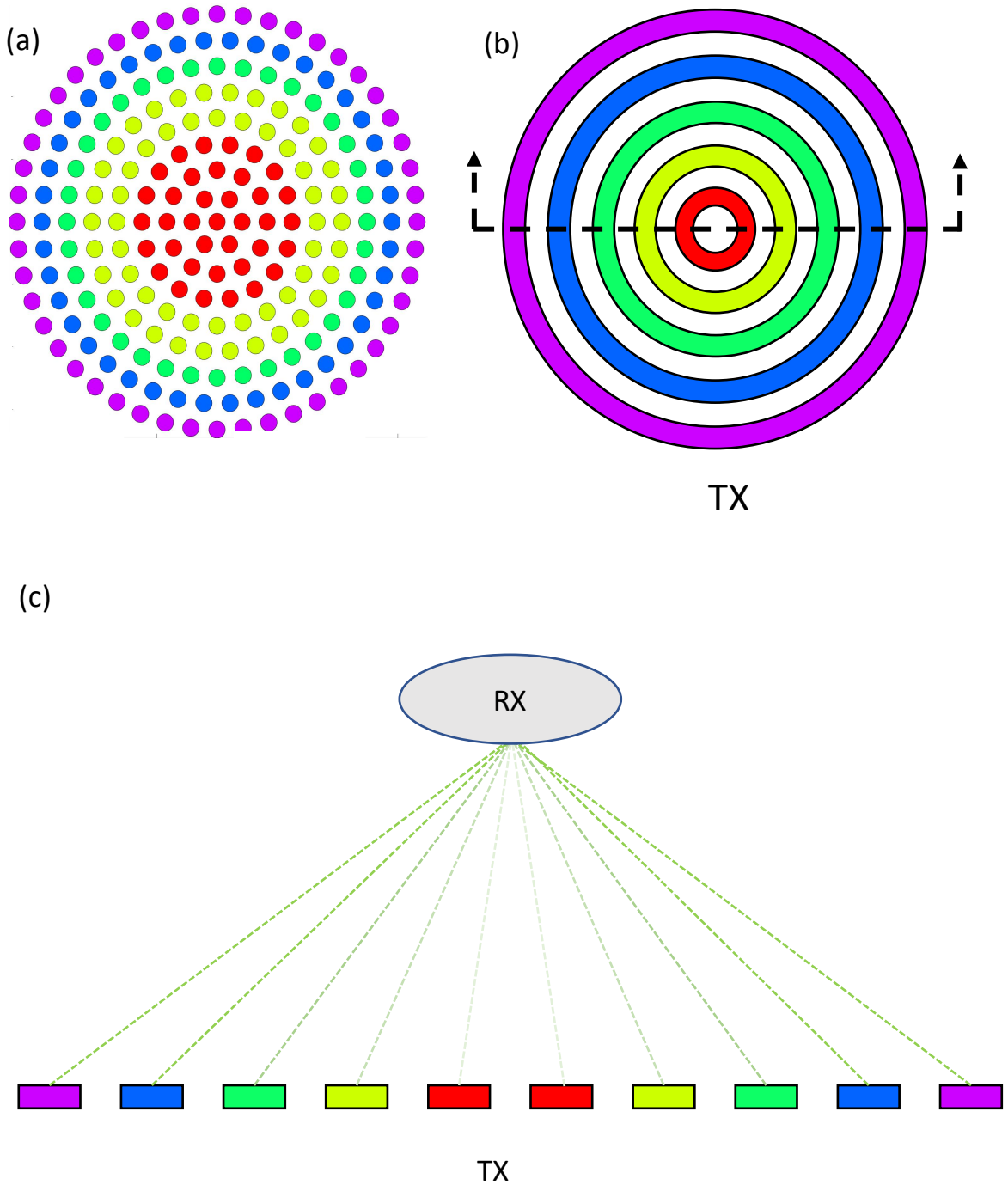

Figure 5.2.1. Schematics of wireless power transfer concept. (a) Annular circle PMUT array as a transmitter. (b). Annular ring PMUT array as a transmitter. (c) Transmitter and receiver arrangement.

5.2.1 Pinned Ring PMUT Design Concept

In order to make use of the annular ring array structure, we need a ring PMUT with high performance in air. Since we've thoroughly studied the pinned PMUT structure, we would like to explore the possibility of implementing such structure on a ring PMUT and its performance.

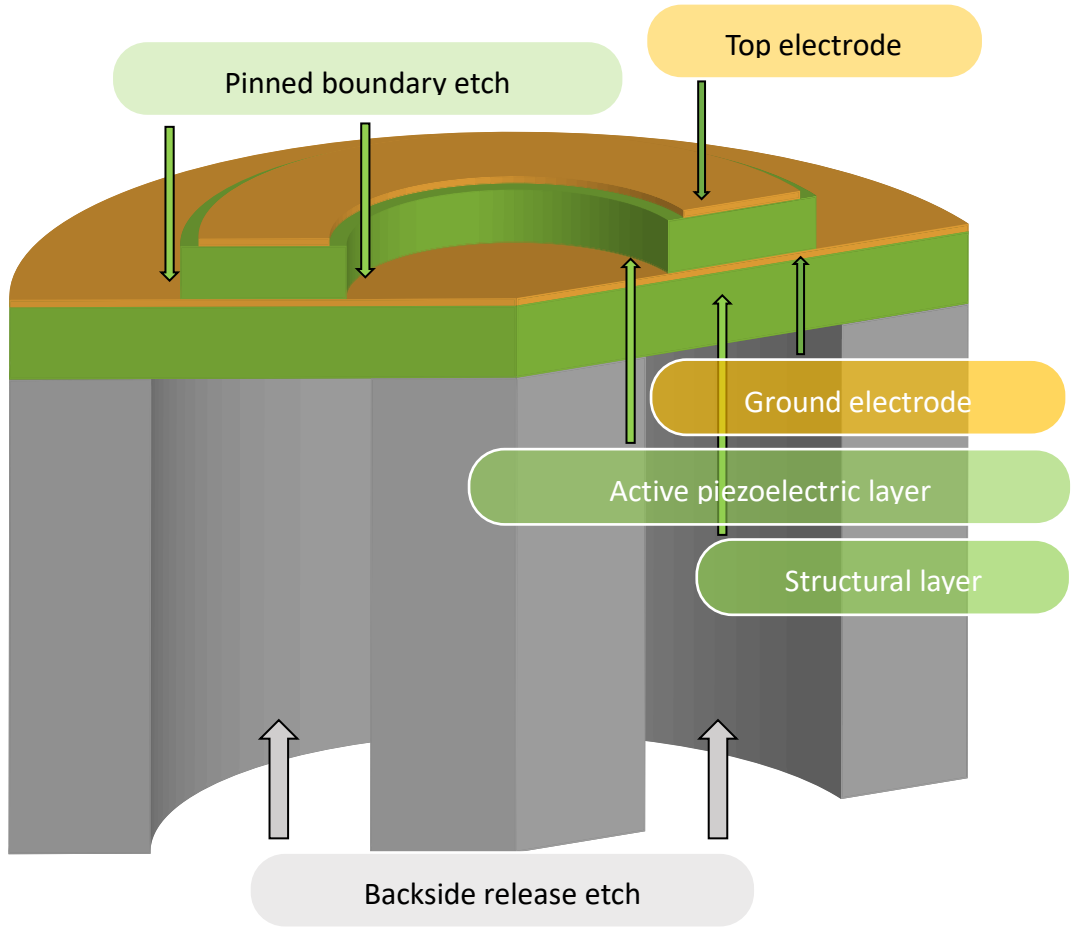

Figure 5.2.2. Schematics of pinned ring PMUT.

Figure 5.2.2 shows the 3D schematics of the pinned ring PMUT design where the green color represents the piezoelectric layer, the orange color represents the electrode layer and the grey color represents the backside DRIE to free the membrane. Similar to the pinned circular PMUT design, we have the structural layer to support the active piezoelectric layer. We also etch the edge of the active piezoelectric layer to realize the pinned boundary. The ring design is realized through backside release etch around a center post.

5.2.2 Wireless Power Transfer Design Concept

With the design of pinned ring PMUT, we can arrange pinned ring PMUTs into array as a transmitter. Each array will contain several ring PMUTs and the array will be activated with a phase shift to concentrate as much acoustic power to the desired receiving location as possible. We use a standalone pinned circular PMUT as the receiving node.

We also try to keep our operating frequency as low as possible to transmit large enough power in air since ultrasound intensity attenuates drastically in air with increasing frequency. The limiting factor here is that with lower operating frequency, the PMUT radius will become larger. Larger PMUT will tend to break due to stress distribution from fabrication. Thus, we need to design our PMUTs accordingly to meet both the desired operating frequency and fabrication limitation.

5.3 Simulation Setup of Pinned Ring PMUT

The simulation setup of the pinned ring PMUT is realized in COMSOL Multiphysics v4.3. Similar to previous setups, we utilize the axisymmetric acoustic-structure-piezoelectric module where the device structure is designed in the solid domain with the structural layer fixed at the boundary and the active layer free to move to imitate the pinned boundary condition as shown in figure 5.3.1. The pinned boundary is realized by etch away the edge of the active layer as shown in figure 5.2.2.

The structure is excited in the electrical domain where the bottom electrode is grounded, and the top electrode is excited to 1 volt as shown in figure 5.3.1. Again, the acoustics domain contains the regular acoustic domain and the perfectly matched layer to simulate infinite space.

We designed the device to have a resonant frequency of 160 kHz and we are comparing its performance with a clamped ring PMUT at the same resonant frequency. The details of parameter selection and simulation results are covered in the following section.

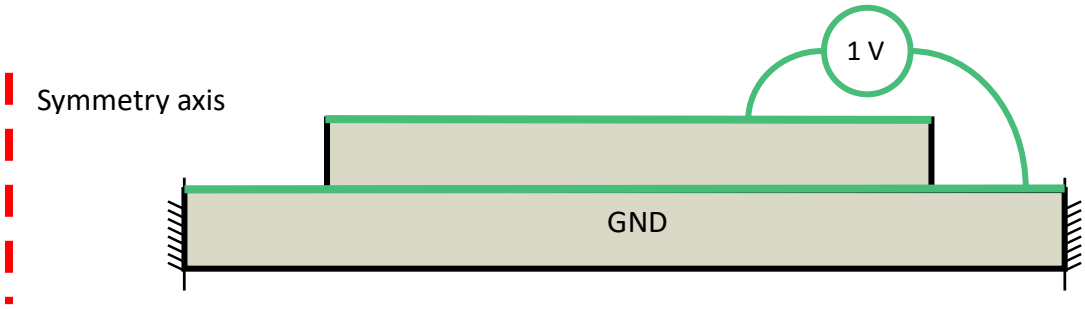

Figure 5.3.1. Schematics of simulation setup and boundary condition of the pinned ring PMUT.

5.4 Simulation Results of Pinned Ring PMUT

The simulated mode shape of the pinned ring PMUT along with the clamped PMUT is shown in figure 5.4.1 where the orange curve represents the pinned ring PMUT and the blue curve represent the clamped ring PMUT.
We can see from the mode shape result that the pinned ring PMUT follows a different mode shape than the clamped ring PMUT as expected for a pinned PMUT design. For a clamped ring design, the inflection point takes place at 23% of radius where for a pinned ring design, the inflection point takes place at 16% of radius.
Figure 5.4.2 shows the simulated frequency response of the pinned ring PMUT and the clamped ring PMUT at the same resonant frequency.
In figure 5.4.2, the top figure compares the result of center displacement per volt of a pinned ring PMUT and a clamped ring PMUT where the bottom figure compared the results of pressure output at 3 mm distance from the transducer plane of a pinned ring PMUT and a clamped ring PMUT. The results of pinned ring PMUT is shown in orange curves and the results of clamped ring PMUT is shown in blue curves.

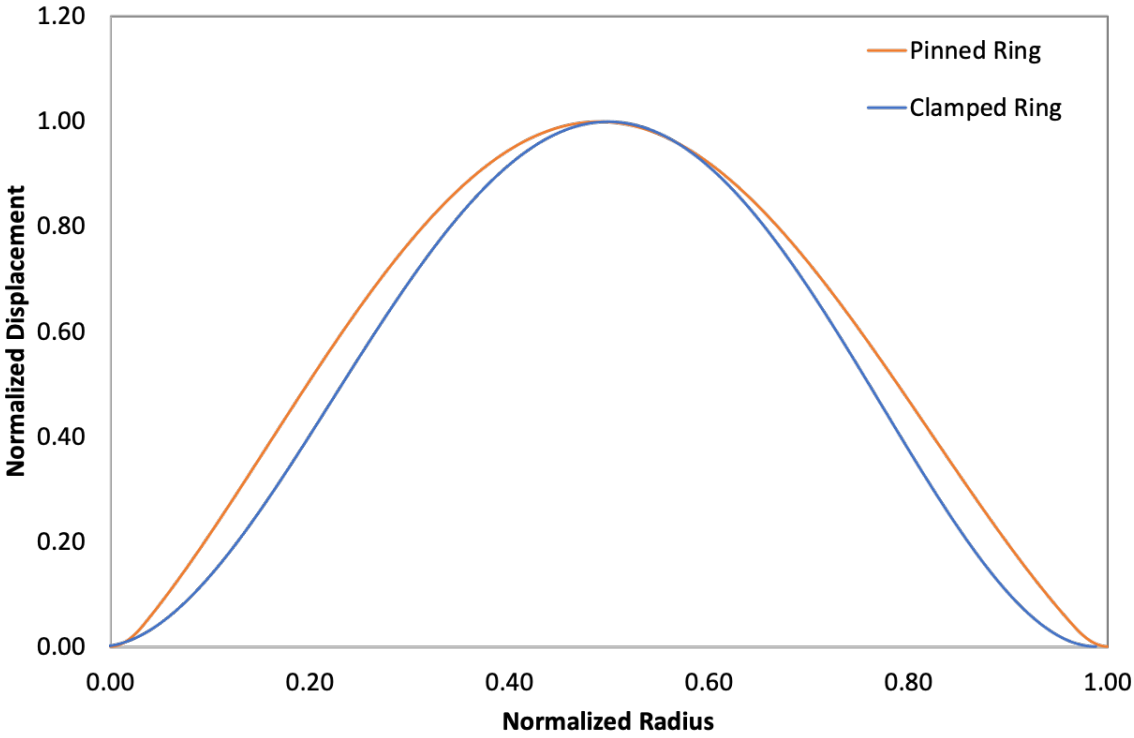

Figure 5.4.1. Simulated mode shape of pinned ring PMUT and clamped ring PMUT.

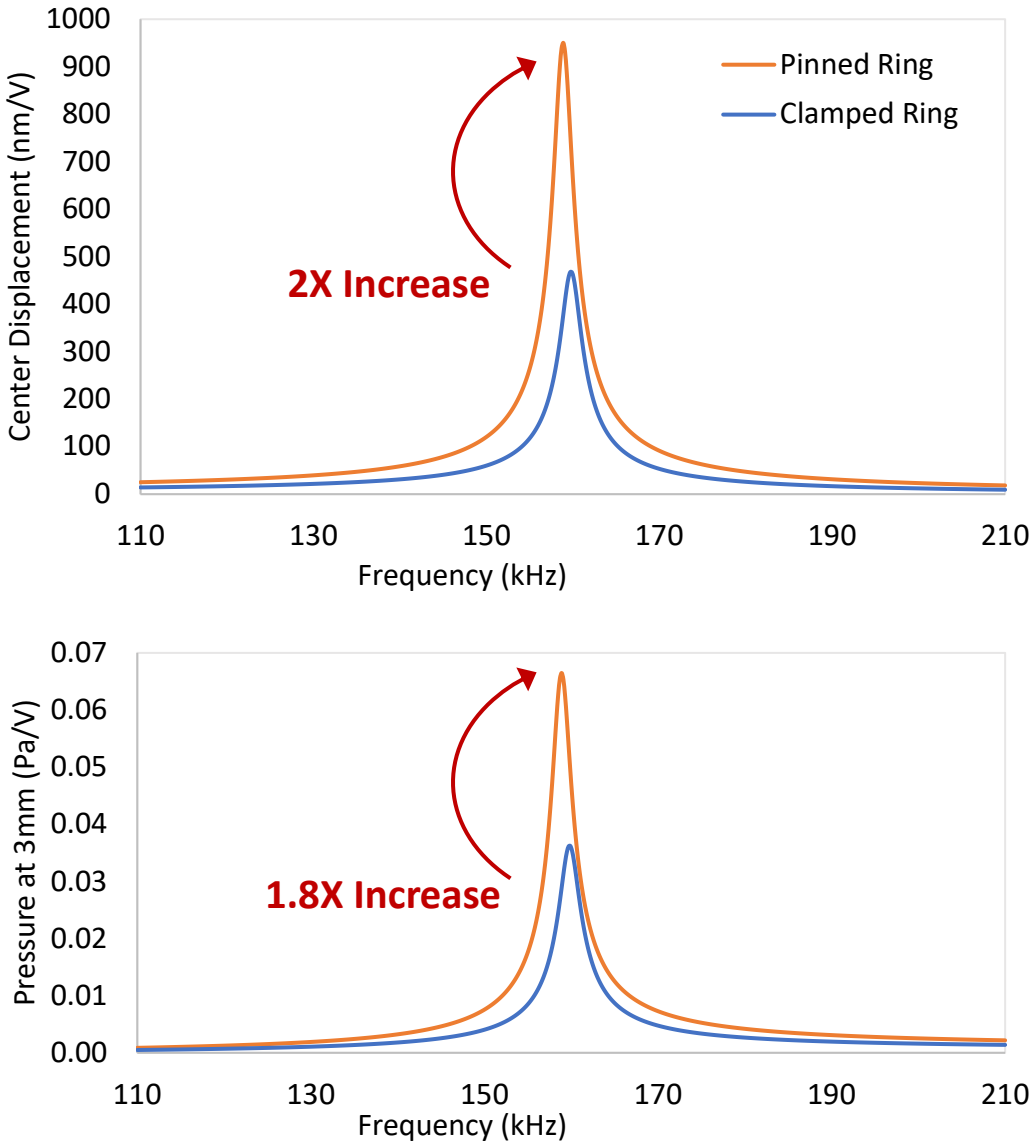

Figure 5.4.2. Simulated frequency response of pinned ring PMUT and clamped ring PMUT.

The design parameters of the pinned ring PMUT has been studied parametrically to obtain the best performance meaning the highest center displacement with varying the ratio of ring etch length l_e to ring radius r as labeled in figure 5.4.3.

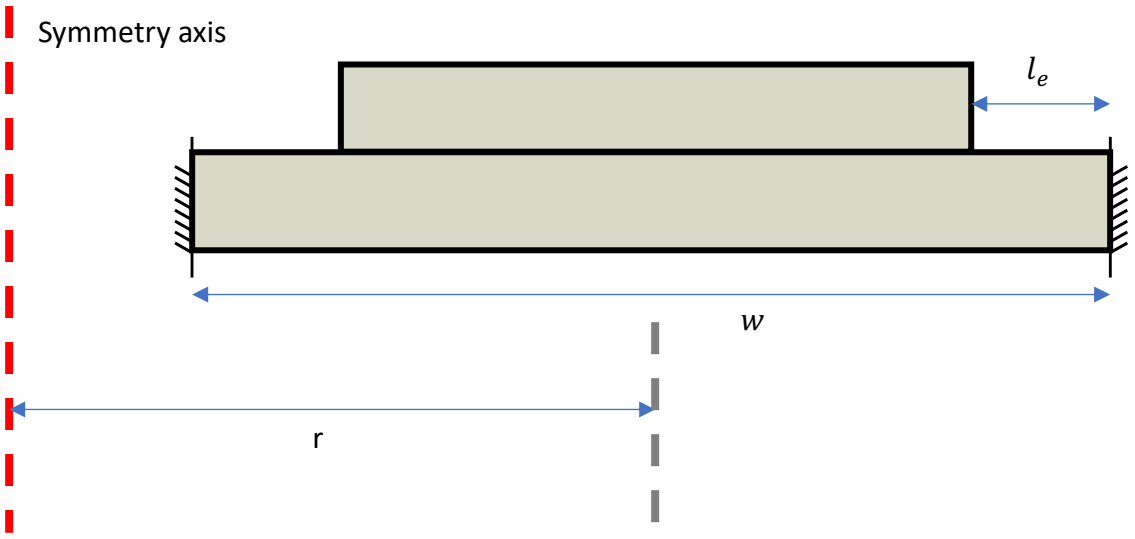

Figure 5.4.3. Schematics of pinned PMUT parameter definition.

Similar to pinned circular PMUT, we found that the best performance happens with 20% of etch length.

In figure 5.4.2, the pinned ring PMUT gives a peak center displacement of 932 nm/V where the clamped ring PMUT gives a peak center displacement of 456 nm/V at the same resonant frequency. This shows a two times increasement in center displacement resulting from the pinned design.

In addition, the pinned ring PMUT shows a peak pressure of 0.065 Pa/V where the clamped ring PMUT shows a peak pressure of 0.036 Pa/V at the same resonant frequency at a distance of 3 mm away from the transducer plane. This is 1.8 times improvement in pressure output resulting from the pinned design.

With simulation validation, the pinned PMUT design shows promising results with improved center displacement amplitude and pressure output compared to a traditional clamped design. We utilize this benefit to realize our wireless power transfer transmitting array. Details of design parameters and simulation results will be covered in the following sections.

5.5 Simulation Setup of Wireless Power Transfer

With confirmed improvement in power output from pinned ring PMUT design, we utilize its ring structure to realize the transmitting side of wireless power transfer. The advantages of using an annular ring design is not only its increased fill factor but also its characteristics of maintaining same resonant frequency while changing the radius of the device as long as the width is fixed [90-91].

There are several factors that we need to consider when designing the transmitting array. First thing to consider is the operating frequency. As mentioned earlier, we desire lower operating frequency since the lower the frequency, the higher the emitted acoustic power from the array. However, lower frequency will require larger width of the ring PMUT which can be a problem due to fabrication limitations. As a result, we are choosing an operating frequency which is low enough yet providing a reasonable device size.

Second thing to consider is number of arrays to operate. One parameter that researchers use to evaluate the efficiency of the entire wireless power transfer system is the acoustic transfer fraction (ATF) which is defined in the following equation [89, 92-96].

$$ATF = \frac{Acoustic\ power\ at\ RX}{Acoustic\ power\ at\ TX} \tag{5.5.1}$$

Studies have shown that ATF saturates when number of array element is larger than nine [89]. Ideally, we want to design a system with 9 arrays. However, for in lab testing, our function generator can only perform phase delay on four channels. As a result, we designed our transmitting array to have four channels to operate.

Third thing to consider is the number of pinned ring PMUTs in each array. Since we don't have a customized ASIC chip, we want each array to have similar area such that the capacitance of each array is similar. So, we need to design carefully to provide similar array area which is a combination of pitch between each single ring PMUT and number of elements per array.

Next thing to consider is the pitch distance between each element. From literature, it is well understood that the spacing between each array need to be smaller compared to the wavelength of the device in order to compress grating lobes [1-3,89]. The existence of grating lobes means that acoustic power emitted from the transmitting array is not concentrated which will lead to a loss in ATF. As a result, we need to design the spacing accordingly to suppress grating lobes.

We then need to consider the location and sizing of the receiving PMUT. Ideally, we would like to place the receiving PMUT at the natural focus of the

transmitting array which is the near-field length L of the transmitted ultrasound defined in the following equation [1-3].

$$L = \frac{(2a)^2 - \lambda^2}{4\lambda} \approx \frac{a^2}{\lambda}, for\ (2a)^2 \geq \lambda^2 \quad (5.5.2)$$

Where a is the dimension of the device which in our case is the width of the ring PMUT and λ is the wavelength of the emitted ultrasound. The size of the receiving PMUT is then determined based on the spot size of the focused ultrasound beam.
Last thing to consider is the phase delay from the transmitting PMUT. In general, phase delay is applied based on the distance between each array to the focus point. The definition of phase delay $\emptyset$ is described in the following equation.

$$\emptyset = \frac{2\pi d}{c/f} \quad (5.5.3)$$

Where d is the distance between the array and the focus point, c is the speed of sound in the medium and f is the operating frequency.
The schematics of the simulation setup is shown in figure 5.5.1. All the important design parameters are labeled, and the details of the parameter selection will be covered in the next section.

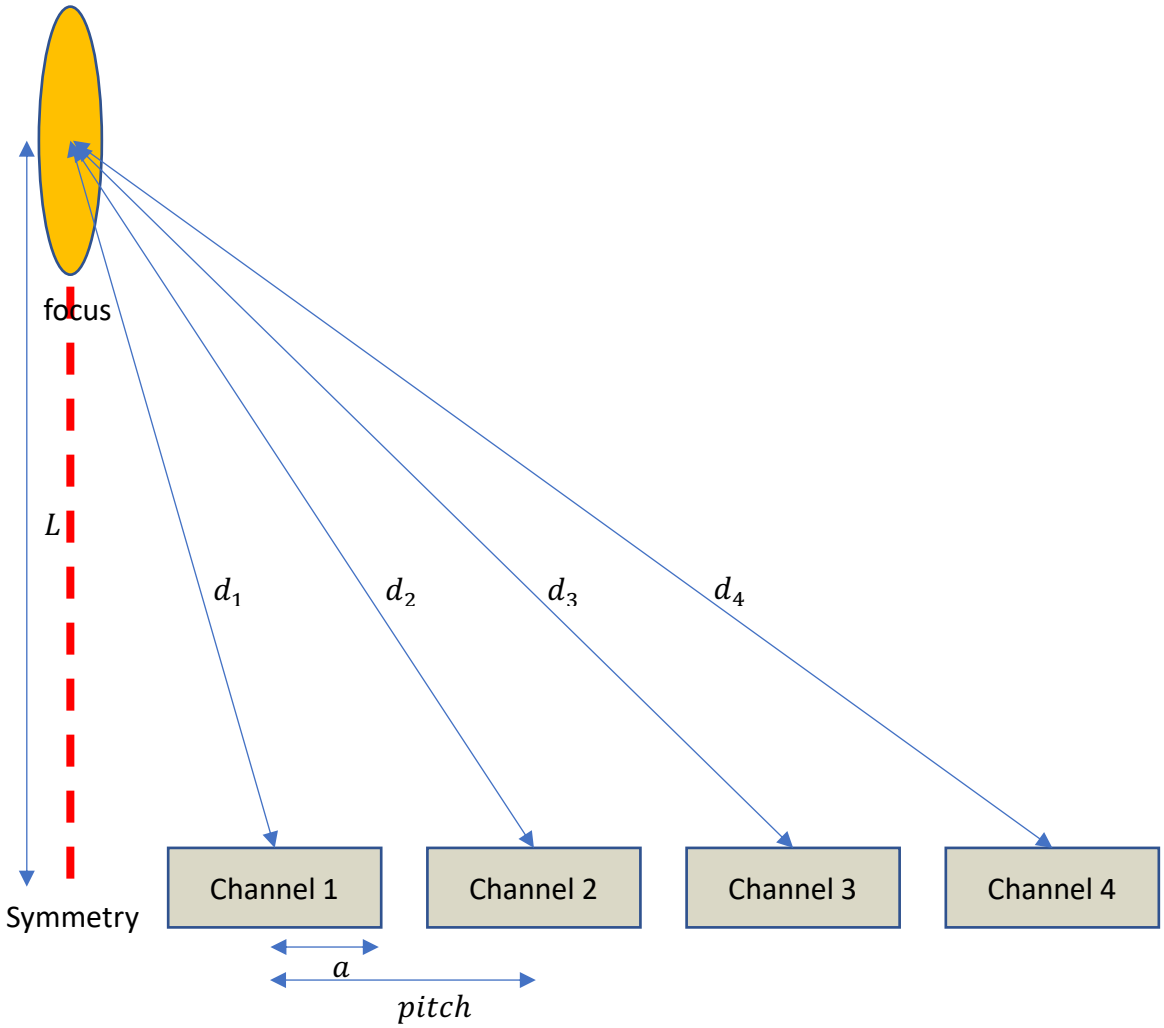

Figure 5.5.1. Schematics of WPT simulation setup with parameters labeled.

5.6 Simulation Results of Wireless Power Transfer

The detailed parameters that we use for simulation setup is listed in table 5.6.1.

Table 5.6.1. List of parameters for simulation setup

Parameter	Value
Ring PMUT width w	$250\ \mu m$
Radius r of the innermost PMUT	$300\ \mu m$
Pitch	$400\ \mu m$
Speed of sound c	$340\ m/s$
Resonant frequency	$250\ kHz$

We chose a resonant frequency of 250 kHz to satisfy our conditions as explained in the previous section. This resonant frequency requires a width of 250 um for the ring PMUT, which is within the fabrication limitation. In addition, the resulting wavelength is $\lambda = c/f = 1.36$ mm which is way larger than the spacing between each array.

We designed our transmitting array to have a total of 9 ring PMUTs. The first channel has 3 ring PMUTs, the second channel has 2 ring PMUTs, and the third and last channel each has 1 ring PMUT.

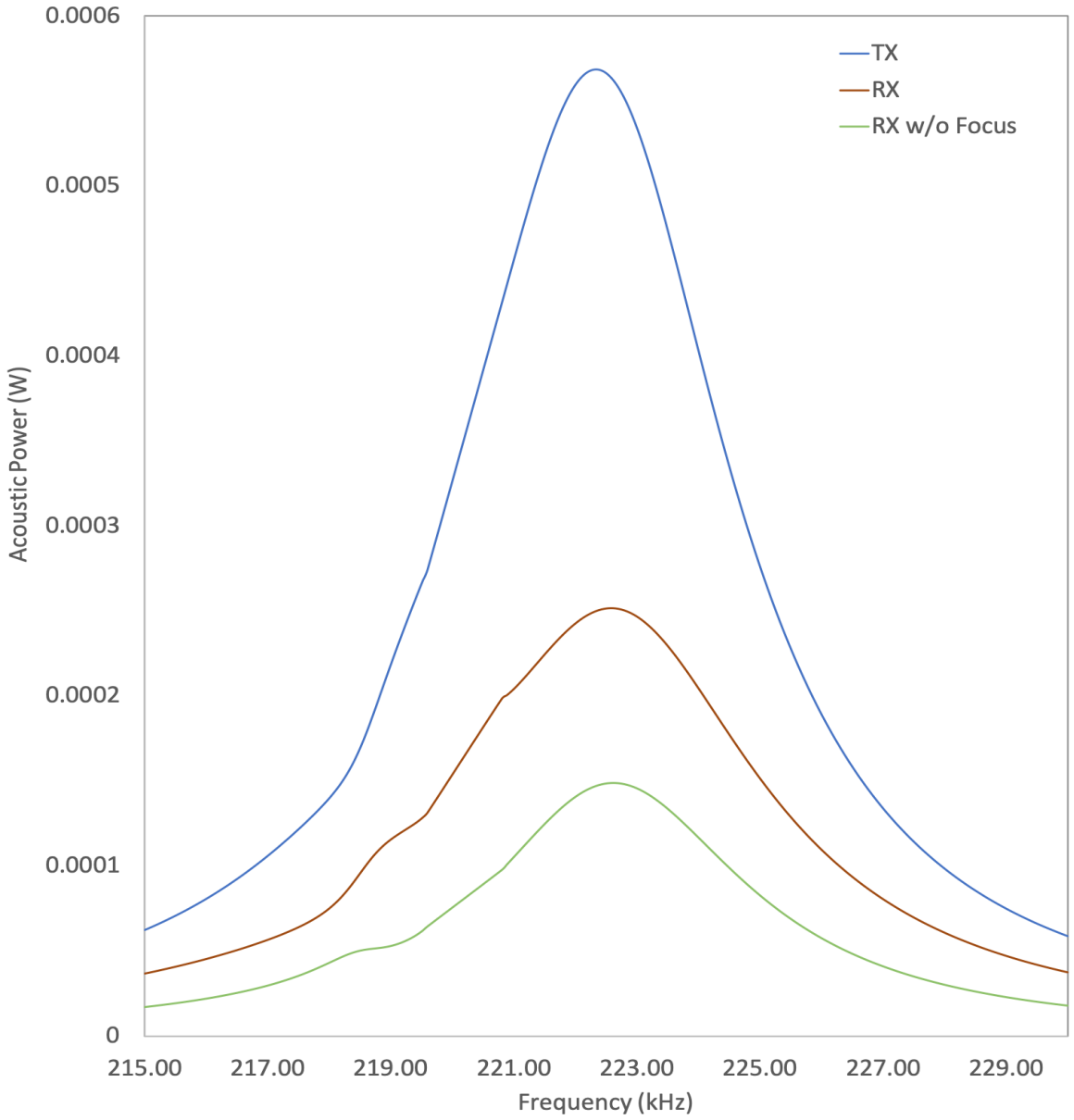

Figure 5.6.1. Simulated acoustic power from transmitting array and receiving array with focus and without focus.

Figure 5.6.1 shows the simulation result of acoustic power Q over frequency from a wireless power transfer system providing the largest acoustic intensity from the receiving array with focusing [1-3].

$$Q = \int_{Area} I \tag{5.6.1}$$

$$I = pu \tag{5.6.2}$$

Where I is the acoustic intensity, P is the acoustic pressure and u is particle velocity. We defined a box area of 0.1 mm by 3mm where 3 mm is along the width of the transmitting array as described in figure 5.6.2.

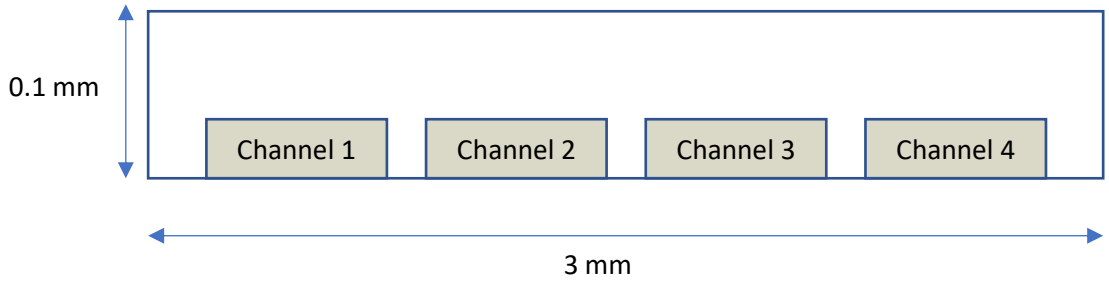

Figure 5.6.2. Schematics of box area for acoustic power simulation result.

In figure 5.6.1, blue curve shows the simulated acoustic power of transmitting array, red curve shows the simulated acoustic power of receiving array with focusing and the green curve shows the simulated acoustic power of receiving array without focusing both at 1.8 mm distance from the transmitting array.
The peak emitted acoustic power from the transmitting array happens at 222 kHz with a value of 0.57 W at 1 volt excitation. The peak receiving acoustic power with focusing happens at 222 kHz with a value of 0.25 W at 1 volt excitation. And the peak receiving acoustic power without focusing happens at 222 kHz with a value of 0.15 W at 1 volt excitation.
The generated acoustic intensity profile of the receiving PMUT with and without focusing is shown in figure 5.6.3.

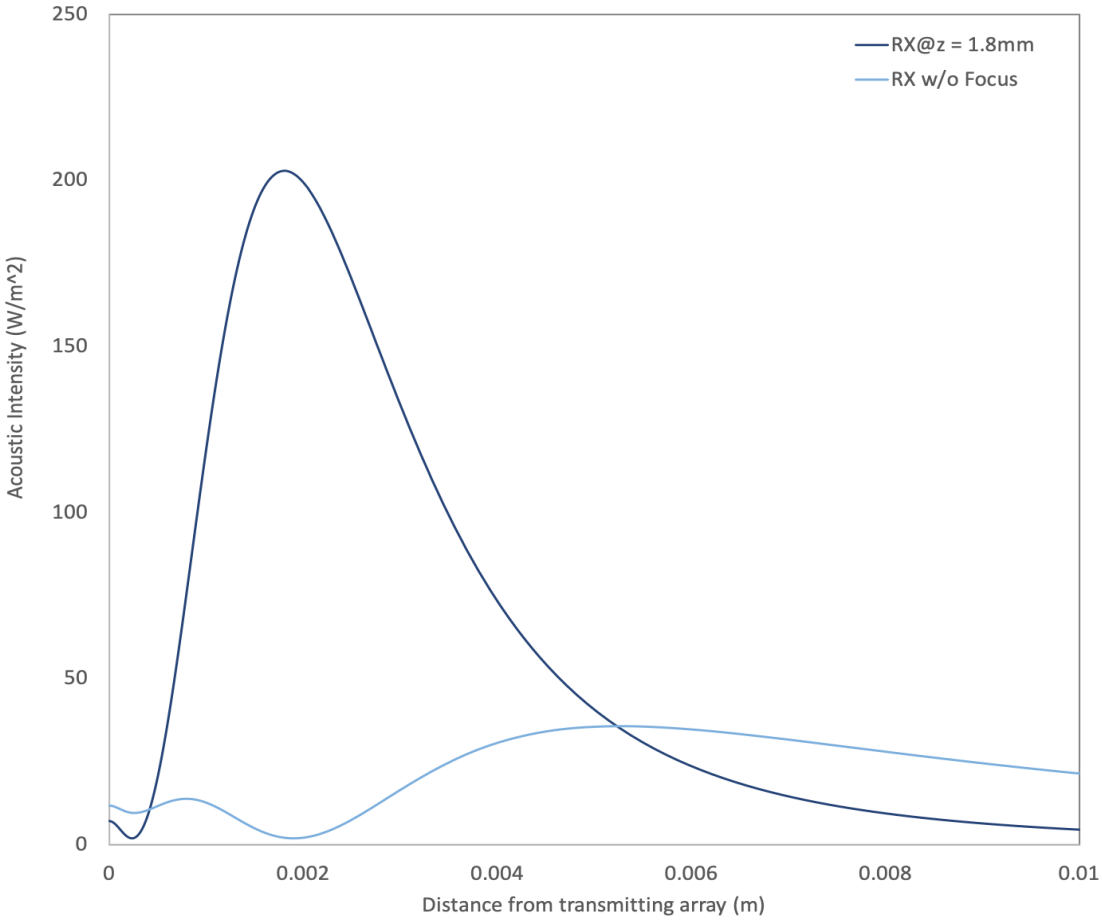

Figure 5.6.3. Simulated acoustic intensity profile of the receiving array with focus at 1.8 mm distance from the transmitting array and without focus.

From figure 5.6.2, we can see that without focus, the maximum acoustic intensity happens at 5 mm distance with a value of 37 W/m^2. The maximum acoustic intensity with focus happens at 1.8 mm distance with a value of 203 W/m^2. This is 5.5 times improvement in acoustic intensity using phase shift.

The generated acoustic intensity is within the safety limit according to the American Council of Governmental and Industrial Hygienists (ACGIH) – recommended pressure limit which corresponds to an intensity of 306 W/m^2 [93] yet large enough to ensure high efficiency of the entire wireless power transfer system.

The acoustic transfer fraction (ATF) at different focus point is calculated using equation 5.5.1 and the results are shown in figure 5.6.3. From the figure, we can see that the maximum attainable ATF happens at a focus point of 2.7 mm away from the transmitting array which provides a 57% efficiency. This value is the

highest achievable ATF that we've seen from the literature based on a MEMS acoustic device. It also shows that the wireless power transfer system has a working range of 2 mm to 4 mm if we want to keep an efficiency of 40%. The ability to provide sufficient efficiency over a working range provides convenience for a consumer electronic device.
Note that this design only utilize four channels and we can achieve even higher efficiency if we can increase the number of channels for phase focusing.

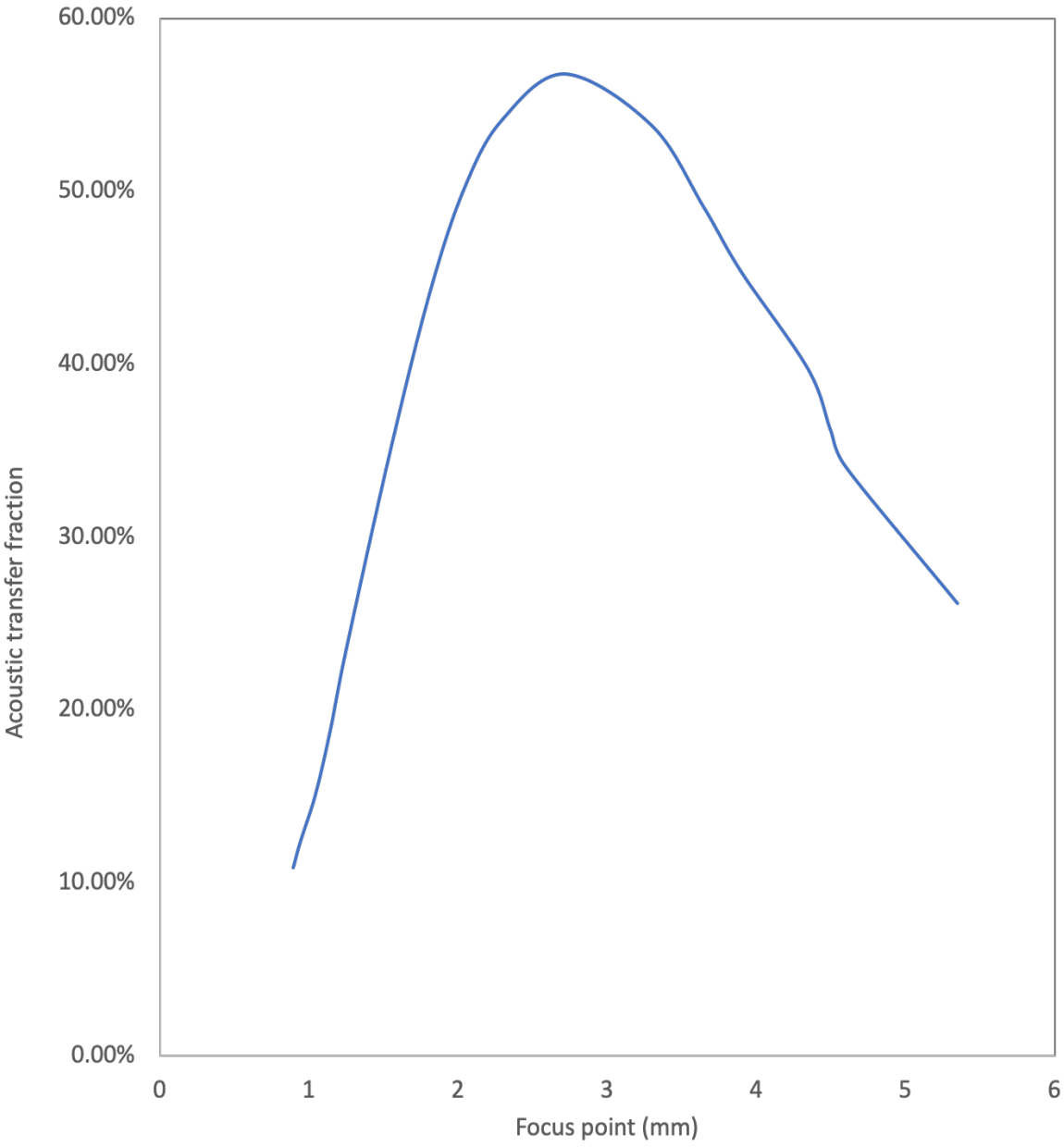

Figure 5.6.4. Simulated acoustic transfer fraction over focus point at resonant frequency.

5.7 Conclusion

This chapter reports the design concept and simulation result of a wireless power transfer system based on a MEMS-acoustic device. We first investigated a new ring PMUT structure based on the pinned design. Simulation results show an improvement of 2.2 times in center displacement amplitude and 1.8 times improvement in pressure output.

Based on the pinned ring PMUT structure, we developed the transmitting array of the wireless power transfer system. We used four channels for phase shifting with a resonant frequency of 250 kHz. Simulation results show an improvement of 5.5 times in acoustic intensity at the receiving node comparing the result with and without focusing.

As a result, we are able to achieve a maximum efficiency of 57% at a focus point of 2.7 mm from the transmitting array. We can also allow a working distance of 2mm to 4mm to maintain an efficiency of 40%.

In conclusion, we've designed and studied a wireless power transfer system using pinned PMUT structure showing 57% efficiency which is the highest efficiency seen from literature based on a MEMS-acoustic device. The achieved efficiency has room for improvement if we allow more channels to operate for phase shift. This study opens up new application space for wireless power transfer using MEMS-acoustic device.

Chapter 6

Long-distance Object Detection using PMUTs

6.1 Introduction

Researchers have explored extensively using Micromachined Ultrasonic Transducers (MUTs) for liquid-coupled applications such as portable medical imaging and cardiovascular imaging [7-12]. However, using MUTs for air-coupled applications have not been explored as much. In particular, piezoelectric Micromachined Ultrasonic Transducer (PMUT) is seen as a better candidate for air-coupled application compared to a Capacitive Micromachined Ultrasonic Transducer (CMUT). For air-coupled application with MUTs operated as a transmitting unit, we desire a device that can provide as large a vibrating amplitude as possible. Larger vibrating amplitude translates to larger emitted acoustic pressure. With high acoustic pressure, the device will be able to send ultrasound to longer distance. This is especially beneficial for applications such as range finding and long-distance object detection.

In general, CMUT has high electromechanical coupling which lead to high receiving sensitivity [23-26]. However, for high transmitting sensitivity, we need the CMUT plate to vibrate with large amplitude. This is in conflict with the existence of the thin gap required for high electromechanical coupling. In addition, large vibrating amplitude might lead to problems such as pull in.

PMUT, on the other hand, do not have a thin gap which limit its vibrating amplitude. This geometry freedom provides PMUT with more application space as a transmitting device for air-coupled application. Large vibrating amplitude or acoustic power means the device should operate at as low frequency as it can afford. Lower frequency is also preferred for air-coupled application since ultrasound attenuates with increasing frequency.

A typical PMUT device with traditional clamped boundary condition has an operating frequency above 500 kHz as seen from literature. This is still a relatively large operating frequency. We would like to explore the possibility of lowering a PMUT device's operating frequency and use it for long-distance object detection.

From our device fabrication experience in the Berkeley Marvell Nanofabrication Lab, the lowest operating frequency we can achieve in air is 630 kHz. Lower frequency means larger device size which can cause problems to the device itself such as broken Aluminum Nitride (AlN) resulting from stress distribution through the fabrication process.

As a result, we would like to explore the possibility of enlarging the PMUT device's size from the fabrication process without device breakage so that we can achieve a much lower operating frequency. The design and simulation result of such device will be realized using COMSOL Multiphysics v4.3. We will then fabricate such devices in the Berkeley Marvell Nanofabrication Lab and perform device characterization. Long-distance detection using such fabricated device will then be studied in a pulse-echo mode.

6.2 Concept

To achieve low resonant frequency, we designed a traditional clamped PMUT at two radii. The larger PMUT has a radius of 355 um and the smaller PMUT has a radius of 275 um. The exact film stack is illustrated in figure 6.2.1.

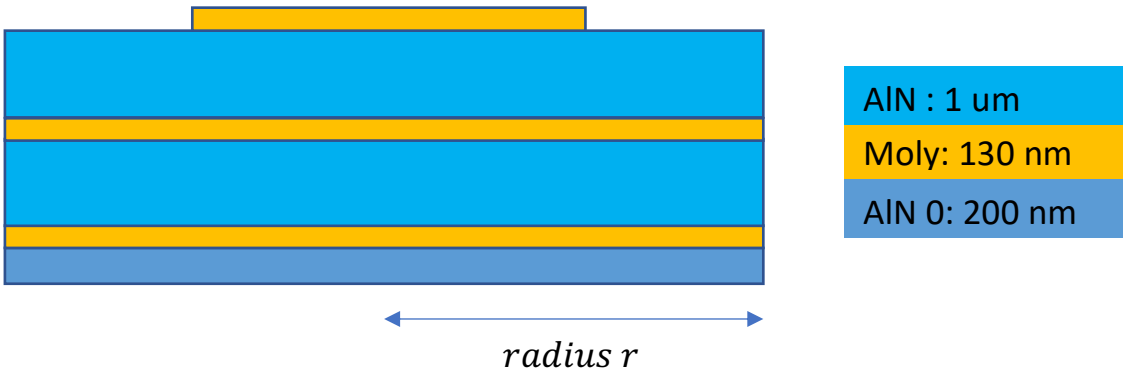

Figure 6.2.1 Illustration of PMUT film stack.

As shown in figure 6.2.1, each standalone PMUT device consists of a seed AlN layer which is 200 nm in thickness, a bottom ground electrode using Molybdenum (Moly) as the electrode material and is 130 nm in thickness, a bottom piezoelectric layer using AlN which is 1 um in thickness, a 130 nm Moly middle electrode layer, another 1 um AlN top piezoelectric layer and a 130 nm Moly top electrode layer. Radius r is defined as the backside DRIE that frees up the membrane. The film stack and fabrication process follow that of a bimorph PMUT device [59]. However, in this study, only the top AlN layer is activated and the device operates in the traditional clamped PMUT mode. Each chip

consists of five arrays and each array has 4 by 20 standalone PMUTs. The PMUT chip layout is shown in figure 6.2.2.

Figure 6.2.2 Array layout of a PMUT chip.

From figure 6.2.2, each colored box represents one PMUT array. Each array is electrically connected together and excited together. All five arrays share the same common ground and the top electrode can be activated separately.

6.3 Experimental Setup and Result

The fabrication process of the chip is similar to that described in chapter 2. After we fabricate the chip, we glue each chip to a customized PCB board. We then solder header pins onto the PCB board for electrical connection. Each chip is then excited in the pulse-echo mode to characterize its behavior.

The larger radius chip is designed to have a resonant frequency of 180 kHz. The frequency spectrum of this chip is shown in figure 6.3.1.
From figure 6.3.1, we see that the chip has a resonant peak at around 180 kHz. However, it also has a lot of unexpected peaks at frequencies below its resonance. We suspect that this is due to broken PMUTs. In addition, when this chip is being excited in pulse-echo mode, we cannot observe a clear echo. When we inspect the chip under a microscope, we also observe broken PMUTs across the chip. We conclude that this radius is too large to survive our fabrication process.

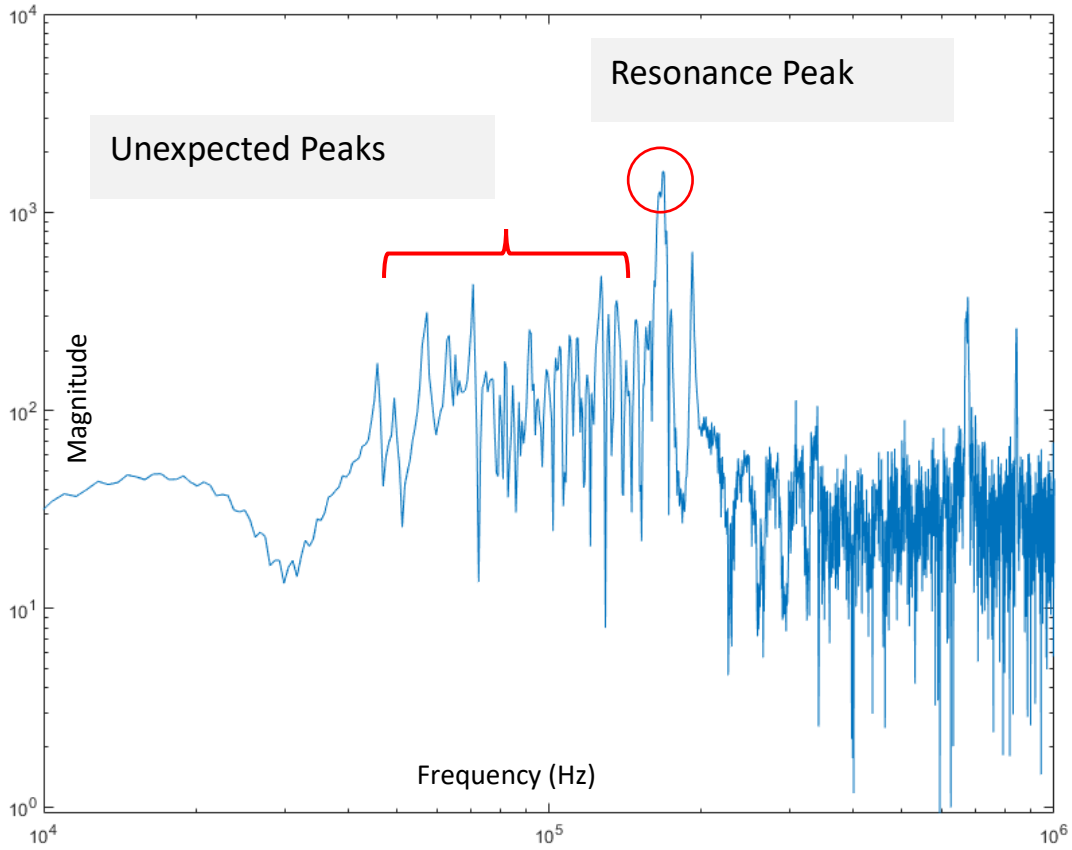

Figure 6.3.1 Frequency spectrum of PMUT chip with r = 355 radius.

The smaller radius chip is designed to have a resonant frequency of 338 kHz. The pulse echo experimental result of this chip is shown in figure 6.3.2.

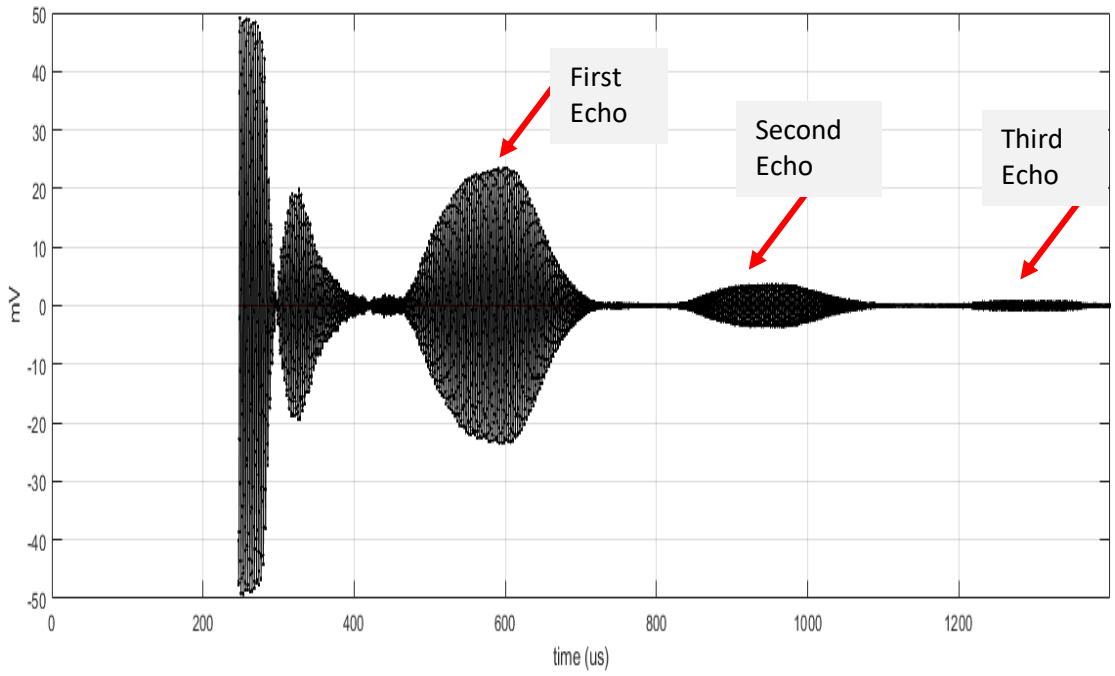

Figure 6.3.2 Pulse echo response of PMUT chip with r = 275 radius.

In this experiment, we excited one of the five arrays with 10 Vpp, 50 cycles at 338 kHz. We placed the reflector at 6.35 cm away. With a speed of sound of 340 m/s in air, we are expected to see our first echo at 374 us which corresponds to our first echo as shown in figure 6.3.2. The ability of this chip to show three echoes implies that we can at least detect object at a distance of 19 cm away from the PMUT chip.

With this chip successfully characterized, we setup our experiment to long-distance object detection. Figure 6.3.3 shows the experiment setup.

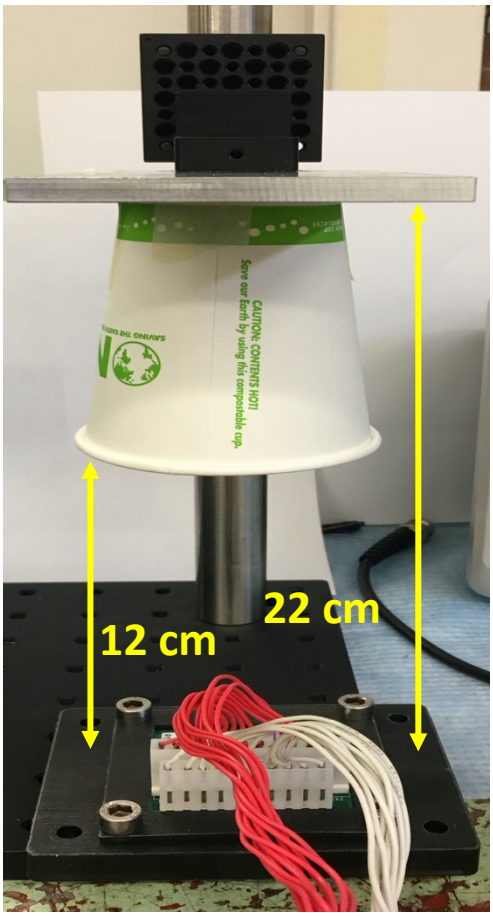

Figure 6.3.3 Paper cup detection experimental Setup.

In figure 6.3.3, an empty paper cup is fixed upside down from the PMUT chip with its rim at a distance of 12 cm away from the chip and the bottom of the cup 22 cm away from the chip. The PMUT chips are excited under the same condition. The experimental result is shown in figure 6.3.4.

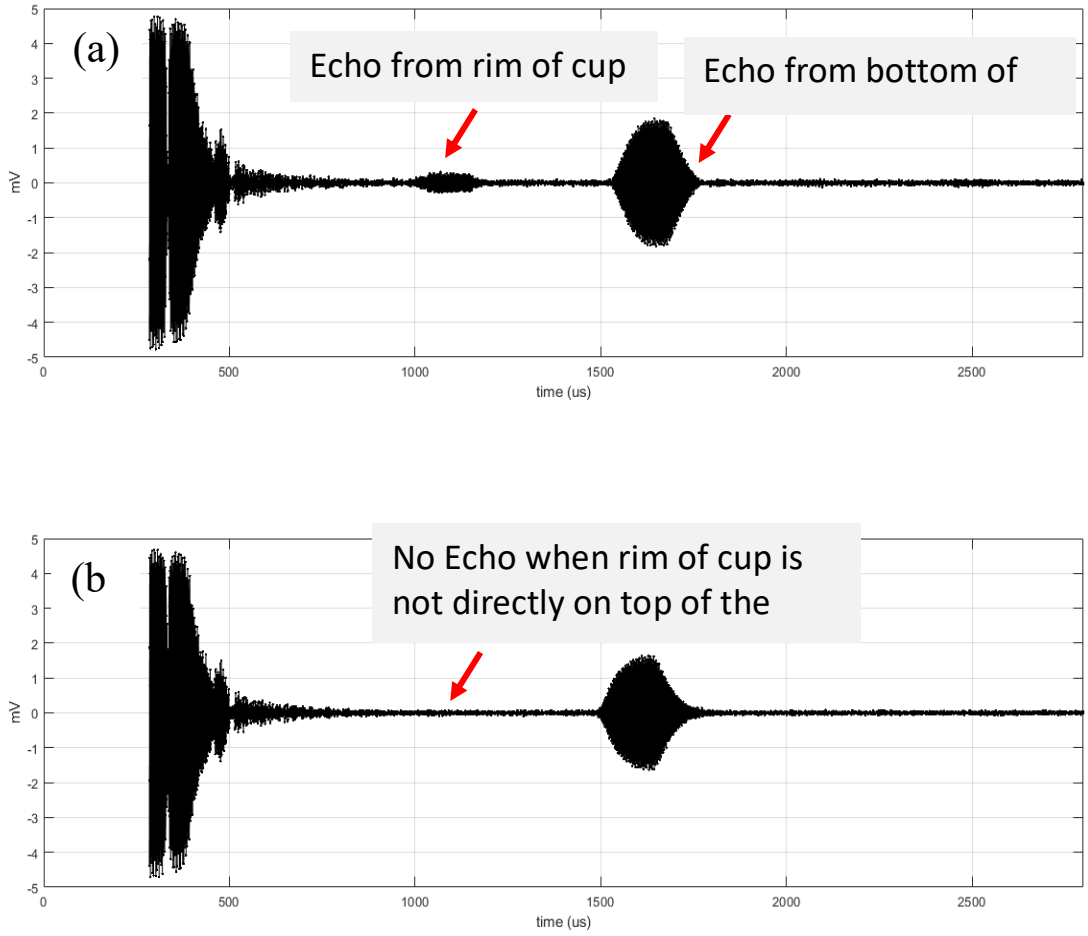

Figure 6.3.4 Pulse echo experimental Result. (a) Rim of cup directly on top of the PMUT chip. (b) Rim of cup not directly on top of the PMUT chip.

Figure 6.3.4 (a) shows the experimental result of the scenario where the rim of the cup is placed directly on top of the PMUT chip. With a speed of sound of 340 m/s in air, we expect to see an echo at 706 us for the rim of the cup and at 1294 us for the bottom of the cup. The experimental result shows matching time of flight for the two echoes. Note that the rim of cup gives a very weak echo. This is due to the small spot size of the rim where not all of the transmitted ultrasound reached the rim and thus the reflected signal is small.
The large receiving amplitude from the bottom of the cup shows promising result. Out experimental setup platform can only allow 22 cm distance, and this implies that even longer detection distance can be possible.

Figure 6.3.4 (b) shows the experimental results of the scenario where the rim of the cup is not placed directly on top of the PMUT chip. In this situation, we can only see the echo from the bottom of the cup which happens at 1294 us time of flight. This also proves that the previous small echo that we observe is from the rim of the cup. If we steer the beam toward the rim of cup, then we will be able to observe an echo.

6.4 Conclusion

In this chapter, we investigated the possibility of using PMUT chip for long distance object detection by enlarging standalone chip diaphragm size. Traditionally, we've fabricated devices that gives 633 kHz for its lowest resonant frequency in air.

Here, we fabricated two chips at two different radius and investigated the chip quality for long-distance object detection. Each chip contains five arrays where each array has 4x20 standalone PMUTs. The larger PMUT is designed to have a 355 um radius with a resonant frequency of 180 kHz. Although we are able to observe its resonance, we also seen unexpected resonant peaks at frequencies below its resonant frequency. These unexpected resonant peaks are due to broken PMUTs which is likely caused by stress distribution from the fabrication process.

The smaller PMUT is designed to have a 275 um radius with a resonant frequency of 338 kHz. The chip shows clear echoes when we characterized it in pulse-echo. We then placed a paper cup upside down where the rim of cup is 12 cm away from the chip and the bottom of cup if 22 cm away from the chip. From pulse echo experiment, we observe two clear echoes when we place rim of cup directly on top of the chip and one clear echo when rim of cup is not directly on top of the chip.

As a result, we successfully fabricated a PMUT chip that is able to operate in air at low frequency with 22 cm long distance object detection ability. This study opens up more application space for air-coupled applications using PMUTs.

Chapter 7

Conclusion and Future Works

In this dissertation, we worked on improving standalone PMUT's acoustic performance, meaning vibrating amplitude, acoustic pressure and electromechanical coupling through changing the boundary condition of a traditional PMUT. We validated our design from simulation and analytical modeling. We then fabricated such PMUT and characterized its performance. We see matching results between simulation and experiment which means that we've designed a new PMUT structure with significantly better performance compared to a traditional PMUT structure.

With the novel pinned PMUT design, we further investigated the possibility of altering the design to enable same chip transmitting and receiving functionality. We achieved this goal by changing the location of pinned boundary and designed the dual-electrode pinned PMUT accordingly. Simulation results proved that the dual-electrode pinned PMUT gives similar performance compared to the original pinned PMUT when excited differentially.

Using these novel PMUT design, we explored different applications. We first looked at using PMUT for tilt sensing. Instead of using time-of-flight, which is the traditional way, we used the receiving PMUT's pressure/voltage to determine tilt angle. We demonstrated experimentally that with our PMUT chip, we are able to measure tilt angle between $-8°$ to $+8°$ with an accuracy of $\pm 0.7°$.

The further investigated the possibility of using PMUT for a complete wireless power transfer system, meaning using PMUT as both the transmitting and receiving unit. We designed a pinned ring PMUT first as it is an essential element for the transmitting array. We see a 2.2 times improvement in center displacement comparing a pinned ring PMUT to a traditional ring PMUT. We then arranged these pinned ring PMUT into annular array to form the transmitting unit. We see 5.5 times improvement in acoustic intensity at the receiving unit when we phase shift the transmitted ultrasound and a maximum of 57% efficiency when we focus the beam at 2.7 mm distance.

We then investigated our fabrication limit on manufacturing large diaphragm PMUT for low frequency air-coupled applications. We fabricated two chips at larger radius, one at 355 um radius with 180 kHz resonant frequency in air and the other at 275 um radius with 338 kHz resonant frequency. We found that the larger radius PMUT has many broken PMUTs in the array which results in unexpected resonant peaks. With the 275 um radius PMUT chip, we demonstrated long-distance object detection experimentally by placing a paper

cup upside down from the PMUT chip where the rim of cup is 12 cm away from the chip and bottom of cup is 22 cm away from the chip. We can see clear echoes for both objects when rim of cup is placed directly above the transmitting array.
In conclusion, we've designed and fabricated a novel pinned PMUT providing excellent electromechanical coupling which enabled many applications such as tilt sensing and wireless power transfer. We also investigated our fabrication limitation on PMUT diaphragm size and demonstrated long-distance object detection with the largest possible PMUT our fabrication process allows.
For future work, we would like to (1) fabricate the dual-electrode pinned PMUT structure with low operational frequency in air and explore various applications such as (a) same chip long distance range finding, (b) temperature sensor, and (c) 3D object mapping; (2) Fabricate pinned ring PMUT array for wireless power transfer system with at least four channels for phase delay and characterize its performances and compare to state-of-the-art; (3) Look into different piezoelectric materials which can provide better acoustic performance and further lower PMUT device's operational frequency to open up more air-coupled application space.

References

[1] C. H. Sherman et al., Transducers and Arrays for Underwater Sound (The Underwater Acoustic Series), New York, NY, USA: Springer, 2007.
[2] D. T. Blackstock, Fundamentals of Physical Acoustics, New York, NY, USA: Wiley, 2000.
[3] D. A. Berlincourt et al., “Piezoelectric and piezomagnetic materials and their function in transducers” in Physical Acoustics, vol. I, Part A, New York: Academic Press, pp. 233-256, 1964.
[4] J. J. Bernstein et al., "Micromachined high frequency ferroelectric sonar transducers" in IEEE Transactions on Ultrasonics Ferroelectrics and Frequency Control, vol. 44, pp.960-969, Sep 1997.
[5] B. T. Khuri-Yakub et al., “Capacitive micromachined ultrasonic transducers for medical imaging and therapy” in Journal of Micromechanics and Microengineering, vol. 21, May 2011.
[6] M. Agrawal et al., "A microfluidic platform for glucose sensing using broadband ultrasound spectroscopy" in 2016 IEEE International Frequency Control Symposium (IFCS), pp. 1-5, New Orleans, LA, USA, 2016.
[7] F. L. Degertekin et al., "Annular-ring CMUT arrays for forward-looking IVUS: Transducer characterization and imaging" in IEEE Transactions on Ultrasonics Ferroelectrics and Frequency Control, vol. 53, pp. 474-482, Feb 2006.
[8] J. W. Busse et al., “The effect of low-intensity pulsed ultrasound therapy on time to fracture healing: A meta-analysis” in Cmaj, vol. 166, no. 4, pp. 437–441, 2002.
[9] S. Mitragotri, “Healing sound: the use of ultrasound in drug delivery and other therapeutic applications” in Nature Reviews Discovery, vol. 4, pp. 255-260, 2005.
[10] Y. Lu et al., "High frequency piezoelectric micromachined ultrasonic transducer array for intravascular ultrasound imaging" in 2014 IEEE 27th International Conference on Micro Electro Mechanical Systems (MEMS), San Francisco, CA, USA, pp. 745-748, 2014.
[11] D. E. Dausch et al., "Improved pulse-echo imaging performance for flexure-mode pMUT arrays" in 2010 IEEE International Ultrasonics Symposium, San Diego, CA, USA, pp. 451-454, 2010.
[12] D. E. Dausch et al., "In Vivo Real-Time 3-D Intracardiac Echo Using PMUT Arrays" in IEEE Trans. Ultrason. Ferroelectr. Freq. Control, vol. 61, pp. 1754-1764, Oct 2014.
[13] R. M. Schmitt et al., "Ultrasonic imaging of fingerprints using acoustical impediography" in Ultrasonics Symposium, vol.1, pp. 680-688, 2004.

[14] B. W. Drinkwater et al., “Ultrasonic arrays for non-destructive evaluation: A review” in Ndt & E International, vol. 39, pp. 525-541, Oct 2006.
[15] Fundamentals of Ultrasonic Imaging and Flaw Detection, National Instruments.
[16] B. A. Griffin et al., "Aluminum Nitride Ultrasonic Air-Coupled Actuator" in Journal of Microelectromechanical Systems, vol. 20, pp. 476-486, Apr 2011.
[17] D. E. Dausch, et al., “Piezoelectric Micromachined Ultrasound Transducer (pMUT) Arrays for 3D Imaging Probes” in 2006 IEEE Ultrasonics Symposium, Proceedings, Vancouver, CANADA, vol. 1-5, pp. 934-937, 2006.
[18] P. Muralt et al., “Piezoelectric micromachined ultrasonic transducers based on PZT thin films” in IEEE Transactions on Ultrasonics Ferroelectrics and Frequency Control, vol. 52, pp. 2276-2288, Dec. 2005.
[19] Q. Wang et al., "Design, Fabrication, and Characterization of Scandium Aluminum Nitride-Based Piezoelectric Micromachined Ultrasonic Transducers" in Journal of Microelectromechanical Systems, vol. 26, no. 5, pp. 1132-1139, Oct. 2017.
[20] S. Shelton et al., “Improved acoustic coupling of air-coupled micromachined ultrasonic transducers” in Proc. 2014 IEEE 27th International Conference on Micro Electro Mechanical Systems (MEMS), San Francisco, CA, USA, pp. 753-756, 2014.
[21] F. Akasheh et al., "Development of piezoelectric micromachined ultrasonic transducers," Sensors and Actuators A-Physical, vol. 111, pp. 275-287, Mar 15, 2004.
[22] S. Shelton et al., “CMOS-compatible AlN piezoelectric micromachined ultrasonic transducers” in Proc. 2009 IEEE Int. Ultrason. Symp. (IUS), pp.402-405, Rome, Italy, 2009.
[23] I. Ladabaum, et al., "Surface micromachined capacitive ultrasonic transducers" in IEEE Transactions on Ultrasonics, Ferroelectrics, and Frequency Control, vol. 45, no. 3, pp. 678-690, May 1998.
[24] M.S. Salim et al., “Capacitive micromachined ultrasonic transducers: Technology and application” in Journal of Medical Ultrasound, no.20, pp.8-31, 2012.
[25] G.-H. Feng et al., “Fabrication of MEMS ZnO dome-shaped-diaphragm transducers for high-frequency ultrasonic imaging” in Journal of Micromechanics and Microengineering, vol. 15, pp.586-590, March 2005.
[26] A. S. Ergun et al., “Capacitive micromachined ultrasonic transducers: Theory and technology” in J. Aerosp. Eng., vol.16, no.2, pp.76–84, 2003.
[27] C. Bayram et al., “Bandwidth improvement in a cMUT array with mixed sized elements” in IEEE International Ultrasonics Symposium, 2005, vol. 00, no. c, pp. 1956–1959.

[28] J.M. Rothberg et al., inventors, Butterfly Network Inc, “Monolithic ultrasonic imaging devices, systems and methods”, United States patent US9521991B2, Dec 20, 2016.
[29] Y. Lu et al., “Short-range and high-resolution ultrasound imaging using an 8 MHz aluminum nitride PMUT array" in IEEE Int. Conf. on MEMS, Micro Electro Mechanical Systems (MEMS), pp. 140-143, Jan. 2015.
[30] A. Bhuyan, et al., “3D volumetric ultrasound imaging with a 3232 CMUT array integrated with front-end ICs using IP-chip bonding technology" in IEEE Int. Solid-State Circuits Conf. (ISSCC) Dig. Tech. Papers, pp. 396-397, Feb. 2013.
[31] J. M. Nam et al., "Design and implementation of a capacitive fingerprint sensor circuit in CMOS technology" in Sensor Actuat. A-Phys., vol. 135, pp. 283-291, Mar 30 2007.
[32] X. Jiang et al., “Ultrasonic fingerprint sensor with transmit beamforming based on a PMUT array bonded to CMOS circuitry” in IEEE Transactions on Ultrasonics, Ferroelectrics, and Frequency Control (IUFFC), vol.64, no.9, pp.1401-1408, 2017
[33] D. A. Horsley et al., "Ultrasonic fingerprint sensor based on a PMUT array bonded to CMOS circuitry" in 2016 IEEE International Ultrasonics Symposium (IUS), Tours, pp.1-4, 2016.
[34] H. Tang et al., "Pulse-echo ultrasonic fingerprint sensor on a chip" in 2015 18th International Conference on Solid-State Sensors, Actuators and Microsystems (TRANSDUCERS), Anchorage, AK, USA, pp. 674-677, 2015.
[35] S. Akhbari et al., “Dual-electrode Bimorph PMUT Arrays for Hanhled Therapeutic Medical Devices” in Proc. 2016 29th IEEE International Conference on Micro Electro Mechanical Systems (MEMS), Shanghai, China, pp. 1102-1105, 2016.
[36] R. J. Przybyla et al., “3D ultrasonic gesture recognition” in IEEE Int. Solid-State Circuits Conf. (ISSCC) Dig. Tech. Papers, pp.210–211, Feb. 2014.
[37] O. Rozen et al., "Monolithic MEMS-CMOS ultrasonic rangefinder based on dual-electrode PMUTs" in 2016 IEEE 29th International Conference on Micro Electro Mechanical Systems (MEMS), Shanghai, pp. 115-118, 2016.
[38] J. K. Schneider et al., "Ultrasonic imaging systems for personal identification" in IEEE Ultrasonics Symposium Proceedings, Vols 1 and 2, pp. 595-601, 2001.
[39] Z. Zhou et al., "Monocrystalline PMNN-PZT thin film ultrasonic rangefinder with 2 meter range at 1 volt drive" in 2017 19th International Conference on Solid-State Sensors, Actuators and Microsystems (TRANSDUCERS), Kaohsiung, pp. 167-170, 2017.

[40] R. J. Przybyla et al., "In-Air Rangefinding With an AlN Piezoelectric Micromachined Ultrasound Transducer" in IEEE Sensors Journal, vol. 11, no. 11, pp. 2690-2697, Nov. 2011.
[41] L.C. Lynnworth et al., “Ultrasonic flowmeters: Half century progress report, 1955-2005” in Ultrasonics, vol. 44, pp. 1371-1378, 2006.
[42] D. Han et al., “Two-dimensional ultrasonic anemometer using the directivity angle of an ultrasonic sensor” in Microelectronics Journal, vol. 39, pp. 1195-1199, 2008.
[43] G.T. Bui et al., “Two capacitive micro-machined ultrasonic transducers for wind speed measurement” in Sensors, vol. 16, no. 6, pp. 814, 2016
[44] Z. Wang et al., "Ultrasound radiating performances of piezoelectric micromachined ultrasonic transmitter" in Appl. Phys. Lett., vol. 86, Jan 17, 2005.
[45] Q. F. Zhou et al., "Self-focused high frequency ultrasonic transducers based on ZnO piezoelectric films" in Appl. Phys. Lett., vol. 90, Mar 12, 2007.
[46] F. Sammoura et al., “Optimizing the electrode size of circular bimorph plates with different boundary conditions for maximum deflection of piezoelectric micromachined ultrasonic transducers” in Ultrasonics, vol.53, pp.328–334, 2013.
[47] Y. Liang et al., "Pinned Boundary Piezoelectric Micromachined Ultrasonic Transducers," 2019 IEEE 32nd International Conference on Micro Electro Mechanical Systems (MEMS), Seoul, South Korea, pp. 791-794, 2019.
[48] H. Yu et al., “Capacitive micromachined ultrasonic transducer based tilt sensing” in Applied Physics Letter, vol. 101, issue 153502, 2012.
[49] A. Kurs et al., “Wireless Power Transfer via Strongly Coupled Magnetic Resonances” in Science, Vol. 317, Issue 5834, pp. 83-86, 2007.
[50] S. Y. R. Hui et al., "A Critical Review of Recent Progress in Mid-Range Wireless Power Transfer" in IEEE Transactions on Power Electronics, vol. 29, no. 9, pp. 4500-4511, Sept. 2014.
[51] A. P. Sample et al., "Analysis, Experimental Results, and Range Adaptation of Magnetically Coupled Resonators for Wireless Power Transfer" in IEEE Transactions on Industrial Electronics, vol. 58, no. 2, pp. 544-554, Feb. 2011.
[52] A. S. Rekhi et al., "Wireless Power Transfer to Millimeter-Sized Nodes Using Airborne Ultrasound" in IEEE Transactions on Ultrasonics, Ferroelectrics, and Frequency Control, vol. 64, no. 10, pp. 1526-1541, Oct. 2017.
[53] B. Eovino et al., “Broadband ring-shaped PMUTs based on acoustically induced resonance” in 2017 IEEE 30th International Conference on Micro Electro Mechanical Systems (MEMS), pp.1184-1187, Las Vegas, USA, 2017.

[54] Y. Lu et al., “A high fill-factor annular array of high frequency piezoelectric micromachined ultrasonic transducers” in Journal of Microelectromechanical Systems, vol.24, no.4, pp.904-913, 2015.
[55] B. Eovino et al., “A single-chip flow sensor based on bimorph pMUTs with differential readout capabilities” in 2018 IEEE 31st International Conference on Micro Electro Mechanical Systems (MEMS), pp.1184-1187, Belfast, Northern Ireland, 2018.
[56] C. Sun, et al., "Investigation of Broadband Characteristics of Multi-Frequency Piezoelectric Micromachined Ultrasonic Transducer (MF-pMUT)" in IEEE Sensors Journal, vol. 19, no. 3, pp. 860-867, 1 Feb.1, 2019.
[57] B. Eovino et al., “Ring-shaped piezoelectric micromachined ultrasonic transducers (PMUT) with increased pressure generation” in Proc. of Hilton Head 2016.
[58] F. Sammoura, et al., “Enhanced coupling of piezoelectric micromachined ultrasonic transducers with initial static deflection” in 2013 IEEE Sensors, Baltimore, MD, USA, pp. 1-4, 2013.
[59] S. Akhbari et al., “Bimorph piezoelectric micromachined ultrasonic transducers” in Journal of Microelectromechanical Systems, vol.25, no.2, pp.326-336, 2016.
[60] A. Guedes et al., “Aluminum nitride PMUT based on a flexurally-suspended membrane” in 2011 IEEE Transducers, pp.2062-2065, Beijing, China, 2011.
[61] C. Nistorica et al., "Modeling and characterization of a 3D-MEMS piezoelectric ultrasound transducer" in 2016 IEEE International Ultrasonics Symposium (IUS), Tours, pp. 1-4, 2016.
[62] F. Sammoura, et al., “Multiple electrode piezoelectric micromachined ultrasonic transducers” in 2014 IEEE International Ultrasonics Symposium (IUS), Chicago, IL, USA, pp. 305-308, 2014.
[63] Y. Lu et al., “Broadband piezoelectric micromachined ultrasonic transducers based on dual resonance modes” in Proc. 2015 28th IEEE International Conference on Micro Electro Mechanical Systems (MEMS), Estoril, Portugal, pp. 146-149, 2015.
[64] E. Ventsel et al., Thin Plates and Shells: Theory, Analysis, and Applications: CRC Press, 2001.
[65] S. A. N. Prasad et al., “Analytical electroacoustic model of a piezoelectric composite circular plate” in Aiaa Journal, vol. 44, pp. 2311-2318, Oct 2006.
[66] K. Smyth et al., "Analytic solution for N-electrode actuated piezoelectric disk with application to piezoelectric micromachined ultrasonic transducers" in IEEE Transactions on Ultrasonics, Ferroelectrics, and Frequency Control, vol. 60, no. 8, pp. 1756-1767, August 2013.

[67] D. E. Dausch et al., "Theory and Operation of 2-D Array Piezoelectric Micromachined Ultrasound Transducers" in IEEE Transactions on Ultrasonics Ferroelectrics and Frequency Control, vol. 55, pp. 2484-2492, Nov 2008.
[68] J. N. Reddy, “Theory and Analysis of Elastic Plates and Shells” 2nd ed., Boca Raton, FL: CRC Press, 2007.
[69] S. Akhbari et al., “Equivalent Circuit Models for Large Arrays of Curved and Flat Piezoelectric Micromachined Ultrasonic Transducers” in IEEE Trans. Ultrason. Ferroelectr. Freq. Control, vol. 63, no. 3, pp. 432–447, 2016.
[70] F. Akasheh et al., "Piezoelectric micromachined ultrasonic transducers: Modeling the influence of structural parameters on device performance" in IEEE Transactions on Ultrasonics Ferroelectrics and Frequency Control, vol. 52, pp. 455-468, Mar 2005.
[71] R. Krimholtz et al., “New Equivalent Circuit for Piezoelectric Transducers” in Electronic Letters, vol. 6, pp. 398-399 & 560, 1970.
[72] F. Sammoura et al., “An Equivalent Network Representation of a Clamped Bimorph Piezoelectric Micromachined Ultrasonic Transducer with Circular and Annular Electrodes using Matrix Manipulation Techniques” in IEEE Transactions on Ultrasonics, Ferroelectrics, and Frequency Control, in press. pp. 1989-2003, vol. 60, no. 9, September 2013.
[73] F. Sammoura et al., "An Accurate Equivalent Circuit for the Clamped Circular Multiple-Electrode PMUT with Residual Stress" in Joint UFFC, EFTF and PFM Symposium, Prague, Czech Republic, pp. 275-278, 2013.
[74] D. Karim et al., “Finite Element Analysis in Combination with Perfectly Matched Layer to the Numerical Modeling of Acoustic Devices in Piezoelectric Materials” in Applied Mathematics, 4, 64-71, 2013.
[75] T. Kamohara et al., “Influence of aluminum nitride interlayers on crystal orientation and piezoelectric property of aluminum nitride thin films prepared on titanium electrodes” in Thin Solid Films, vol 515, issue 11, pp. 4565-45699, 2007.
[76] S. Trolier-McKinstry et al., "Thin film piezoelectrics for MEMS" in Journal of Electroceramics, vol. 12, pp. 7-17, Jan-Mar 2004.

[77] R. Schellin et al., “A Low Cost Angular Rate Sensor for Automotive Applications in Surface Micromachining Technology” In: Ricken D.E., Gessner W. (eds) Advanced Microsystems for Automotive Applications 99. Springer and the environment. Springer, Berlin, Heidelberg, 1999.
[78] S. Ray et al., "Design and development of Tilted Single Axis and Azimuth-Altitude Dual Axis Solar Tracking systems" in 2016 IEEE 1st International Conference on Power Electronics, Intelligent Control and Energy Systems (ICPEICES), Delhi, pp. 1-6, 2016.

[79] X. Chen et al., "Transmitting Sensitivity Enhancement of Piezoelectric Micromachined Ultrasonic Transducers via Residual Stress Localization by Stiffness Modification" in IEEE Electron Device Letters, vol. 40, no. 5, pp. 796-799, May 2019.
[80] P. L. Carson et al., “Ultrasonic power and intensities produced by diagnostic ultrasound equipment” in Ultrasound in Med. & Biol., Vol. 3, pp. 341-350. Pergamon Press, Printed in Great Britain, 1978.
[81] E. Mehdizadeh et al., "AlN on SOI pMUTs for ultrasonic power transfer" in 2017 IEEE International Ultrasonics Symposium (IUS), Washington, DC, USA, pp. 1-4, 1978.
[82] H. Basaeri et al., "A MEMS-Scale Ultrasonic Power Receiver for Biomedical Implants" in IEEE Sensors Letters, vol. 3, no. 4, pp. 1-4, Art no. 2501104, April 2019.
[83] Phipps Natalie, "Acoustic Intensity Measurement System: Application in Localized Drug Delivery", Master's Theses. 3784, 2010.
[84] T. Ishiyama et al., "Impact of a wireless power transmission system using an ultrasonic air transducer for low-power mobile applications" in IEEE Symposium on Ultrasonics, 2003, Honolulu, HI, USA, vol.2, pp.1368-1371, 2003.
[85] S. Ozeri et al., “Ultrasonic transcutaneous energy transfer for powering implanted devices” in Ultrasonics, vol. 50, issue 6, pp. 556-566, May 2010.
[86] Q. Shi et al., “MEMS Based Broadband Piezoelectric Ultrasonic Energy Harvester (PUEH) for Enabling Self-Powered Implantable Biomedical Devices” in Scientific Reports, 6, Article number: 24946, 2016.
[87] S. Ozeri et al., “Ultrasonic transcutaneous energy transfer using a continuous wave 650 kHz Gaussian shaded transmitter” in Ultrasonics, vol. 50, issue 7, pp. 666-674, June 2010.
[88] S.Q. Lee et al., “Biocompatible wireless power transferring based on ultrasonic resonance devices” in Proc. Mtgs. Acoust. 19, 030030, 2013.
[89] V. F. Tseng, et al., "Phased Array Focusing for Acoustic Wireless Power Transfer" in IEEE Transactions on Ultrasonics, Ferroelectrics, and Frequency Control, vol. 65, no. 1, pp. 39-49, Jan. 2018.
[90] B. E. Eovino, et al., "Concentric PMUT Arrays for Focused Ultrasound and High Intensity Applications" in 2019 IEEE 32nd International Conference on Micro Electro Mechanical Systems (MEMS), Seoul, South Korea, pp. 771-774, 2019.
[91] J. A. Brown et al., "Design and fabrication of annular arrays for high-frequency ultrasound," in IEEE Transactions on Ultrasonics, Ferroelectrics, and Frequency Control, vol. 51, no. 8, pp. 1010-1017, Aug. 2004.

[92] A. Marzo, et al., "Ultraino: An Open Phased-Array System for Narrowband Airborne Ultrasound Transmission" in IEEE Transactions on Ultrasonics, Ferroelectrics, and Frequency Control, vol. 65, no. 1, pp. 102-111, Jan. 2018.
[93] A. S. Rekhi et al., "Wireless Power Transfer to Millimeter-Sized Nodes Using Airborne Ultrasound" in IEEE Transactions on Ultrasonics, Ferroelectrics, and Frequency Control, vol. 64, no. 10, pp. 1526-1541, Oct. 2017.
[94] E. Mehdizadeh et al., "Through-package wireless powering via piezoelectric micromachined ultrasonic transducers" in 2018 IEEE Micro Electro Mechanical Systems (MEMS), Belfast, Northern Ireland, pp. 1076-1079, 2018.
[95] A. K. RamRakhyani et al., "Design and Optimization of Resonance-Based Efficient Wireless Power Delivery Systems for Biomedical Implants" in IEEE Transactions on Biomedical Circuits and Systems, vol. 5, no. 1, pp. 48-63, Feb. 2011.
[96] S. Surappa et al., "Analysis and Design of Capacitive Parametric Ultrasonic Transducers for Efficient Ultrasonic Power Transfer Based on a 1-D Lumped Model" in IEEE Transactions on Ultrasonics, Ferroelectrics, and Frequency Control, vol. 65, no. 11, pp. 2103-2112, Nov. 2018.